Hall D / GlueX
Technical Construction Report

June 26, 2014

Abstract

The Technical Construction Report describes the Hall D facility constructed as a part of the JLab 12 GeV Upgrade Project. The facility is dedicated to physics with linearly-polarized photon beam. Electron beam extracted from the CEBAF accelerator to the new Tagger Hall produces polarized photons by the coherent radiation. The photon beam is delivered to Hall D. The Hall D apparatus is optimized for light-meson spectroscopy - experiment GlueX. The main goal of GlueX is to search and map out the spectrum of light hybrid mesons with exotic quantum numbers.

M. Dugger, B. Ritchie and I. Senderovich
Arizona State University, Tempe AZ 85281

D. Fassouliotis, P. Ioannou, and Ch. Kourkoumelis
University of Athens, Athens, Greece

N. Jarvis, W. Levine, P. Mattione, W. McGinley, C. A. Meyer (GlueX spokesperson), R. A. Schumacher, and M. Staib
Carnegie Mellon University, Pittsburgh,PA 15213

F. J. Klein, D. Sober, N. Sparks, and N. Walford
Catholic University of America, Washington, D.C.

D. Doughty
Christopher Newport University (Newport News, VA)

A. Barnes, R. Jones, J. McIntyre, F. Mokaya and B. Pratt
University of Connecticut, Storrs, CT

W. Boeglin, L. Guo, E. Pooser, and J. Reinhold
Florida International University, Miami,FL

H. Al Ghoul, V. Crede, P. Eugenio, A. Ostrovidov, and A. Tsaris
Florida State University, Tallahassee,FL

D. Ireland and K. Livingston
University of Glsagow, Glsagow UK

D. Bennett, J. Bennett, J. Frye, M. Lara, J. Leckey, R. Mitchell, K. Moriya, B. Schaefer and M. Shepherd (GlueX Deputy Spokesperson),
Indiana University, Bloomington,IN

O. Chernyshov, A. Dolgolenko, A. Gerasimov, V. Goryachev, I. Larin, V. Matveev and V. Tarasov
ITEP Moscow, Moscow, Russia

F. Barbosa, E. Chudakov (Hall D Leader), M. Dalton, A. Deur, J. Dudek, C. Cuevas, H. Egiyan, S. Furletov, M. Ito, D. Lawrence, D. Mack, M. McCaughan, M. Pennington, L. Pentchev, Y. Qiang, E. Smith, A. Somov, S. Taylor, T. Whitlatch, and B. Zihlmann,
Jefferson Lab, Newport News, VA 23606

R. Miskimen
University of Massachusetts Amherst, Amherst, MA

B. Guegan, J. Hardin, J. Stevens and M. Williams
Massachusetts Institute of Technology, Cambridge, MA

V. Berdnikov, G. Nigmatkulov, A. Ponosov, D. Romanov, S. Somov and I. Tolstukhin
MEPHI, Moscow, Russia

C. Salgado
Norfolk State University, Norfolk, VA

P. Ambrozewicz, A. Gasparian and R. Pedroni

University of North Carolina A&T, A&T State, NC

T. Black and L. Gan
University of North Carolina, Wilmington, NC

S. Dobbs, K. K. Seth, X. Ting and A. Tomaradze
Northwestern University, Evanston, IL

T. Beattie, G. Huber, G. Lolos, Z. Papandreou, E. Plummer, A. Semenov and I. Semenova
University of Regina, Regina, Saskatchewan, Canada

W. Brooks, H. Hakobyan, S. Kuleshov, O. Soto, A. Toro and I. Vega
Santa Maria University, Valparaiso, Chile

N. Gevorgyan, H. Hakobyan and V. Kakoyan
Yerevan Physics Institute, Yervan, Armenia

Contents

Chapter 1

Overview

The Technical Construction Report describes the Hall D facility constructed as a part of the JLab 12 GeV Upgrade Project. The facility is dedicated to physics with linearly-polarized photon beam. Electron beam extracted from the CEBAF accelerator to the new Tagger Hall produces polarized photons by the coherent radiation. The photon beam is delivered to Hall D. The Hall D apparatus is optimized for light-meson spectroscopy - experiment GlueX. The main goal of GlueX is to search and map out the spectrum of light hybrid mesons with exotic quantum numbers.

1.1 Physics Motivation [1]

The primary motivation of the GlueX experiment is to search for, and ultimately study the pattern of gluonic excitations in the meson spectrum produced in γp collisions, in a mass range of 1.5-2.5 GeV/c^2. Recent lattice QCD calculations predict a rich spectrum of hybrid mesons that have both exotic and non-exotic J^{PC} quantum numbers, corresponding to $q\bar{q}$ states ($q = u$, d, or s) coupled with a gluonic field.

1.1.1 Expectations for Exotic Hybrid Mesons

Lattice QCD calculations predict several nonets of exotic J^{PC} quantum number states. The lightest supermultiplet of hybrid mesons contains four nonets with J^{PC} quantum numbers 1^{--}, 0^{-+}, 1^{-+} and 2^{-+}, where the 1^{-+} quantum numbers are exotic. In addition to the lowest mass states, the lattice calculations predict several nonets of excited hybrids. Those with exotic quantum numbers are $J^{PC} = 1^{-+}$, $J^{PC} = 0^{+-}$, and two nonets with $J^{PC} = 2^{+-}$. Several of the these states are discussed in Table 1.1. Also shown in the table are some of the possible decay modes for these mesons. While some of the final states are fairly simple, such as $\rho\pi$, $\omega\pi$ and $\eta'\pi$, most of them involve more complicated decays leading to several particles in the final state. Typical decays involve both charged particles and photons from the decays of π° and η mesons. A primary goal of the GlueX detector is to be able exclusively reconstruct these final states with good efficiency and purity. This goal has been one of the primary drivers to the design of the experiment.

Not only do the lattice calculations predict the existence of hybrid mesons, but they also predict masses and nonet mixing angles. The mixing angles relate the amount of $s\bar{s}$ and $u\bar{u}+d\bar{d}$

[1] *SVN revision ID:* tcr_intro.tex 13927 2014-06-20 17:19:48Z cmeyer

Table 1.1: A compilation of exotic quantum number hybrid approximate masses and decay predictions. Masses are estimated from dynamical LQCD calculations with $M_\pi = 396$ MeV/c^2. (We consider η, η', and ω to be stable final state particles.)

	Approximate Mass (MeV)	J^{PC}	Relevant Decays	Final States
π_1	1900	1^{-+}	$b_1\pi$, $\rho\pi$, $f_1\pi$, $a_1\eta$, $\eta'\pi$	$\omega\pi\pi$, 3π, 5π, $\eta 3\pi$, $\eta'\pi$
η_1	2100	1^{-+}	$a_1\pi$, $f_1\eta$, $\pi(1300)\pi$, $\eta\eta'$	4π, $\eta 4\pi$, $\eta\eta\pi\pi$
η_1'	2300	1^{-+}	$K_1(1400)K$, $K_1(1270)K$, K^*K	$KK\pi\pi$, $KK\pi$, $KK\omega$
b_0	2400	0^{+-}	$\pi(1300)\pi$, $h_1\pi$, $b_1\eta$, $f_1\rho$	4π, $\omega\eta\pi$, $\eta 4\pi$
h_0	2400	0^{+-}	$b_1\pi$, $h_1\eta$, $K(1460)K$	$\omega\pi\pi$, $\eta 3\pi$, $KK\pi\pi$
h_0'	2500	0^{+-}	$K(1460)K$, $K_1(1270)K$, $h_1\eta$	$KK\pi\pi$, $\eta 3\pi$
b_2	2500	2^{+-}	$a_2\pi$, $\omega\pi$, $\rho\eta$, $a_1\pi$, $h_1\pi$, $f_1\rho$, $b_1\eta$	$\omega\pi$, 4π, $\eta\pi\pi$, $\eta 4\pi$, $\omega\eta\pi$
h_2	2500	2^{+-}	$b_1\pi$, $\rho\pi$, $\omega\eta$, $f_1\omega$	$\omega\pi\pi$, 3π, $\omega\eta 2\pi$
h_2'	2600	2^{+-}	$K_1(1400)K$, $K_1(1270)K$, K_2^*K	$KK\pi\pi$, $KK\pi$

in the isospin zero members of each nonet. For the exotic mesons listed in the table, the mixing is between the η_1 and η_1', the h_0 and h_0', and between the b_0 and the b_0'. These mixing angles can be measured experimentally by comparing the decay rates of each mesons to final states with and without kaons. The requirement to reconstruct exclusive final states involving several charged particles and photons requires a nearly hermetic detector with good momentum and energy resolution.

A thorough study of the hybrid spectrum, including the identification of the isovector triplet, with charges 0 and ± 1, and both isoscalar members, $|s\bar{s}\rangle$ and $|u\bar{u}\rangle + |d\bar{d}\rangle$, for each predicted hybrid combination of J^{PC}, may only be achieved by conducting a systematic amplitude analysis of many different hadronic final states.

1.1.2 Photoproduction

Photoproduction provides certain advantages for the amplitude analysis of the final states in comparison with hadroproduction, say in $\pi^- p$ collision. In photoproduction the initial state interaction is suppressed. Also, photons can be linearly polarized. Photoproduction amplitudes involving unpolarized (or circularly polarized) photons can depend on the center of mass energy, $\sqrt{s}$, as well as the angle between the produced meson system and the initial photon direction (the polar angle, θ). The use of linearly-polarized photons defines a second direction (along the polarization axis), and the corresponding production amplitudes can also depend on the angle to this axis—effectively the azimuthal angle, ϕ. The extra information from this angle ultimately simplify the amplitude analysis. For the same statistical precision, a factor of two change in the degree of linear polarization mapping into a factor of two change in needed statistics. In addition to the simplification, for t-channel production of mechanisms, there is a one-to-one mapping between the naturality of the exchanged particle (natural parity exchange has $J^P = 0^+, 1^-, 2^+, \cdots$, while unnatural exchange has $J^P = 0^-, 1^+, 2^-, \cdots$) and the orientation of the linear-polarization direction in the event.

1.2 The Hall-D Complex and the GlueX Detector

The Hall-D complex consists of a tagger hall where incident $12\,GeV$ electrons produce a beam of linearly polarized photons, and the experimental hall, where the photons interact in an experimental target and the resulting interactions are recorded by the GlueX detector. A schematic of the complex, including the tagger area and the GlueX experiment, is shown in Figure 1.1. More information on the production, tagging and monitoring of the photon beam

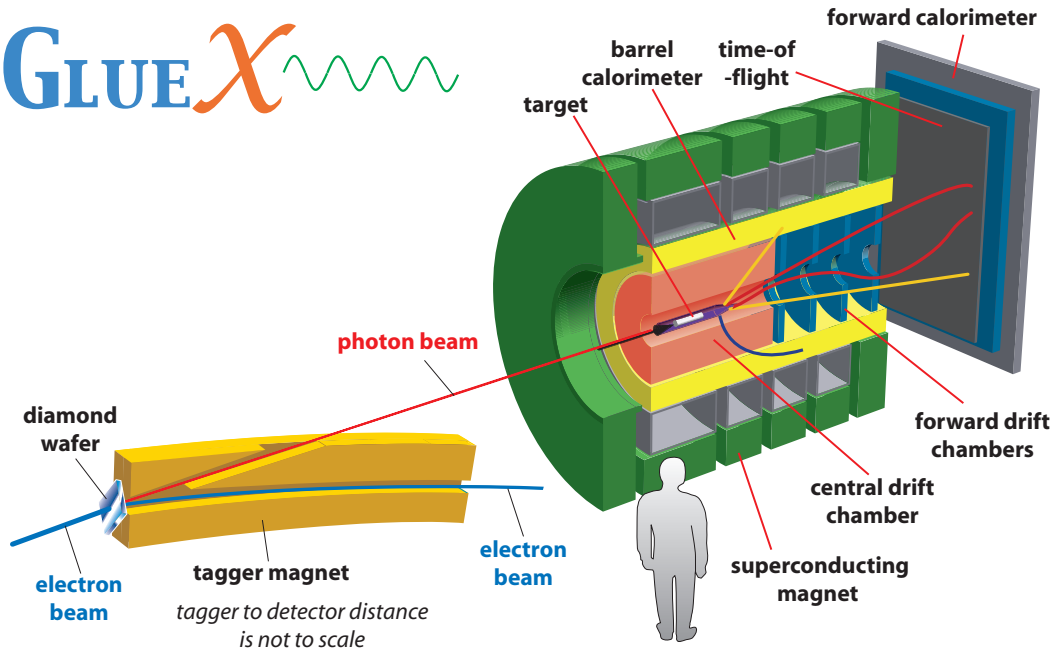

Figure 1.1: A cut-away drawing of the GlueX detector in Hall D.

can be found in Chapter 2. The GlueX detector is described in detail in Chapter 3.

1.2.1 Experimental Description

As seen in Figure 1.1, the $12\,GeV$ electron beam passes through a thin diamond wafer, where bremsstrahlung photons are produced. The electrons are then deflected by the tagger magnet. Non-radiating electrons are sent to a beam dump, while the electrons which have radiated more than a half of their energy are detected by a pair of hodoscope arrays. These arrays are aligned such that each detector element maps onto a narrow momentum range in the deflected electrons, and hence, a narrow energy range in the produced photons. Thus, the energy of each photon is "tagged" and known in the experiment. The photon beam then travels about $80\,m$ to the experimental hall, where prior to entering the experiment, it is collimated, and monitored using both a polarimeter and a pair spectrometer.

The photons can then interact in the target in GlueX. Much of the experimental apparatus is inside a solenoidal magnet with central filed of $2\,T$. The charged particles produced by the interacting photons are tracked by the start counter immediately outside the target (not shown in the figure), and then a pair of tracking systems. The central drift chamber is based on 28

layers of axial and stereo straws. The forward drift chambers are 24 drift chambers planes with both cathode and anode readout. The flight-time of charged particles are measured using a combination of the start counter and the time-of-flight wall in the forward direction, and the start counter and the barrel calorimeter inside the solenoid.

The final-state photons are detected in a pair of calorimeters. The barrel calorimeter, located inside the solenoid, consists if layers of scintillating fiber alternating with lead sheets. The forward calorimeter is downstream of the time-of-flight wall, and consists of 2800 lead-glass blocks.

1.2.2 Experimental Requirements

In order to be able to exclusively reconstruct events with final states given in Table 1.1, accurate reconstruction of the incident photon, as well as the produced charge particles and photons is necessary.

The linear polarization of the incident photon beam is produced through the coherent bremsstrahlung process. These coherent photons have energies in the range of 8.4 to $9\,GeV$, and will be about 40%, after the beam collimation to ~ 25 μrad with respect to the incoming electron direction. For these linearly-polarized photons, it is necessary to accurately know the photon energy, both for the exclusive final state reconstruction and also to accurately determine the photon polarization on an event-by-event basis. In GlueX, this energy is known to an accuracy of 0.1% of the incident photon energy.

In order to exclusively reconstruct multi-particle final states, the GlueX detector needs be nearly hermetic with good momentum and energy resolution for both charged particles and photons. In order to be able to carry out the needed amplitude analysis, the detector acceptance needs to be reasonably uniform, and well understood and modeled in simulation. Typical momentum resolution for charged particles 1–2%, while for very-forward high-momentum particles, it is somewhat worse at around 8-9%. For high-momentum charged particles, the tracking system has nearly hermetic acceptance for polar angles from about 2° to 150° in the lab. Because of target material, protons with momentum below about $350\,MeV/c$ are not detected, and pions with momentum under $200\,MeV/c$ can have spiraling trajectories in the detector, which make reconstruction challenging.

For photons, the typical energy resolution is $(5\,\text{to}\,6\%)/\sqrt{E_\gamma}$. There is some variation in the barrel calorimeter resolution, depending on the incident angle of the photon, but generally, photons above about $50\,MeV$ are detected in the BCAL. The interaction point along the beam direction is determined by comparing the information from the readouts on the upstream and downstream ends of the detector. The forward calorimeter can reconstruct photons whose energy is larger than $100\,MeV$, with uniform resolution across the face of the detector. There is an overlap region between the calorimeters at around 11°. Both photon detection efficiency and energy resolution is degraded in this region.

1.2.3 Data Requirements

In addition to the ability to reconstruct exclusive final states, the GlueX experiment will need to collect sufficient statistics to carry out amplitude analyses in small bins of meson invariant mass, and in momentum transfer, $|t|$. Large production cross sections for reactions of interest are $10\,\mu b$, while more typical final-state cross sections are a few hundred nb. The GlueX experiment has been built with a data acquisition system capable of collecting data using

photon beams with $10^8\,\gamma/s$ in the coherent peak. However, the experiment may be limited by electromagnetic backgrounds in the detector, and force to run at photon rates smaller than the design limit.

Expected raw event sizes are 15kilobytes, and the data acquisition limit is expected to be $20\,kHz$. The level-1 hardware trigger alone will allow the experiment to run at in incident photon rate of $10^7\,\gamma/s$ in the coherent peak. Of the $20\,kHz$ event rate, about $2\,kHz$ corresponds to hadronic interaction with photon in the coherent peak. In order to run at higher beam intensities, the level-3 software trigger is needed to keep the rate of events to tape limited to $20\,kHz$. Including the events where the energy of the interacting photon is above $9\,GeV$ roughly doubles the number of interesting hadronic events.

The typical final states listed in Table 1.1 are expected to range from 3.5% of the hadronic events for $\gamma p \to p3\pi$ to under 1%. Assuming an 85% reconstruction efficiency per final state particle, and that 60% of the final state protons are detectable, Table 1.2 shows the number of reconstructed events per hour assuming a total hadronic rate of $2\,kHz$ for events with photon energies in the coherent peak. These events are ultimately binned in both an meson invariant mass, as well as momentum transfer, $|t|$, but for most of these channels 40 days of running at 50% efficiency would produce about a factor of 500 times the number listed in the table.This is sufficient for an initial amplitude analysis on many of these channels. Phase IV running of GlueX anticipates 200 days of running with 5×10^7 photon beam intensity, a factor of 25 over the above estimate.

Table 1.2: PYTHIA predictions for the fraction of hadronic events in some final states interesting for exotic hybrid meson searches. The superscript on $(n\pi)^{0\pm}$ indicates the net electric charge of the n pions. The specific final state column looks are one particular charge combination, and the event rate column show the number of reconstructed events per second assuming 10^7 incident photons per second, and 85% reconstruction efficiency for each detected particle.

Reaction	Fraction	Specific f.s.	Events/hour
$\gamma p \to p(3\pi)^0$	3.5 %	$p\pi^+\pi^-\pi^0$	87×10^3
$\gamma p \to n(3\pi)^+$	2.0 %	$n\pi^+\pi^+\pi^-$	58×10^3
$\gamma p \to p(2\pi)^0\omega$	1.8 %	$p2\pi^+2\pi^-\pi^0$	35×10^3
$\gamma p \to n(2\pi)^+\omega$	1.0 %	$n2\pi^+\pi^-2\pi^0$	28×10^3
$\gamma p \to p(3\pi)^0\eta$	2.0 %	$p\pi^+\pi^-\pi^0\eta$	14×10^3
$\gamma p \to n(3\pi)^+\eta$	1.0 %	$n\pi^+\pi^+\pi^-\eta$	7×10^3
$\gamma p \to p(2\pi)^0\eta$	1.0 %	$p\pi^+\pi^-\eta$	8×10^3
$\gamma p \to n(2\pi)^+\eta$	< 1 %	$n\pi^+\pi^0\eta$	$< 13 \times 10^3$
$\gamma p \to p\pi^0\omega$	< 1 %	$p\pi^+\pi^-2\pi^0$	$< 19 \times 10^3$
$\gamma p \to n\pi^+\omega$	< 1 %	$n2\pi^+\pi^-\pi^0$	$< 33 \times 10^3$

1.3 Infrastructure [2]

The gross features of the infrastructure for the Hall D complex are given.

Table 1.3: General Hall D Tagger Building Infrastructure

Feature	Value
Electron beam energy	$\lesssim$ 12 GeV
Width and length of Tagger Hall	7.5 $\times$27.6 m^2
Beam height above floor	1.8 m
Low Conductivity Water (LCW) flow (130 psi supply, 70 psi drop, 90 deg F)	40 gal/min
Chilled Water flow, includes collimator (80 psi supply, 30 psi drop, 45 deg F)	10 gal/min
Floor Load capacity (designed for hydrostatic forces)	See facilities
Distance from radiator (the goniometer vacuum vessel center) to collimator (the front face)	75.29 m
Distance tagger magnet center to electron dump	$\sim$ 24 m
Power deposition in electron dump	$<$ 60 kW

Table 1.4: Collimator and Hall D Infrastructure

Feature	Value
Photon beam energy	$\lesssim$ 12 GeV
Size of collimator alcove	4.5$\times$12.5 m^2
Beam height above floor in collimator	1.0 m
Beam power deposition in collimator alcove	$<$ 10 W
Size of Hall D	15$\times$29.5 m^2
Crane (20 US tons) hook height above floor	11 m
Electrical power installed Hall D Complex	1 MVA
Floor Load capacity (designed for hydrostatic forces)	See facilities
Beam height above floor in Hall D	3.5 m
Low Conductivity Water (LCW) flow (130 psi supply, 70 psi drop, 90 deg F)	129 gal/min
Chilled Water flow, includes collimator (80 psi supply, 30 psi drop, 45 deg F)	128 gal/min
Power deposition in photon dump	$<$ 2 W

Table 1.5: Overall parameters for detector performance.

Feature	Value
Solenoidal magnet	$\lesssim$ 2 T
Charged particle momentum resolution, σ	$\sim$ 1-3%
Photon energy resolution, σ_E/E	$\sim 5.5\%/\sqrt{E}$

[2] *SVN revision ID:* tdr_summary_infr.tex 13853 2014-06-12 03:42:44Z gen

Chapter 2

Hall D Photon Beam

2.1 Introduction

The $12\,GeV$ electron beam enters the tagger hall and passes through a $20\,\mu m$ thick diamond wafer. When the electrons pass through the diamond crystal, they produce both an incoherent bremsstrahlung beam, and a coherent bremsstrahlung beam. The elctrons are then bent using a tagger magent. Those electrons which produced a photon are bent into a pair of tagger arrays to measure their energy, and from this measurement, the energy of the produced electron is known. The tagger hall beam optics have been engineered so it is impossible for electrons to travel to the experimental hall.

The energy of the coherenet component is selected by precisely orientating the diamond crystal relative to the incident eletron direction using a goniometer. The degree of linear polarization in the coherent peak is increases as the energy of the photons decreases from the electron beam energy. In the nominal GlueX configuration, we produce a coherent beam with maximum energy of $9\,GeV$, and a degree of linear polarization of 40% in the energy range of $8.4\,GeV$ up to the $9\,GeV$ edge. The coherent photons travel along the initial electron beam axis, while the incoherent component is produced in a cone around the electron beam axis. In the Hall-D complex, the resulting photon beam travels about $80\,m$, and is then passed through a $3.4\,mm$ diameter collimator. This allows most of the coherent photons to pass through into the experimental hall, while most of the incoherent photons are scraped away.

Just before passing into the experimental hall, the beam passes through a polarimeter to measure the degree of linear polarization, and then just after it enters the experimental hall about $4\,m$ above the floor. It first passes through the pair spectrometer, which monitors the energy and flux of the beam. Neither the polarimeter nor the pair spectrometer are shown in Figure 1.1. Finally, the photon beam travels through the GlueX detector, and ultimately goes to the photon beam dump just outside the downstream end of the experimental hall.

2.1.1 Beam Summary [1]

The main parameters and properties of the Photon Beam are given in Tables 2.1 and 2.2.

[1] *SVN revision ID:* tdr_summary_beam.tex 13876 2014-06-13 16:08:03Z cmeyer

Table 2.1: Electron beam parameters. The emittance, energy spread and the related parameters were predicted by a model of the transport line from the accelerator to the Hall D photon source.

parameter	design results
energy	12 GeV
minimum useful current	1 nA
maximum useful current	3 μA
maximum permitted current	5 μA
energy spread, RMS	$<$ 10 MeV
transverse x emittance	10 mm$\cdot\mu$rad
transverse y emittance	2.5 mm$\cdot\mu$rad
x-dispersion at radiator	$<$ 1 cm
y-dispersion at radiator	$<$ 1 cm
x spot size at radiator, RMS	1.1 mm
y spot size at radiator, RMS	0.7 mm
x image size at collimator, RMS	0.5 mm
y image size at collimator, RMS	0.5 mm
distance radiator to collimator	75.3 m
image position stability at collimator	$\pm$200 μm

Table 2.2: Operating parameters for an experiment using the coherent Bremsstrahlung beam, calculated with the properties listed in Table 2.1, a diamond radiator of thickness 20 μm, and the standard primary collimator of diameter 3.4 mm located at its nominal position. The electron beam current is taken to be 2.2 μA. The hadronic rates are calculated for a 30 cm liquid hydrogen target.

E upper edge of the peak	9 GeV
Peak effective range	8.4 - 9.0 GeV
Tagger rate in the effective range	240 MHz
N_γ in the effective range after collimator	100 MHz
Maximum polarization in the peak, after collimator	41%
Mean polarization in the effective range, after collimator	37%
Power on collimator	4.5 W
Power on target	0.7 W
Total hadronic rate	360 kHz
Hadronic rate in the effective range	15 kHz

2.2 Tagger Spectrometer

2.2.1 Specifications

To satisfy the needs of the GlueX physics program, the tagged photon spectrometer should meet the following specifications:

1. Photon energy detection from 70% to 75% of E_0 with energy resolution of about 0.1% r.m.s. Percentages refer to the primary beam energy E_0, i.e. "0.1%" means 12 MeV energy resolution for a 12 GeV beam.

2. A detector system which allows a counting rate of at least 5×10^6 electrons per second per 0.1% over this range of photon energies.

3. An additional capability for photon energy detection from 25% to 90% of E_0, with less stringent resolution and count rate requirements .

4. A quadrupole magnet between the radiator and dipole spectrometer which images the beam spot on the radiator onto a line on the focal plane. This feature makes it possible to envision the use of focal plane counters with two-dimensional readout, with which one could enhance the tagging efficiency of the source. Focal plane detectors with two-dimensional readout are considered as a possible upgrade beyond the baseline design presented in this chapter. Any improvements obtained using this technique would be over and above the performance figures presented in this report.

The system described below, based on a room-temperature design, meets all of these criteria. The option of a superconducting design was also studied. With a superconducting magnet, the spectrometer could operate at much higher fields, offering the possibility of some space savings in the size of the tagger focal plane array and larger head-room for future possible energy upgrades beyond 12 GeV. An iron yoke design was found which would clamp the 5 T field sufficiently to make it possible to operate normal phototubes on the nearby tagger focal plane. However, as shown below, rate considerations require a degree of segmentation in the tagging counters such that it is impractical to increase the dispersion along the focal plane above what is provided by a 1.5 T room temperature magnet. That being the case, it was decided that considerations of upgrade margin and electrical power alone do not justify the additional cost and complexity of a superconducting magnet.

2.2.2 Tagger Magnet

Tagger Magnet Summary [2]

The basic design or as-built parameters for the tagging magnet and the tagging spectrometer are given in Tables 2.3 and 2.4. The assembly drawing for the tagging magnet is D000001900-1000.

Table 2.3: Parameters for the tagging magnet.

Radius of curvature	26.7 m
Full-energy deflection	13.4°
Field at 12 GeV	1.5 T
Maximum Field	1.75 T
Gap height	3.0 cm
Flat pole tip width	32.5 cm
Length of yoke	6.146 m
Weight	65 US tons
Length of focal plane (25% to 98% of E_0)	9.10 m
Coil resistance	0.564 Ω
Coil power at 12 GeV	28 kW
Current at 12 GeV	223 A
Vacuum	10^{-5} Torr
Pole tip profile	Rogowski contour
Photon beam pipe diameter in yoke	0.94 in. ID

Table 2.4: Geometrical parameters of the tagging spectrometer for E_0 = 12 GeV : Bend = deflection angle; Drift = distance from exit edge to focal plane; Angle = angle between electron path and focal plane; cm/%E_0 = dispersion in units of cm per percent of the incident energy

k (GeV)	Bend (deg)	Drift (m)	Angle (deg)	cm/%E_0 perp.to ray	cm/%E_0 along FP
6	17.29	3.19	9.24	1.59	9.90
7	17.95	2.89	9.90	1.77	10.30
8	18.89	2.56	10.84	2.04	10.86
9	20.31	2.20	12.26	2.49	11.71
10	22.79	1.77	14.74	3.36	13.21
11	28.66	1.23	20.61	5.91	16.78

[2] *SVN revision ID:* tdr_summary_taggermagnet.tex 13854 2014-06-12 04:42:15Z gen

2.2.3 Tagger Microscope

Tagger Microscope Summary [3]

The main parameters and properties of the Tagger Microscope (TAGM) are given in Tables 2.5 and 2.6. The assembly drawing for the tagger detectors installation is D000000002-1008.

Table 2.5: TAGM properties.

Item	Value
Energy range, E_γ	8.1 - 9.1 GeV
Energy resolution (r.m.s.)	5 MeV
Maximum counter rate	3 MHz
Number of scintillators	array of 102×5
Scintillator fibers	2×2 mm^2 BCF-20
Scintillator fiber length	20±2 mm
Light guide fibers	2×2 mm^2 BCF-98, ≈1 m long
Operating temperature	20°C, forced air cooling

Table 2.6: TAGM channel counts.

Item	Description	Quantity
Light sensor	Hamamtsu S10931-050P MPPC (50 μm pixel size)	510
MPPC Bias supply	Wiener MPV8120l MPOD	1
Readout channels	97 (column sums) + 5 individual columns	122
Flash ADCs	JLab fADC250-MHz, 16 ch	8
Discriminator	JLab leading edge, 16 ch	8
TDCs	JLab F1TDC V2, 32 ch, 60 ps	4

[3] *SVN revision ID:* tdr_summary_microscope.tex 13854 2014-06-12 04:42:15Z gen

2.2.4 Tagger Hodoscope

Tagger Hodoscope Summary [4]

The main parameters and properties of the Tagger Hodoscope (TAGH) are given in Tables 2.7 and 2.8. The assembly drawing for the tagger detectors installation is D000000002-1008. The assembly drawing for the TAGH counter is D000000103-1030.

Table 2.7: TAGH properties.

Item	Value
Energy range, E_γ	
continuous coverage	9.1 - 11.78 GeV
$30-50\%$ sampling	3.048 - 8.1 GeV
Total number of counters	218 originally installed (mounting slots for 274 counters)
Counter energy bin ΔE_γ (MeV)	
counter 1-22 (21 mm wide)	10.2 - 23.7
counter 23-40 (16 mm wide)	18.4 - 29.5
counter 41-64 (10 mm wide)	18.7 - 26.8
counter 65-81 (8 mm wide)	21.7 - 26.0
counter 82-131 (5 mm wide)	16.4 - 22.2
counter 132-151 (4 mm wide)	16.6 - 17.2
counter 152-218 (3 mm wide)	13.7 - 20.3
Scintillator thickness/height	6×40 mm^2
Scintillator material	EJ-228
Maximum counter rate	3 MHz
Light guide type	cylindrical shape, UVT PMMA

Table 2.8: TAGH channel counts.

Item	Description	Quantity
Light sensor	Hamamtsu R9800 PMT JLab designed divider, divider based amplifier (gain ~ 8) two signal outputs	218
HV for PMTs	CAEN A1535SN, 24 ch	10
Flash ADCs	JLab fADC250-MHz, 16 ch	15
Discriminator	JLab leading edge, 16 ch	15
TDCs	JLab F1TDC V2, 32 ch, 60 ps	8

[4] *SVN revision ID:* tdr_summary_hodoscope.tex 13854 2014-06-12 04:42:15Z gen

2.3 Pair Spectrometer

2.3.1 Pair Spectrometer Magnet

Pair Spectrometer Magnet Summary [5]

The main parameters and properties of the Pair Spectrometer Magnet are given in Table 2.9. The assembly drawing for the Pair Spectrometer Magnet is D000001500-1000.

Table 2.9: Pair Spectrometer magnet properties.

Item	Value
Magnet type 18D36	Water-cooled dipole
Maximum current	1375 A
Nominal field for 12 GeV endpoint, at the center	1.8 T
Current at 1.8 T	990.0 A
Coil power at 990 A	29.7 kW
Radius of curvature at B=1.8T, E_{e^+/e^-}=6 GeV	11.14 m
Deflection at B=1.8T, E_{e^+/e^-}=2.8 GeV	9.9°
Number of coil turns	52
Coil resistance (upper/lower/total) at 22.2°C	15.20/15.11/30.31 mΩ
Original gap height/width/length	6 inch / 18 inch / 36 inch
2 iron pole tips added height/width/length	3.89 cm / 45.47 cm / 91.4 cm
2 iron pole tips material	AISI 1006
Modified gap height/width/length	7.62 cm / 45.7 cm / 91.4 cm
Iron yoke size height/width/length	110.5 cm / 209.6 cm / 91.4 cm
Coils dimension along Z-axis	118.9 cm
Original design weight	17.5 US tons (Copper: 1.1 ton)

[5] *SVN revision ID:* tdr_summary_psmagnet.tex 13854 2014-06-12 04:42:15Z gen

2.3.2 Pair Spectrometer Detector

Pair Spectrometer Detector Summary [6]

The main parameters and properties of the Pair Spectrometer Detector are given in Tables 2.10 and 2.11. The assembly drawing for the high-granularity counters is D000001500-1007.

Table 2.10: Pair Spectrometer properties.

Item	Value
High-granularity hodoscope (PS)	
E_γ energy range	6. - 12.5 GeV
$e^\pm$ energy range (two detector arms)	3. - 6.25 GeV
E_γ energy resolution	$\sim$ 30 MeV
Converter thickness	$5 \cdot 10^{-4}$ - 10^{-2} X_0 (TBD)
Rate per counter for (10^{-3} X_0 converter)	$>$ 1kHz
Number of scintillator tiles per detector arm	
tiles 1×10×30 mm^3 EJ-212	40
tiles 2×10×30 mm^3 EJ-212	105
Light collection	1×1 mm^2 double-clad WLS fibers, BCF-92
Low-granularity counters (PSC)	
Number of counters per detector arm	8
Scintillator size	2×4.4×6 cm^3, EJ-200
Light Collection	Fish-tail light-guide, UVT PMMA

Table 2.11: Pair Spectrometer channel counts.

Item	Description	Quantity
High-granularity counters (PS)		
Light sensor	Hamamatsu S10931-050P MPPC (50 μm pixel size)	2×145
MPPC bias	ISEG EHS 201P-F-K, 16 ch, 10 mA for 5 MPPC/ch	4
MPPC LV	MPOD MPV8008, 8 ch	1
Operating temperature	room temperature, air cooling	
Flash ADCs	JLab fADC250-MHz, 16 ch	19
Low-granularity counters (PSC)		
Light sensor	Hamamatsu H7415 PMT assembly with tapered divider	
Flash ADCs	JLab fADC250-MHz, 16 ch	1
Discriminator	JLab Leading edge discriminator, 16 ch	1
TDCs	JLab F1TDC V2, 32 ch, 60 ps	1

[6] *SVN revision ID:* tdr_summary_ps.tex 13854 2014-06-12 04:42:15Z gen

Chapter 3

The GlueX Detector in Hall D

The spectrometer has been optimized for experiment GlueX with the primary goal to search for new exotic meson states. Hybrid mesons decays are expected to provide several particles in the final state, mostly charged pions and photons. The meson spectroscopy based on Partial Wave Analysis (PWA) requires a nearly-hermetic detector for these secondary particles.

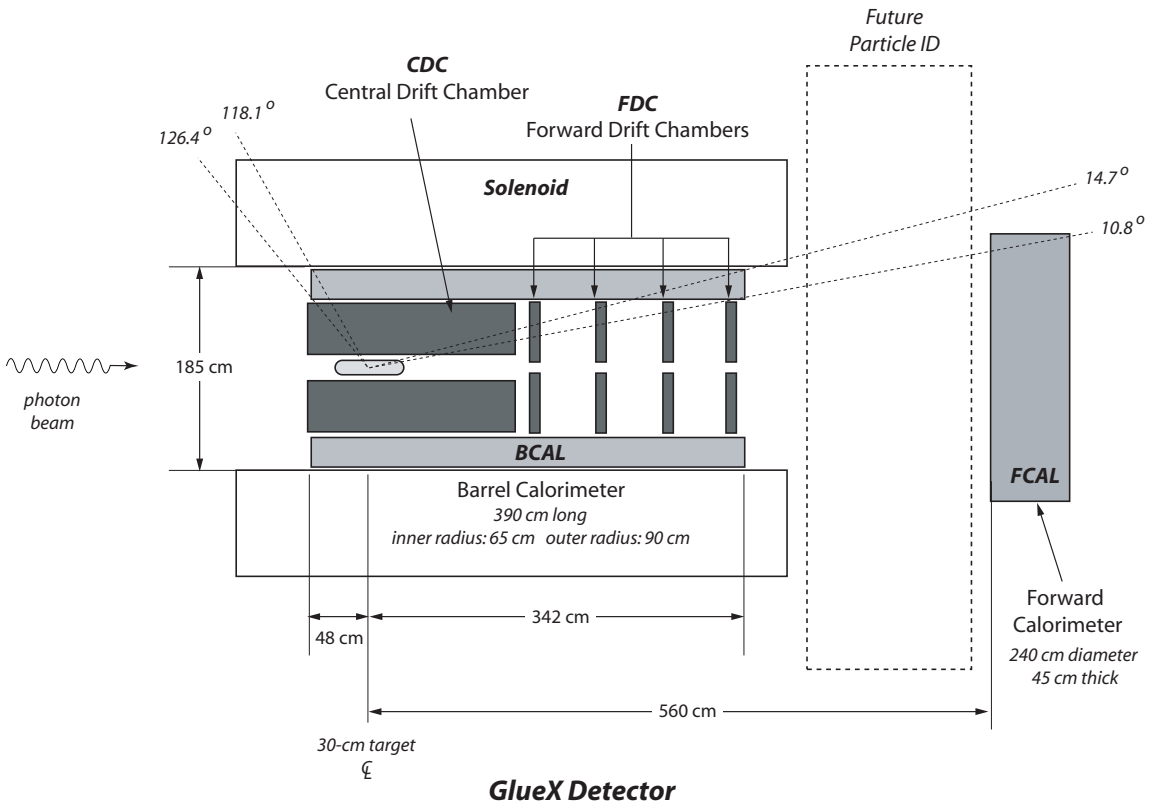

Figure 3.1: The spectrometer schematics.

In order to acheive the desired hermiticity as well as the needed momentum and energy resoultuons, the GlueX detector utilizies a solenoidal magnet with a central magentic field of

about $2\,T$. The bore of the magnet is about $4\,m$ long and $2\,m$ in diameter and has been centered on the photon beamline. The nominal position of the $30\,cm$ long liquid hydrogen target is $65\,cm$ into the magnet from its upstream end. A small fraction of the incident photons interact in the hydrogen target, and the resulting events are recorded by the GlueX detector.

Surrounding the hydrogen target is the start counter. This device consists of 30 narrow scintillator paddles aranged in a cylindrical shape with a cone-shaped nose. The detctors are readout at the upstream end using silicon photomultipliers (SiPMs). The resulting signal from charged particles passing through the start counter are used both in the level-1 hardare trigger, and in offline reconstruction to determine the interaction time of the event.

The start counter is located in the bore of the central drift chamber (CDC). The CDC is a $1.5\,m$ long, $1.20\,m$ diamter strawtube drift chamber. The straws are arranged in 28 layers, with groups of layers alternating between axial (along the beam) and $\pm 6^\circ$ stereo layers. The trajectories of charged particles are measured with an accuracy of $\sim 150 \mu m$ in the radial direction, and about $1\,mm$ along the beam axis. The curvature of the tracks in the known magnetic field allows us to measure the momentum of the particles. Most of the charged particles detected in the CDC are have their momentum measured to an accuracy of 1–2%. For tracks that cross at least 10 layers in the CDC, the coverage in polar angle extends from about 20° to about 150°.

The CDC is in the upstream half of the solenoid, while in the downstream half of the solenoid, charged tracking is carried out by the forward drift chambers (FDC). There are four FDC packages arranged along the beam axis, each of which contains six separte drift chamber layers oriented with 60° rotations between adjacent layers. The chambers have cathode strips and anode wires, both of which are read out. Each package is designed to reconstruct short track segments, with positions measured to an accuracy of about $200\,\mu m$. The momentum resolution of the charged particles detected by the FDC depend strongly on their momentum and polar angle. The FDC measures tracks with polar angles going from about 1° out to about 25°.

Charged particles that exit the FDC at the downstream end of the solenoid travel to the time-of-flight wall. This detector is a crossed pair of scintilator planes, readout at both ends by photo multipliers. The detector records the time at which charged paricles pass through it with about $80\,ps$ accuracy, and when this is combined with the time of the start of the event and the momentum of the particle, both the path-length traveled by the particle and its flight time can be determined. The accuracy of this decetor is sufficient determine if the particle is a $\pi^\pm$ or $K^\pm$ up to momentums of about $2\,GeV/c$. Particles with polar angles more forward than about 11° are measured by the time-of-flight wall.

In order to be able to reconstruct π° and η mesons, the GlueX detector must be able to detecect and reconstruct photons. This is carried out by a pair of calorimeters. The barrel calorimeter (BCAL) is located inside the bore of the magnet outside the radiuse of the CDC and FDC. The forward calorimeter (FCAL) is located downstream of the time-of-flight wall.

The BCAL is built with scintilating fibers between thin sheets of lead formed into 48 wedge-shaped modules that run the lnegth of the solenoid. The $4\,m$ long wedges form a ring against the inner bore of the solenoid, and are read out at both the upstream and downstream ends using SiPMs. For each module, the readout is broken into four progressively thicker layers as one moves outward radially. The BCAL detects photons of energy larger than $50\,MeV$ between polar angles of 11° back to about 160° with an energy resolution of about 6% at 1 GeV. The BCAL also accurately measures the arrival time of both photons and charged particles to an

accuracy of about $250\,ps$.

The FCAL is built with 2800 leadglass blocks stacked in a circular array. The glass is readout using photomultiplier tubes. Photons with energy larger than $100\,MeV$ and polar angles between 1° are 11° are reconstructed with an energy resolution of about 6% at 1 GeV. The arrival time of the photons is measured with nanosecond accuracy.

3.1 Superconducting Solenoid

3.1.1 Solenoid Summary [1]

The superconducting solenoid is used as the spectrometer magnet and also contains the e^+e^- pairs produced by the photon beam in the target and other material inside. The magnet consists of 4 separate coils, each in its own helium bath and in its own vacuum vessel, and of an iron yoke. The cryogens are delivered from a distribution vessel above the magnet. The assembly drawing for the solenoid is D000000402-1000.

Table 3.1: The main parameters of the superconducting solenoid.

	Value	
Inside diameter of coils	80 in	203.2 cm
Clear bore diameter	73 in	185.4 cm
Overall length along iron	479.5 cm	
Number of turns	4608	
Operating temperature (actual)	4.5°K	
Maximal allowed current at 4.5°K	1350 A	
Nominal current at 4.5°K	1300 A	
Maximal central field at 1350 A	2.08 T	
Inductance at 1350 A	26.4 H	
Energy at 1350 A	24.1 MJ	
Total conductor length	117600 ft	35.84 km
Total conductor weight	29000 lbs	13.15 t
Substrate material	Copper	
Copper-to-filament ratio (grade A)	20:1	
Copper-to-filament ratio (grade B)	28:1	
Number of separate coils	4	
Longitudinal arrangement of coils	2-1-3-4	
Turns per coil 1 / conductor grade	1428	B
Turns per coil 2 / conductor grade	928	B
Turns per coil 3 / conductor grade	776	B
Turns per coil 4 / conductor grade	1476	A
Coil resistance at $\sim$ 300°K	15.3 Ω	
Coil resistance at $\sim$ 10°K	$\sim$0.15Ω	
Coil cooling scheme	helium bath	
Total helium volume (including reservoir)	3200 ℓ	
Protection circuit limiting voltage	90 V	
Protection circuit resistor	0.061 Ω	
Inside iron diameter	116 in	294.6 cm
Outside iron diameter	148 in	375.9 cm
Full weight	284 t	

[1] *SVN revision ID:* tdr_summary_sol.tex 13854 2014-06-12 04:42:15Z gen

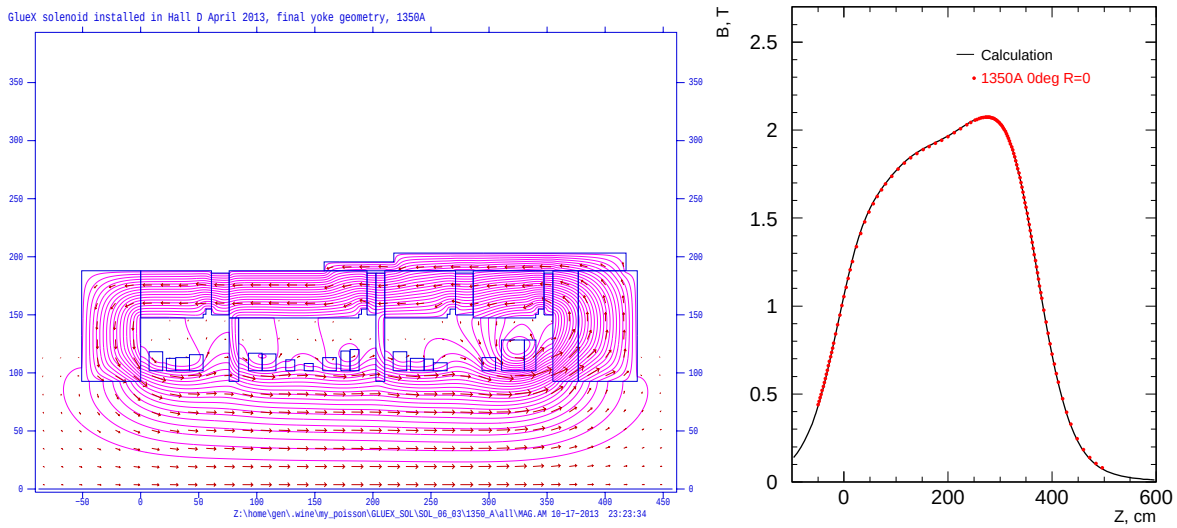

Figure 3.2: Magnetic field for the Hall D configuration at 1350 A computed with Poisson [2] (left). The conductor and the yoke configuration is shown. The calculated field on the axis and the results of the measurements at 1350 A (right).

3.1.2 Overview [2]

The solenoid, a superconducting magnet provides a ∼2 T magnetic field parallel to the beam direction at the center of the magnet. The diameter of the clear bore is 185.4 cm (73 inch) and the yoke's overall length is 479.5 cm. At 1350 A the coil inductance is 26.3 H resulting in a stored energy of 24 MJ. The iron and conductor configuration is shown in Fig. 3.2 with the calculated magnetic field lines superimposed.

A detailed description of the magnet and the supporting systems is given in [1] and references therein.

The magnet was designed and built at SLAC in the early 1970's using standards that today would be considered very conservative. It is a cryostatically stable design and uses cryostats that were designed to be opened and serviced with hand tools.

The solenoid is constructed of four separate superconducting toroidal coils and cryostats. The coils are connected in series. A common liquid helium reservoir is located atop the solenoid providing the gravity feed of the liquid to the coils. The layout of the coils' cryostats and the flux return iron yoke is shown in Fig. 3.3.

Table 3.1 summarizes the important magnet parameters.

Before installation in Hall D all the coils were tested individually in 2010-2012 [3]. During the full magnet tests in April-May 2013 the magnet once reached the target current of 1500 A but quenched at 1460 A at the next try. The operation conditions have been re-evaluated and the nominal operation current was reduced from 1500 A to 1350 A to provide enough operations margin. The magnet was successfully tested and the field was mapped at 1350 A and 1300 A.

[2] *SVN revision ID:* sol_note.tex 13933 2014-06-23 00:17:25Z gen

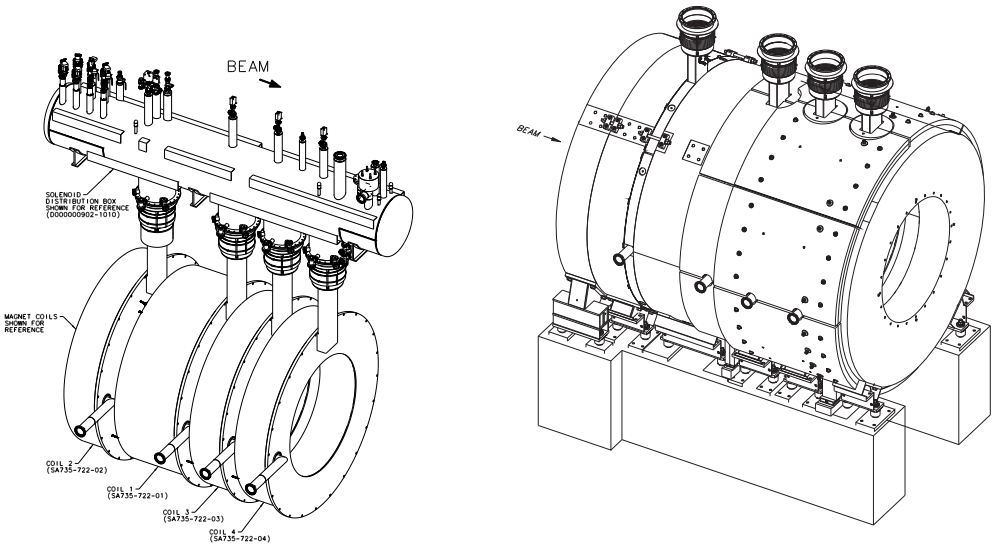

Figure 3.3: The magnet consists of 4 separate coils, each in its own vacuum vessel, and of an iron yoke. Each of the coils is connected to a common helium reservoir through a chimney. The power cable and the instrumentation cables pass through the chimneys.

3.1.3 Subsystems

Conductor

The superconductor composite is made of niobium–titanium filaments[3] in a copper substrate, twisted and shaped into a $\sim$7.62$\times$1 mm^2 rectangular band. The laminated conductor is made by soldering the superconductor composite band between two copper strips[4] to form a rectangular cross section 7.62$\times$5.33 mm^2 (0.30$\times$0.21 inch^2) [5]. The measured resistivity ratio of the conductor at $\sim$ 300°K and $\sim$ 15°K is RRR$\approx$ 100. Two types of filaments have been used (see Fig. 3.4 and Table. 3.2). The Grade A conductor provides a higher current limit than the Grade B conductor and is used in the area of the highest magnetic field (Coil 4).

The coil was wound on G-10 standoff strips glued on the cylindrical inner wall of the liquid helium vessel. As the coil was wound, a 0.025 inch-thick stainless steel support band and two 0.0075 inch-thick Mylar insulating strips were wound along with it for pre-tensioning and insulation (Fig. 3.4). Cooling by the liquid helium is accomplished from the shorter (5.33 mm) sides of the cable.

Short samples of the Grade A and B cables have been measured at SLAC during the coils' construction [1] .

[3]The critical temperature is about 10°K.

[4]Copper CDA 102. Average Resistivity Ratio for 300°K:4.2°K is a minimum of 150:1, claimed by the builders of the magnet [4]. Our measurements show RRR$\approx$ 100.

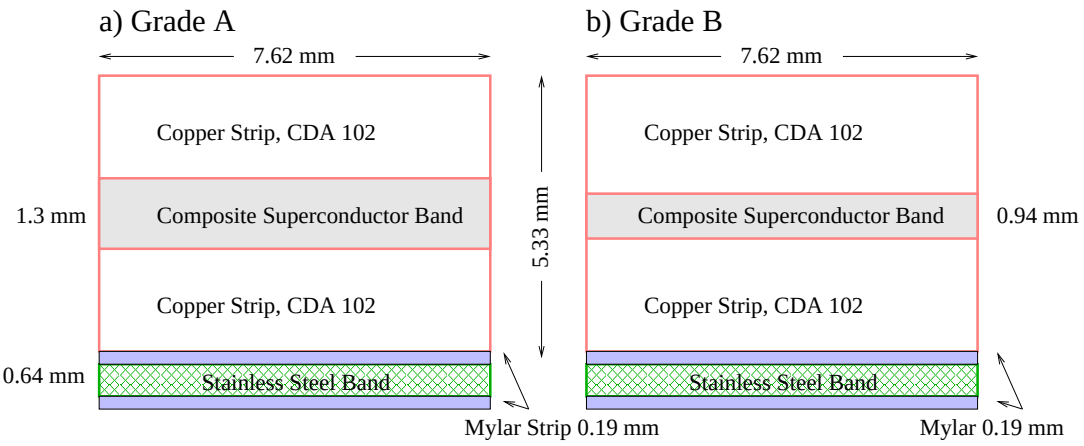

Figure 3.4: The conductor cable consisting of a superconducting composite sandwiched between copper strips is co-wound with a stainless steel band and two Mylar strips for insulation. Two cable types are used.

Conductor	Filaments			Composite Band		Cable	Coils
	#	diameter	360° twist	thickness	NiTi/Cu	NiTi/Cu	used
Grade A	87	178 μm	15 cm	1.30 mm	1:4	1:20	4
Grade B	87	127 μm	15 cm	0.94 mm	1:4	1:28	rest

Table 3.2: Parameters of the conductor.

Coils

Each of the coils has unique construction and winding patterns leading to a relatively uniform, but slightly increasing field from upstream to downstream. The modifications in the return iron yoke made at JLab lead to an increase of the axial magnetic forces on the most upstream coil with respect to the original design (see [1]). The force would be too high for Coil 1, while acceptable for Coil 2 which has fewer turns. Therefore, Coils 1 and 2 were swapped.

Each of the coils consists of a number of subcoils. Each subcoil contains a number of "double pancakes" with the same number of turns (see Table 3.3). Each double pancake is made from a single piece of conductor. The crossover within double pancakes is at the inner diameter and the splices from double pancake to the adjacent double pancake are on the outer diameter, a region of lower field. Spacer strips separate the non-insulated conductor surfaces on the faces of the pancakes, allowing direct cooling with liquid helium (Fig. 3.5). These insulation methods and piping/vessel construction methods are unique to the early days of large superconducting magnet construction.

The construction of each coil is similar, with a central flange dividing the coil volume into two zones seen in Fig. 3.6. The upstream zone is smaller and its helium volume is considered an antechamber to the downstream chamber. The antechamber is connected to the downstream chamber by 5.0×2.2 cm^2 passages at 3:00, 6:00, 9:00 and 12:00 o'clock. The passages at 3:00 and 12:00 are restricted by Micarta insulator to 2.9×0.74 cm^2 where conductors pass through. The downstream zone contains more subcoils and contains the larger store of helium as well

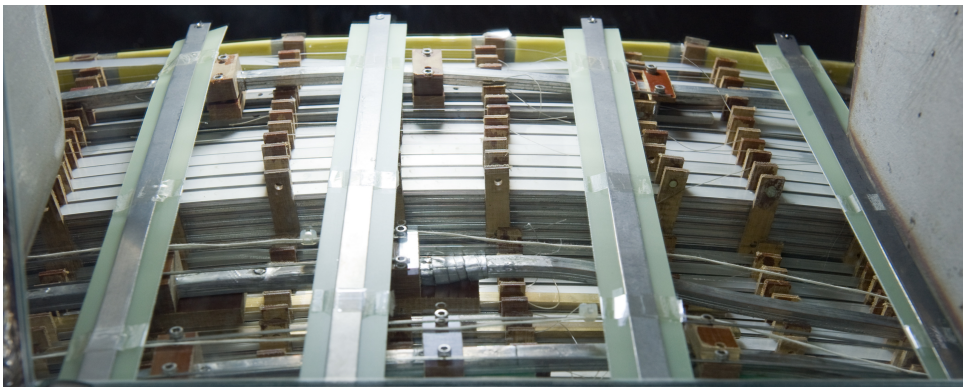

Figure 3.5: Coil 2: Looking downstream at the support straps for the wave spring compression rods. Poorly supported turns of the downstream-most subcoil are visible along with several inter–double pancake leads and splices,

as the access tubes from the cryogenic supply/return that contain the electrical leads. During powering, the forces on the subcoils tend to compress them axially toward the central flange.

The coil is supported within its cryostat vacuum vessel in the axial direction by a series of axial columns mounted between the outside projection of the central flange and the base flange of the vacuum vessel. That flange in turn is mounted to the inner edge of the yoke. Radial support is provided by four columns mounted in a pinwheel pattern between the helium vessel and the outer vacuum vessel shell. The columns are made of two concentric stainless steel tubes and a central rod of titanium. A thermal intercept from the liquid nitrogen shield is attached to the outermost tube near the room temperature end. The resulting long length of low thermal conductivity materials between intercept and helium vessel leads to a low heat leak.

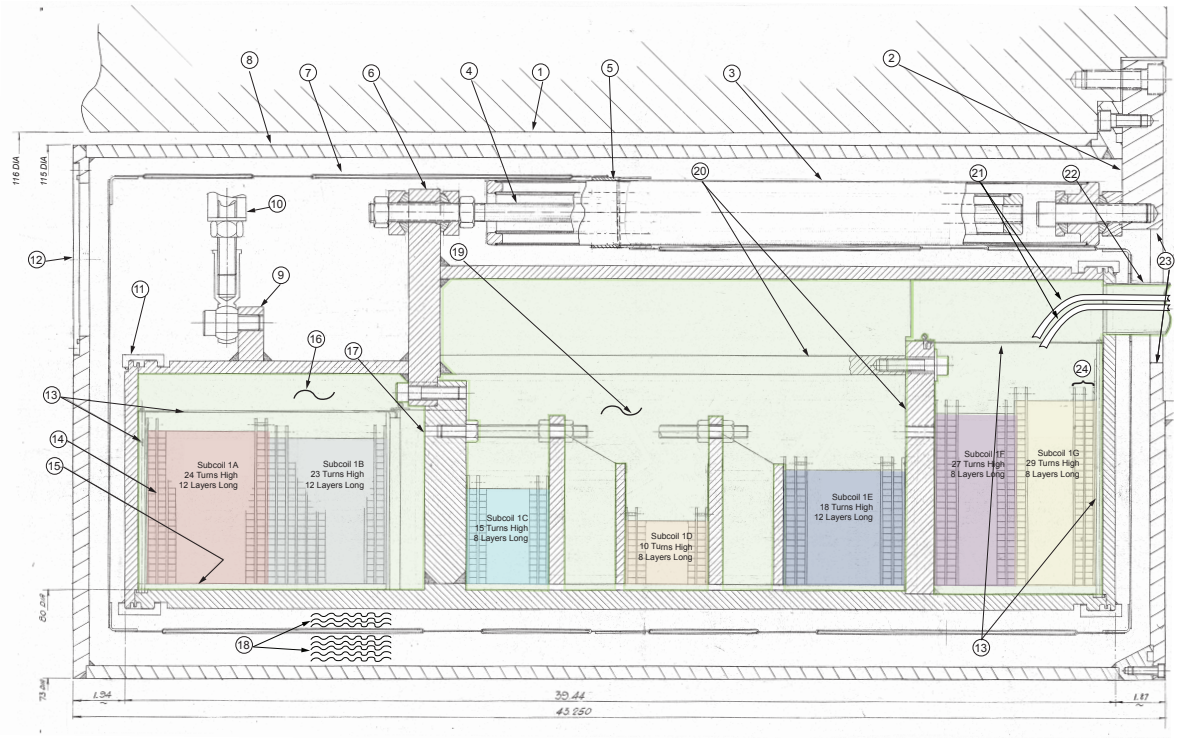

Figure 3.6: The cross section of the Coil 1.

1 Magnet Yoke
2 Base Flange Vacuum Vessel
3 Typical axial Support Column
4 Titanium Rod
5 Column's LN2 Intercept
6 Outside Projection of the Central Flange
7 LN2 Shield
8 Cryostat Vacuum Vessel
9 Radial Support Anchor on Helium Vessel
10 Radial Support Column
11 Vacuum Type Seal Weld and Clip System Closure of Helium Vessel
12 Radial Support Access Port (Also Vacuum Relief Valve Position)
13 Wave Spring Compression System and Rod Support Strap
14 Spacer Strip
15 G-10 Stand-Off Strips
16 Upstream Antechamber and Liquid Helium Volume
17 Central Flange for Coil Support
18 Superinsulation
19 Downstream Chamber and Main Liquid Helium Volume
20 Downstream Coil Support Web and Flange system
21 Coil Leads in One Tube
22 Two 2-inch Tubes into Chimney
23 Opening in Base Vacuum Flange leads to Chimney
24 Double Pancake (Typical)

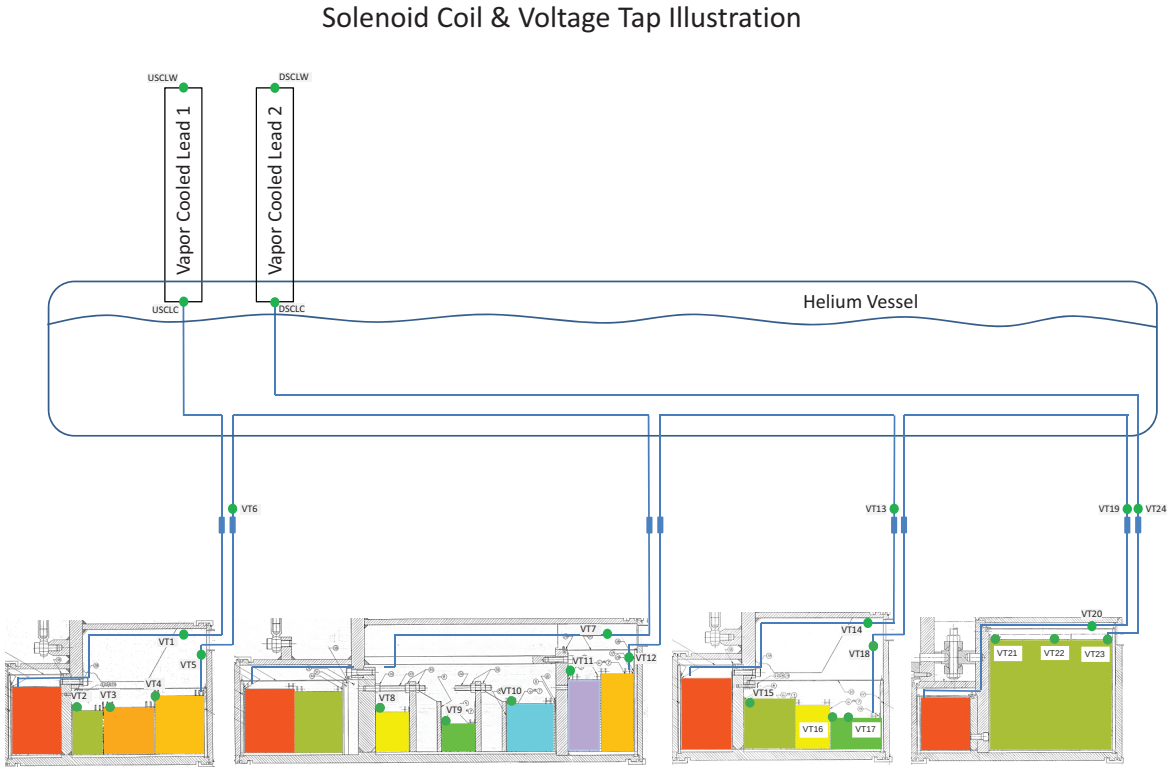

Figure 3.7: The coils and the tap wire locations and destinations.

A copper, liquid nitrogen cooled shield, made of hollow copper waffle panels on the circumferential surfaces and copper sheet on the flat surfaces provides the heat intercept to minimize thermal radiation heat leak to the helium. Splits in the electrical continuity of the panels prevent them from forming a single electrical turn. Super-insulation is placed between vacuum vessel and nitrogen shield and between nitrogen shield and helium vessel to further minimize heat leak.

Voltage taps allow monitoring of the voltage across subcoils as well as the bus between coils and the vapor cooled leads. The position where the voltage taps are connected is not simply at the subcoils junctions, but rather occasionally straddles two subcoils or sometimes several voltage taps monitor one subcoil. Turns in each subcoil and the voltage tap read-out scheme are outlined in Fig. 3.7 and Table 3.3[5].

[5] The electrical schematic available at the URL: D000001613-1112.

Coil	Turns	Sub	Turns structure			R_{min}	R_{max}	Z_{min}	Z_{max}	Voltage taps and read-out channels			
		coil	N_Z	N_R	N_{tot}	cm	cm	cm	cm	tap-1, vtt	tap-2, vtt	channel, vtt	turns
		vapor-cooled lead - bottom - jumper cable								usclc	1	3	0
		short cable								1	2	4	312
2	928	2A	12	26	312	101.88	118.22	7.68	19.39				
		2B	8	17	136	101.88	112.53	22.56	30.29	2	3	5	172
		2C	12	18	216	101.88	113.16	30.52	42.24	3	4	6	180
		2D	12	22	264	101.88	115.69	42.47	54.19	4	6	7	264
		splice								5	8	8	564
		jumper cable, splice								6			
		short cable								7			
1	1428	1A	12	24	288	101.88	116.95	92.88	104.59				
		1B	12	23	276	101.88	116.32	104.85	116.57				
		1C	8	15	120	101.88	111.26	125.04	132.77	8	9	9	120
		1D	8	10	80	101.88	108.10	140.94	148.67	9	10	10	80
		1E	12	18	216	101.88	113.16	156.84	168.55	10	11	11	216
		1F	8	27	216	101.88	118.85	172.49	180.22	11	14	12	448
		1G	8	29	232	101.88	120.11	180.46	188.19				
		jumper cable, splice								12			
		splice								13	15	13	312
		cable								14			
3	776	3A	12	26	312	101.88	118.22	217.82	229.54				
		3B	12	17	204	101.88	112.53	232.71	244.42	15	16	14	332
		3C	8	16	128	101.88	111.89	244.66	252.39	16	17	15	44
		3D	12	11	132	101.88	108.73	252.62	264.34	17	20	16	88
		jumper cable, splice								18			
		splice								19	21	17	216
		short cable								20			
4	1476	4A/B	12	18	216	101.88	113.16	294.72	306.43				
		4C	20	42	840	101.88	128.33	311.51	331.27	21	22	18	672
		4D	10	42	420	101.88	128.33	331.27	341.15	22	24	19	588
		splice								23	24	20	0
		jumper cable to the bottom of the vapor-cooled lead								24	dsclc	21	0

Table 3.3: Each of 4 coils consists of several subcoils. Each subcoil consists of several "double pancakes" of the same radial dimensions. N_Z is the number of "pancakes" in the subcoil, N_R is the number of turns in the "pancake", N_{tot} is the full number of turns in the subcoil. The subcoil boundaries for the Hall D geometry are presented, calculated using the positions of the yoke rings (see Table 3.4). The tap wires come out of the cold volume in order to measure the voltage across a channel between taps. Column "tap-1" shows the tap coming from the start of the given segment. Voltages between "tap-1" and "tap-2" are read out, and the column "turns" indicates the number of conductor turns in between.

Flux Return Iron Yoke

A ∼236 t iron flux return path consists of [6]:

1 The original 4 cast (1010 steel) yoke rings - the holders for the coils.

2 The original 2 cast (1010 steel) end-plate rings. The upstream ring was modified by boring its original 8-inch radius to 36.5 inches radius.

3 4 filler plates (1018 steel) to fill the 6-inch gaps in the original yoke left for detectors and for the coil chimneys. Two filler plates are 3-inch thick

4 A baffle (1018 steel) added to reduce the axial forces on the coils nearby.

5 Two hybrid filler-baffle plates (1018 steel) to fill the gaps and reduce the axial forces on the coils. The second 9-inch thick plate also reduces the magnetic saturation in the downstream end plate.

6 Two cladding layers (1018 steel) to reduce the saturation in the yoke and the fringe field in the hall. Two gaps are left for the feet of the yokes: from 27.5 to 47° each, measured from the downward direction.

6 In contrast with the SLAC geometry, the iron rings are tight. It occurred that the flanges of Coils 2 and 4 stick out of their sockets in the yoke rings. Two steel shims were added to cover the flanges.

6 Post-installation measurements revealed small gaps left between some of the iron rings.

The geometry and the dimensions are shown in Fig. 3.3, 3.8, 3.9, and Table 3.4.

[6] The yoke assembly is shown on Assembly Drawing D000000402-1000 see.

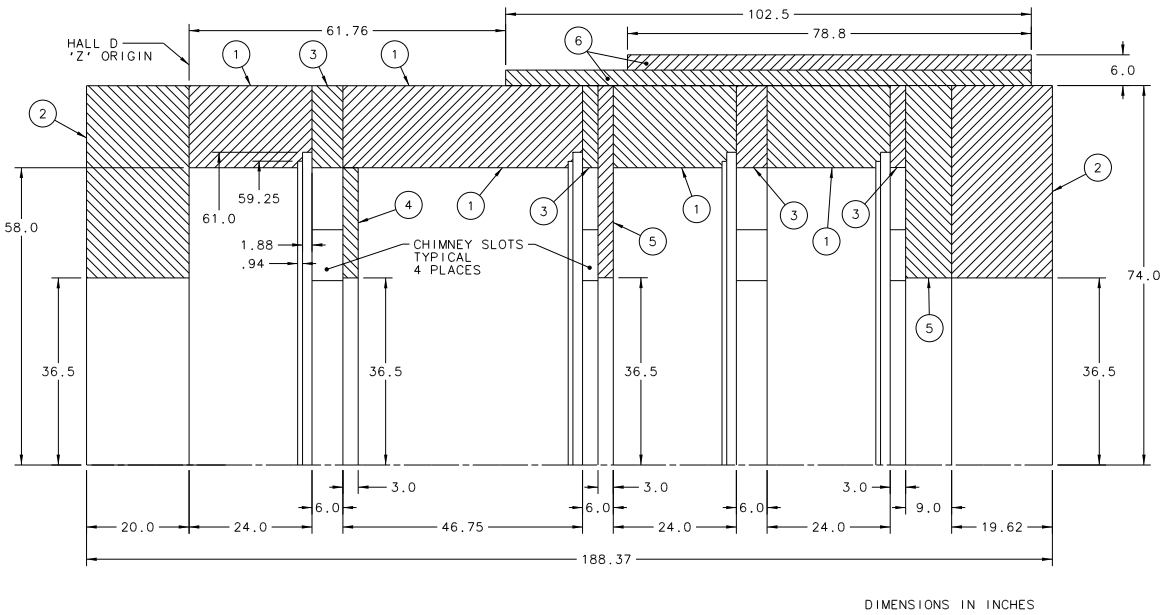

Figure 3.8: The yoke cross section at 45°. The dimensions are in inches. The picture presents the "ideal" geometry. Post-installation measurements revealed deviations in the longitudinal direction from the "ideal" dimensions and positions. Also, two shims have been installed. Table 3.4 shows the results of the measurements.

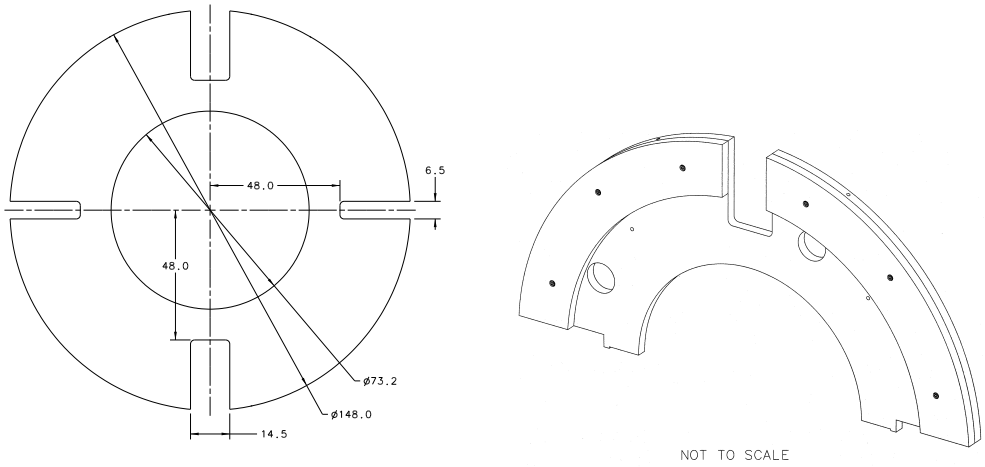

Figure 3.9: The hybrid filler-baffle plate 1 with the cutouts for the chimney and the vacuum pipe (left). In order to improve the azimuthal symmetry of the field, the cutouts are made symmetric with respect to the solenoid axis. The assembly of the hybrid plate with the filler plate parts (right). The filler plates are built of 4 pieces, the hybrid plates are built of two pieces (top and bottom). The dimensions are in inches. The cutouts in filler-baffle plate 2 are 3 inches deep.

Piece	R_{min} cm	R_{max} cm	Z_{min} cm	Z_{max} cm	Comment
Upstream end-plate	92.71	187.96	-50.800	-0.127	
Yoke for Coil 2	147.32	187.96	0.032	61.073	
Shim 1	154.94	187.96	61.124	61.441	Steel shim 0.125 inch
Filler plate 1	147.32	187.96	61.441	76.681	4 pieces
Yoke for Coil 1	147.32	187.96	76.681	195.020	
Filler plate 2	147.32	187.96	195.101	202.802	4 pieces
Filler-baffle plate 1	92.71	187.96	202.802	210.372	2 pieces
Yoke for Coil 3	147.32	187.96	210.453	271.540	
Filler plate 3	147.32	187.96	271.540	286.861	4 pieces
Yoke for Coil 4	147.32	187.96	286.861	347.903	
Shim 2	154.94	187.96	347.903	348.146	Steel shim 0.096 inch
Filler plate 4	147.32	187.96	348.146	355.848	4 pieces
Filler-baffle plate 2	92.71	187.96	355.848	378.748	2 pieces
Downstream end-plate	92.71	187.96	378.827	428.675	
Baffle 1	92.71	147.32	76.681	84.301	2 pieces
Cladding 1	187.96	195.58	156.87	417.22	2 gaps left
Cladding 2	195.58	203.20	217.07	417.22	for the feet

Table 3.4: The sizes and locations of the yoke parts, measured after installation. It was assumed that the coils 2 and 4 were shifted with respect to their yoke rings by the thickness of the shims.

Internal Cryogenic System

The Cryogenic Distribution Box[7], a series of vessels above the yoke is shown in Fig. 3.3 and 3.10. It provides utilities such as connection to the transfer line from the refrigerator, liquid helium, liquid nitrogen, vapor cooled lead mounting, bus bar between coils, instrumentation feedthrough points and relief valve venting. Connections from each coil up to the Distribution Box are made through a chimney. The insulation vacuum for individual coils is isolated from Distribution Box vacuum in the chimneys by a thin stainless steel bellows. Vacuum pumping of the coils is provided at the chimneys which have less restriction than the original Vacuum Pipes.

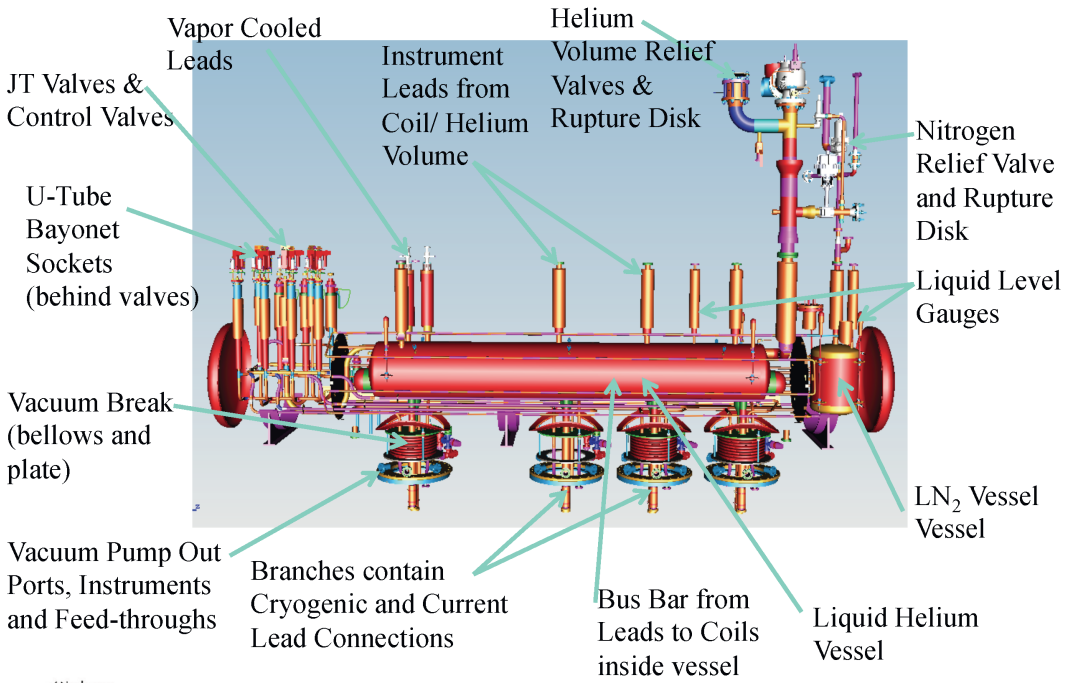

Figure 3.10: The Cryogenic Distribution Box internal features.

Cryogenic supply and control system

The cryogenic supply [6] for this Solenoid is not one of the central helium refrigerator at JLab, but rather a stand-alone, used, 80's era, CTI 2800 Helium Refrigerator located in an adjacent building. Three 18 atm[8] 18 g/s helium compressors supply the high-pressure gas to the refrigerator cold box. When at rated capacity, the refrigerator supplies 180 W of pure refrigeration or a mixture of refrigeration and liquefaction. The refrigerator uses a 1000 ℓ Dewar as a thermal flywheel. The 3 atm output fluid circulates through a heat exchange coil in the Dewar where the fluid is subcooled to near the liquid temperature in the Dewar. The supply fluid then flows to the Hall D Building through a transfer line to a Bayonet Can next to the Distribution Box described in Section 3.1.3.

[7] The Cryogenic Distribution Box Assembly Drawing and P&I drawings are listed in [1].
[8] Throughout this document the absolute values of pressure are implied.

During normal operation Cold Return Helium Gas at about the temperature in the Helium Vessel is regulated by another control valve and returns via the transfer line to the gas volume above the Dewar liquid and proceeds to the Refrigerator Cold Box. There, the cold gas flows through the counterflow heat exchangers, is warmed and goes back to the compressors for another cycle through the refrigerator. Back pressure due to restrictions in the counterflow heat exchangers limit the pressure on the return helium to 1.25 atm and hence the Distribution Box's Helium Vessel is limited to 4.47°K or higher. Provisions are built into the piping at the Dewar of the Refrigerator Building to augment cooling of the plant with portable 1000 ℓ Dewars.

Warm helium return gas from the leads amounts to 3.0 standard ℓ/s at 1350 A and represents 17% of the Refrigerator/Liquefier capacity. It returns to the refrigerator building through the warm helium return pipe. The gas may be recycled into the helium gas compressor system. If there is any indication of contamination, the warm helium gas is returned via the set of warm supply and return pipes leading to the Central Helium Liquefier Plant for purification.

The cryogenic supply system also delivers liquid nitrogen (LN2) at 77°K and 1.2 atm to the Distribution Box Nitrogen Vessel through the Transfer Line to the bayonet can and u-tube systems while acting as a thermal shield for that line. The LN2 Supply is a 1000-gallon Dewar outside the Refrigerator Building that is filled as needed by the tanker truck deliveries that supply all the Lab's cryo systems. Liquid Nitrogen is the source of the first stage of helium gas cooling in the refrigerator.

The cool-down process is stated in Hall D Specification: Hall D Solenoid Operating Narrative and controlled by Hall D Procedure Document: Solenoid Commissioning Plan in a form of checklists that match the Hot Check Out. The first stage of cooldown of the Solenoid is to thoroughly scrub the helium volume of contaminants by several vacuum pump downs followed by circulation of warm helium supply gas from the CHL and back to its purification system. The first part of the cooldown doesn't use the refrigerator but rather uses a portable heat exchanger cooled by Liquid Nitrogen. Temporary u-tubes divert LN2 to a vessel in the heat exchanger. Warm helium from the CHL Supply circulates through heat exchange tubing in the LN2 vessel creating a stream of $\sim$ 80°K helium gas. This gas is mixed with warm helium gas by a control valve to create a controlled 75°K difference in the temperatures of gas to the temperature of the Solenoid Coils. The cooled gas is injected into the small cool-down ports at the bottom of the coils. The flow to each coil is controlled by a separate control valve in the Distribution Box. This process cools the Coils to $\sim$ 100°K.

The second part of the cooldown is to engage the Refrigerator. The portable heat exchanger is removed from the cool down circuit and the LN2 and Helium U-Tubes are connected directly to the Distribution Box and the Bayonet Can. At this point, the helium supply is 3 atm, 5°K helium. Flow is established through the vapor cooled leads to reduce heat load. The super-critical helium is liquefied as it passes through each of the coil supply valves and the now 4.2°K Helium passes through each coil (still in parallel). The coefficients of thermal expansion are reduced by an order of magnitude at 100°K to 80°K, so excessive strains and motions are not expected and the temperature differentials maintained in previous steps are no longer necessary. The magnet continues to cool until the carbon resistor thermometers in each coil begin to indicate the presence of liquid helium. The resistance of carbon resistor thermometers makes a sudden transition to 300 Ω when in the presence of liquid helium. Once liquid is evident in the coils, the cryo group transitions the magnet from warm helium return to cold helium return. Cool down continues until the Liquid Helium Vessel in the Distribution Box begins to

fill as indicated by the LHe Liquid Level Gauge and the differential pressure liquid level gauge. Once the tank begins to fill, the valves to cool-down lines to the individual coils are closed and a control valve is opened to top-fill the Helium Vessel. Liquid helium level is controlled by the top fill valve.

The control system that controls the cryogenic valving for the magnet is completely new and based on Allen-Bradley PLC[9]. Most of the cryogenic system is common to all four coils. Specific to each coil are valves in the Distribution Box that control LN2 and LHe flow from the reservoirs to the individual coil cryostats, and temperature, strain and voltage sensors. We note that hard-wired interlock systems protect all relevant components from operating outside their allowed ranges, independent of PLC control.

Power Supply

The solenoid is powered by a new Danfysik System 8000 Type 854 10V DC power supply and energy dump system.

[9]The new control system allowing for PLC-based feedback control loops reduces the requirements to the capacity of the cryogenic supply in comparison with the old manual control system used at LASS and MEGA. Allen-Bradley PLCs are widely used at JLab.

3.2 Target

3.2.1 Target Summary [10]

The main parameters and properties of the target are given in Tables 3.5 and 3.6. The assembly drawing for the target is D000000300-0000.

Table 3.5: Liquid hydrogen target properties.

Item	Value
Target, conical	Liquid Hydrogen
Target length	30 cm
Upstream diameter	2.42 cm
Downstream diameter	1.56 cm
Target entrance window ⌀ (Kapton, 1.42 g/cm^3, 75 μm)	1.56 cm
Target exit window ⌀ (Kapton, , 1.42 g/cm^3, 75 μm)	1.56 cm
Super insulation	
Aluminized-Mylar+cerex (5 layers)	2.9 mg/cm^2 per layer
Scattering chamber (Aluminum 25 μm) exit window diameter	2.54 cm
Target cell, conical (not in beam path)	Aluminized Kapton, 127 μm
Super insulation (not in beam path)	
Aluminized-Mylar+cerex (5 layers)	2.9 mg/cm^2 per layer
Scattering chamber (not in beam path)	
Aluminum-lined Rohacell ($\sim$ 110 mg/cm^3)	9.44 cm OD, 7.49 cm ID
Distance from end of target to window	4.5 cm
Nominal center in detector coordinates	65 cm
Target pressure	16 psia
Nominal operating temperature	$\sim$18°K

Table 3.6: Additional target

Item	Description
Cryogenic targets	^{4}He, D
Solid targets	various solid targets

[10] *SVN revision ID:* tdr_summary_target.tex 13854 2014-06-12 04:42:15Z gen

3.2.2 Liquid Hydrogen Target [11] [12]

General Description

The Hall D cryotarget is a small kapton target cell containing liquid hydrogen (LH_2) or liquid deuterium (LD_2) at a temperature and pressure of about 18 °K and 18 psia. The cell, which is closely modeled on those utilized in Hall B for more than a decade, is a horizontal, tapered cylinder about 400 mm long with a mean diameter of 20 mm. Liquid hydrogen is introduced into the cell using a pair of 1.5 m long stainless steel tubes (fill and return) connected to a small, copper vessel where hydrogen gas is condensed. This condenser is cooled by a pulse tube refrigerator[13] (PTR) with a base temperature of 3 °K and cooling power of about 20 W at 20 °K. A 100 W temperature controller[14] regulates the condenser's temperature.

The entire target assembly is contained in an "L"-shaped, stainless steel and aluminum vacuum chamber with a Rohacell extension surrounding the target cell. The vacuum chamber, along with the hydrogen storage tanks, gas handling system, and control electronics, is mounted on a custom-built beamline cart for insertion into the Hall D solenoid. A Programmable Logic Controller (PLC) monitors and controls the performance of the target, while hardware interlocks on the target temperature and pressure and on the chamber vacuum ensure the system's safety and integrity.

A simplified schematic drawing of the target system is shown in Fig. 3.11, and a scale drawing of the target, with the insertion cart, is shown in Fig. 3.12.

Target Cell

A detailed drawing of the target cell is shown in Fig. 3.13. The cell is 5 mil (0.13 mm), aluminized polyimide (Kapton) foil wrapped into a tapered cylinder and glued along one edge. An extruded Kapton exit window is glued to the downstream end, and the upstream end is glued into an aluminum base. A polyimide-amide (torlon) tube is glued into the aluminum base and acts as a re-entrant window frame for a Kapton beam-entrance window. Stainless steel tubes for liquid hydrogen (fill and return) are also glued into the base. The epoxy[15] used for all glued joints has a long and successful track record for cryogenic use at Jefferson Lab. Two calibrated Cernox4 thermometers will be inserted into the cell to determine the temperature with better than 0.5% accuracy.

Prototypes for these cells have been constructed and pressurized to failure at room temperature. The burst pressure is typically around 200 psia. Based on the results of pull tests performed at 77 °K, the burst pressure of the cell at 18 °K will be significantly higher than at room temperature. However we do take credit for this in our pressure relief analysis. The operational pressure of the cell is about 35 psia at room temperature and about 18 psia when filled with LH_2. Redundant pressure relief valves, along with properly sized system plumbing, ensure that the cell pressure never exceeds 45 psia. All relief paths, including one on the vacuum chamber as well as all pump exhausts are directed to a dedicated hydrogen vent line installed in Hall D. This line terminates outside the hall and is continuously purged with an inert gas (nitrogen) to ensure that a flammable hydrogen/oxygen mixture does not exist inside the line.

[11] *SVN revision ID:* tcr_cryotarget.tex 13854 2014-06-12 04:42:15Z gen
[12] Author: C. Keith ckeith@jlab.org
[13] Cryomech Model PT415
[14] Lake Shore Model 336
[15] 3M Scotch-Weld DP-190 (gray)

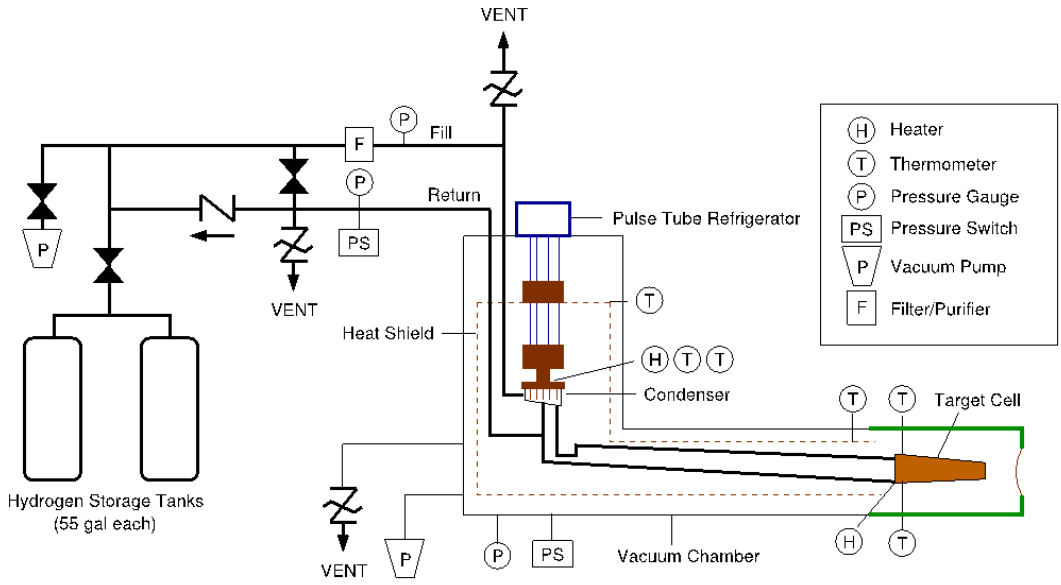

Figure 3.11: Highly simplified schematic of the target system. Not to scale. The Rohacell vacuum chamber extension is indicated in green. The photon beam travels from left to right in this figure.

Condensation of Hydrogen Gas

Room temperature hydrogen gas is introduced to the target from a pair of 55-gallon (208 ℓ) storage tanks located on the insertion cart and charged with an initial H_2 pressure of approximately 35 psia (2.3 atm). The gas is first cooled to approximately 80 °K by a copper heat exchanger in thermal contact with the first stage of the pulse tube refrigerator (PTR). The first stage of the PTR is also used to cool a copper heat shield that surrounds the condenser and the fill and return tubes to the target cell. The shield does not extend to the cell itself, which is instead wrapped with ten layers of superinsulation.

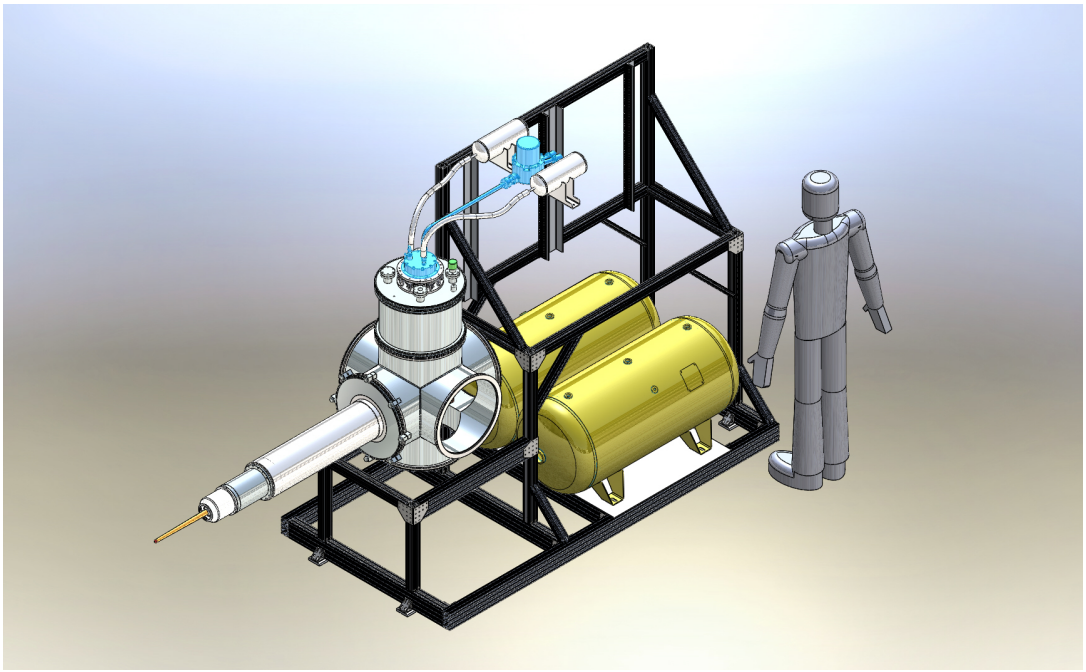

Figure 3.12: Scale drawing of the target assembly. The Rohacell extension is removed and the Kapton target cell is visible on the far left. The hydrogen storage tanks are yellow, and the pulse tube refrigerator is blue.

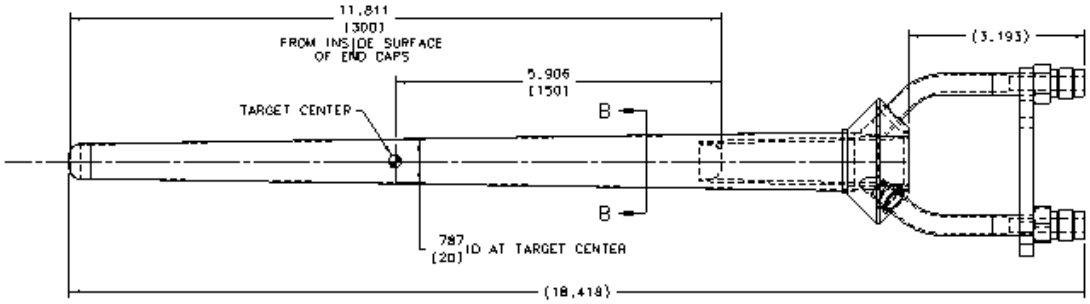

Figure 3.13: Hall D liquid hydrogen target cell.

3.3 Barrel Calorimeter

3.3.1 BCAL Summary [16]

The main parameters and properties of the BCAL are given in Tables 3.7 and 3.8, respectively. The assembly drawing for the BCAL is D000000107-1000.

Table 3.7: BCAL properties.

Property	Value
Number of modules	48
Module length	390 cm
Module inner/outer chords	84.0 mm/118.3 mm
Lead-scintillator matrix thickness	221.7 mm ($14.9X_0$)
Inner/outer Al plates thickness	8 mm/31.75 mm
Module azimuthal bite	7.5°
Total number of fibers	683000
Lead sheet thickness	0.5 mm
Kuraray SCSF-78MJ multi-clad fiber	1.0 mm
Pitch radial/lateral	1.18 mm/1.35 mm
Volume ratios	37:50:13 (Pb:SF:Glue)
Effective density	4.86 g/cm^3
Sampling fraction	0.095
Total weight	28 t
MPPC operating bias, $V_{br} \approx 75$ V	0.6-1.4 V above V_{br}
Operating temperature	5-25°C
Energy resolution, σ_E/E	$5.4\%/\sqrt{E} \oplus 2.3\%$
Time difference res., $\sigma_{\Delta T/2}$	70 ps/$\sqrt{E}$
z-position resolution, σ_z	1.1 cm/$\sqrt{E}$ (weighted)
Polar/azimuthal angle resolution	$\sim$ 8/8.5 mrad

Table 3.8: BCAL channel counts.

Item	Description	Quantity
Light guides	Trapezoidal, 10 types radially	$2 \times 4 \times 10 \times 48$
Light sensor	Hamamatsu 144 mm^2 S12045 MPPC	$2 \times 4 \times 10 \times 48$
Readout fADC	Sensors combined radially 1-2-3-4	$2 \times 4 \times 4 \times 48$
Readout TDC	Sensors combined radially 1-2-3	$2 \times 4 \times 3 \times 48$
Flash ADCs	JLab fADC250-MHz, 16 ch	96
Discriminator	JLab LE Discriminator, 16 ch	72
TDCs	JLab F1TDC V2, 32 ch	36
Monitoring	Blue LED Model SMS1105BWC, Bivar, Inc.	$2 \times 4 \times 10 \times 48$
Monitoring controllers	Athens-custom. One per 4 strings of ten LEDs	96
MPPC Bias supply	ISEG EHS 201P-F-K, 16 ch, 8 mA for 10 MPPC/ch	24
LV power	MPOD MPV8008, 8 ch, 5 A/ ch	8

[16] *SVN revision ID:* tdr_summary_bcal.tex 13854 2014-06-12 04:42:15Z gen

3.3.2 Introduction

The barrel electromagnetic calorimeter (BCAL) is a key component of the hermetic detector, built as a lead, scintillating fiber matrix at the University of Regina. It will be positioned immediately inside the solenoid, leaving a space of 2.7 cm radially between the two for supports and installation. This constrains the device's outer radius to be 90 cm, while its inner radius is fixed at 65 cm to allow adequate space for the CDC (see Section 3.6).

A principle goal of GLUEX calorimetry is to detect and to measure photons from the decays of π^0's and η's which, in turn, can come from the decays of produced mesons (normal or exotic) or possibly from excited baryons (N^* or Δ). The positions and energies of the photons must be determined to sufficient accuracy to allow for a complete kinematic reconstruction of the event. Adequate readout segmentation is required for an accurate determination of the azimuthal angle of tracks as well as for providing information on the energy deposition profile in depth, and for good cluster identification, while avoiding multiple occupancy. Detailed Monte Carlo studies [7, 8] indicate that the BCAL should be sensitive to photon energies in the range from 60 MeV to at least 2.5 GeV. Specifically, studies of the lowest energy photons in high-multiplicity reactions that are expected to yield exotic hybrids such as $\gamma p \rightarrow b_1(1235)\pi n \rightarrow 2\pi^+\pi^-2\pi^0 n$ indicate that an energy threshold of 60 MeV suffices. The device will also provide timing information for charged particles and thus contribute to particle identification (PID) in the central region, in conjunction with the CDC. The BCAL can further assist in PID by providing dE information.

The relevant parameters that determine the π^0 and η mass resolutions are the photon energy (E) and the polar and azimuthal position resolutions (σ_θ and σ_ϕ). The energy resolution (σ_E) depends on the number of photoelectrons (N_{pe}) yielded by the photosensors, based on the collected light. The photoelectron statistics are strongly dependent on the stochastic fluctuations of the energy deposited by the electromagnetic shower in the scintillating fibres of the calorimeter. In addition, N_{pe} depends on the fraction of photon shower energy deposited in the fibres, the efficiency with which the resulting scintillation light is captured in and transmitted down the fibre to the photosensor, and the photon detection efficiency of the photosensor. The photon position is determined by the readout segmentation in the azimuthal direction and in the z direction by the difference in arrival time (ΔT) of the scintillation light between the two ends of the barrel. The time difference ($\sigma_{\Delta T}$) resolution, and therefore the polar angle resolution, also depend on N_{pe}. These measurements assist in the reconstruction of the momentum of photons and PID for charged particles [9, 10].

The performance metrics for these quantities were set by simulating hadronic photoproduction at GLUEX energies using Pythia [11] and also by simulating several of the signature reactions expected to yield exotic mesons. These studies included a GEANT-based simulation [12] of the entire GLUEX detector response, including detector material and cabling, photon reconstruction and kinematic fitting. The Pythia simulations indicate that 70% of the produced photons with energies up to about 2 GeV will be incident on the BCAL. The photon population in the BCAL for one of the signature reactions, $\gamma p \rightarrow \eta\pi^0 p \rightarrow 4\gamma p$, where the distribution in $\eta\pi^0$ mass was generated uniform from 1.0 to 2.0 GeV/c^2 and uniform in decay angles, is shown in Fig. 3.14. The distribution of photons (dN/dz) is plotted as a function of position from the upstream end of the BCAL; the photons predominantly populate the downstream end of the BCAL. Also graphed is the average energy as a function of z with higher energy photons being more forward. The integrated thickness of the BCAL matrix, in number of radiation lengths,

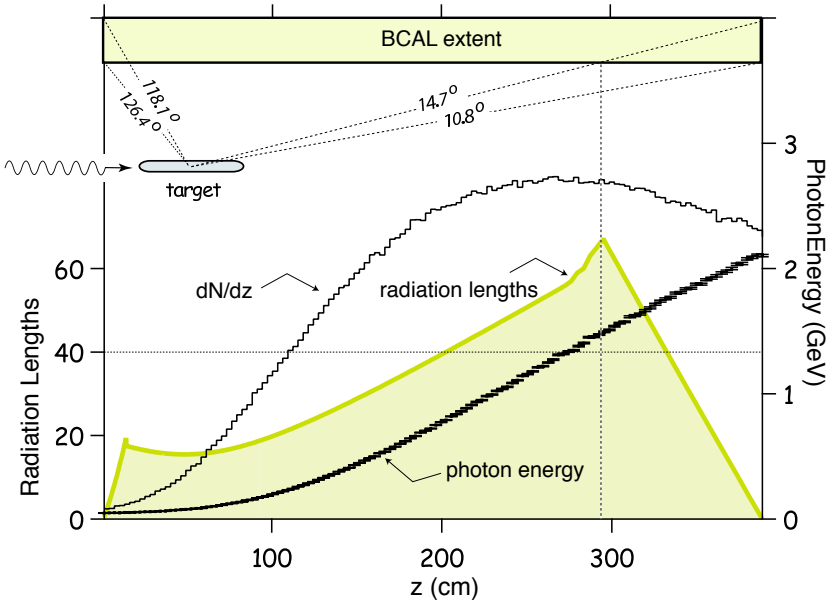

Figure 3.14: The distribution of photons (dN/dz), their energy and integrated path length through the Pb/SciFi matrix as a function of position along the length of the BCAL for one of the GLUEX signature reactions, $\gamma p \to \eta\pi^0 p \to 4\gamma p$, is shown. The target position and angular range subtended by the BCAL are also presented.

traversed by photons incident at various positions along the length of the BCAL is also displayed. The target occupies the region $z = 33 - 63$ cm relative to the upstream edge of the BCAL. Note that there is a narrow ($\sim 1°$) angular range near 11° where the photon trajectory intercepts a small number of radiation lengths of the Pb/SciFi matrix. Photons with angles less than 10°, with respect to the beam direction, will be detected in the FCAL.

3.3.3 Spaghetti Calorimetry

The BCAL design is based on scintillating fibers embedded in a lead matrix, which results in a relatively high–resolution sampling calorimeter. Such materials have been used in calorimeter design and operation for nearly three decades. The ratio of the active scintillator to the passive high-Z material, as well as the diameter of the fibers, can be tuned to enhance resolution, to determine the radiation length, and to achieve uniformity in the electromagnetic (EM) to hadronic response (the e/h ratio).

In general, the energy resolution of an electromagnetic calorimeter is expressed in the form:

$$\frac{\sigma_E}{E} = \frac{a}{\sqrt{E(\text{GeV})}} \oplus b \oplus \frac{c}{E(\text{GeV})}. \tag{3.1}$$

The $a/\sqrt{E}$ term contains the combined effect of sampling fluctuations and photoelectron statistics, with the former dominating the resolution. This is commonly referred to as the stochastic term. The constant term, b, in Eq. 3.1, originates from sources that scale with energy and contribute to uncertainties in the energy reconstruction. These sources can be mechanical imperfections, material defects, segment-to-segment calibration variations, non-uniformity of

response, instability with time and shower leakage. The noise term, c/E, results from noise electronics noise and pileup in high-rate environments. A similar equation governs the timing resolution:

$$\sigma_t = \frac{c}{\sqrt{E(\text{GeV})}} \oplus d. \tag{3.2}$$

In general, the constant term, d, is the result of residual calorimeter mis-calibrations. However, the measured time difference will also be smeared by the finite beam spot size in a test beam when used to determine this quantity.

3.3.4 BCAL Geometry and Parameters

The BCAL is modelled closely after the EmCal calorimeter built for the KLOE experiment at DAΦNE [13–15], which also operated in a solenoidal magnetic field for more than a decade. The KLOE collaboration developed tooling for the production of long-grooved lead sheets, pushed the technology for excellent fibers with long attenuation lengths ($2.3 < \lambda < 3.2\,m$) and built a device with inner radius of $2\,m$ and $4.3\,m$ length [16]. This device utilized $1\,mm$ diameter scintillating fibers, with a fiber to lead to glue ratio of 48 : 42 : 10. The energy and timing resolutions for KLOE [15] are

$$\frac{\sigma_E}{E} = \frac{5.4\%}{\sqrt{E(\text{GeV})}} \oplus 0.7\%, \quad \sigma_t = \frac{56 \text{ ps}}{\sqrt{E(\text{GeV})}} \oplus 133 \text{ ps}.$$

The latter yields a nearly constant $\sigma_t \approx 180\ ps$ for photon energies above 150 MeV, and a diverging timing resolution for $E_\gamma < 75$ MeV. The EmCal parameters and performance served as benchmarks for the BCAL.

A key instrumentation difference is that the EmCal employed conventional PMT readout at each end that was possible due to the lower field and more favorable magnetic field gradient of KLOE compared to GLUEX. The BCAL requires devices that are practically immune to magnetic fields; Silicon Photo–Multipliers (SIPM's) operate reliably in such conditions. Additionally, it is important to point out differences in the GLUEX and KLOE applications of barrel calorimetry. KLOE is a symmetric colliding beam experiment, with the intersection region at the center of its barrel calorimeter. As a result, that calorimeter is illuminated symmetrically and nearly uniformly by photons having 100-200 MeV energies, on average, and with very few photons greater than 400 MeV. On the other hand, GLUEX, is a fixed target experiment, resulting in a highly asymmetric photon distribution: 30% of the photons in the BCAL will have energies considerably higher than 500 MeV. Despite these differences, the KLOE experience provided valuable guidance in the design and construction of the BCAL. The KLOE resolutions are adequate for the GLUEX physics requirements, as indicated by our simulation studies. The extracted resolutions are a direct result of the internal PbSciFi matrix geometry such that similar resolutions should be expected for the BCAL [17].

For GLUEX, the tracking elements inside the magnet's bore require a radius of at least $65\,cm$ in order to perform optimally, leaving about 25 cm of radial thickness for the BCAL. Together with the $4.5\,m$ length of the solenoid these lead to a long, narrow, tube-like design. In this geometry, the readout is logically placed at the ends where space exists and where it can take advantage of the fact that all fibers run parallel to the axis of symmetry of the solenoid and therefore all light piped to the ends of the modules retains its azimuthal and radial information. With rise times of a few ns, good timing can be expected in collecting the light from a shower.

Moreover, because the EM showers spread across the azimuthal boundaries, algorithms for finer positioning of the shower are required. A typical weighted position resolution is $\delta x \approx 5\,mm\,/\sqrt{E}$. For the BCAL design, this would lead to an azimuthal resolution of $\approx$ 8.5 mrad. Using the z position resolution of approximately 4 cm obtained from the time difference leads to a polar angular resolution at 45° of $\approx$ 8 mrad. The time difference from the two ends produces the z coordinate of the hit. Because we will use an array of readout devices on each end (segmented in azimuth and depth), redundant measurements are made of the z coordinate. These measurements of z correspond to different average radii and therefore help to establish the angle of the incoming photon. Finally, the fractional volume of scintillator in the detector naturally makes it efficient for detecting charged hadrons. The mean light collection time of the two readout ends can be used to determine the particle time-of-flight (TOF). TOF coupled with the track length and momentum then yields particle mass, thus contributing to PID information.

The BCAL design is depicted in Fig. 3.15, a zoomed-in view of the matrix is portrayed in Fig. 3.16. The main parameters of the BCAL can be found in Ref. [18] and fabrication was based on the assembly drawings in Ref. [19]. The completed lead-scintillating fiber matrix including the light collection and sensing units at each end is called a module. Fourty eight modules were constructed, plus one spare.

The choice of readout device must bear in mind the considerable magnetic field (2 T) inside the bore and the rapidly varying fringe field at the ends. The option chosen for the readout is based on a large-area application of SiPM's. These devices offer gain and timing resolution comparable to that of a PMT, superior energy resolution, are immune to magnetic fields, and require simple electronic amplification and summing circuits. Each channel will also include low-voltage bias and power for the preamplifiers, a flash ADC, discriminator, TDC and cabling. Forty independent light guides were fastened with epoxy to the two polished ends of the BCAL. A gain-stability, monitoring system is critical and is based in part on small LED's glued directly to each of the light guides. The LED driver system consists of small LED boards driven in four strings of 10 LEDs per side, by a custom-designed controller board. All these are presented in more detail below.

3.3.5 Module Construction

In order to build lead-SciFi modules, our collaboration studied and used the KLOE tooling techniques. Specifically, a "swager" (plastic deformation machine) was borrowed from KLOE and was used as a model to build our own. As a result, several prototypes were built, gradually increasing in dimensions and culminating in two full-sized (l: 400 cm x w: 13 cm x h:[21-24] cm) prototypes, named Prototype 1 and 2. For the production, lead sheets were ordered from the manufacturer[17] at specified widths and Kuraray SCSF-78MJ, double-clad fibers[18] were used.

The modules were built by employing two custom-designed presses that pressed the matrix as it was being stacked with alternating layers of lead sheets and fibers, thereby expelling excess epoxy and allowing the bonded matrix to set. They consisted of a $\sim$4.5 m steel bed, two tilting pistons that raised/lowered a group of 20 pistons to the top surface of the matrix, as well as associated electronics and pneumatics. The fibers were bonded in the lead channels with Bicron-600[19] optical epoxy: the internal matrix geometry is indicated in Fig. 3.16. Visual

[17] Vulcan Lead Inc (www.vulcunlead.com)
[18] Kuraray America Inc., Houston, TX, USA (www.kuraray-am.com)
[19] Saint-Gobain Crystals & Detectors, USA (www.bicron.com)

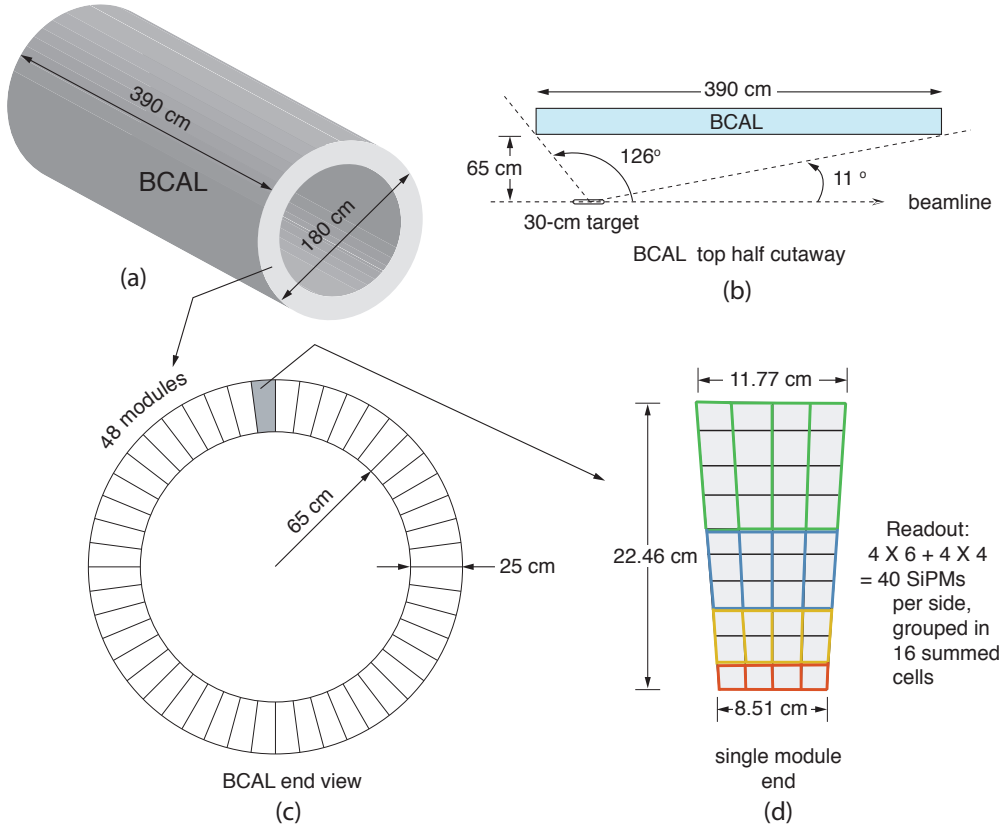

Figure 3.15: Sketch of Barrel Calorimeter readout. (a) A three-dimensional rendering of the BCAL; (b) top-half cutaway (partial side view) of a BCAL module showing is polar angle coverage and location with respect to the GlueX LH_2 target (light guides and readout modules are shown in Fig. 3.17; (c) end view of the BCAL depicting all 48 azimuthal modules and (d) an end view of a single module showing the readout segmentation: four rings (inner to outer) comprised of sums of 1, 2, 3, and 4 readout rows, respectively, and four azimuthal slices (columns), resulting in a total of 16 summed readout zones. More details can be found in the text.

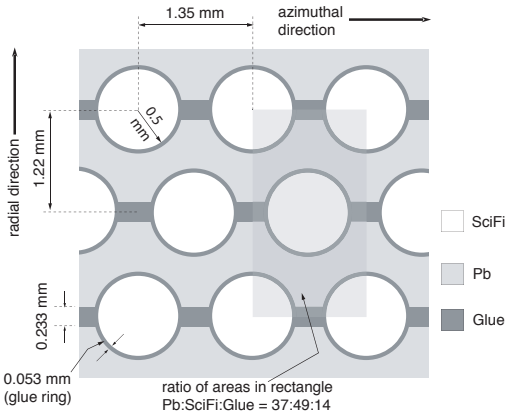

Figure 3.16: Close-up view of the BCAL matrix details.

inspection revealed that only a handful of the approximately 15,350 fibres in each module were damaged during the construction.

A comprehensive report (how-to manual), training video, photos and movies were prepare to simplify the training of personnel and to document the methods employed [20–23]. The final set of construction procedures were recorded in a step-by-step "Procedures Manual" – complete with photos – which details the entire production process [24].

Built modules were shipped for machining to an industrial firm[20]. The process included shaping the modules to their final dimensions within tight tolerances, polishing the two ends and machining features in the aluminum base and top plates.

3.3.6 Light guides

The BCAL light guides connect the output face of the modules to the SiPM light sensors. The geometry of the light guides is azimuthally symmetric, consisting of four identical radial columns per BCAL wedge. Each column consists of ten light guides, which cover an azimuthal angle of 1.875° degrees. Both the input and output faces of the light guides are trapezoidal in shape. The bases of the guide are glued to the face of the BCAL and increase in width toward the outer edge of the wedge. The radial dimension of the bases is 20.57 cm for the inner six guides and 24.64 cm for the outer four. The base of the guide receives the light from the calorimeter and funnels it down to a smaller trapezoid covering the sensitive area of the SiPM sensors, which is 1.27×1.27 cm^2. The length of the light guides is 8 cm. There is a 0.5 mm air gap between the output of the light guide and the 0.45 mm clear epoxy protective coating over the sensitive area of the SiPM. The light guide shapes are shown in Fig. 3.17. The simulated light collection for the ten guides ranged from 0.48-0.75%. [25]

The light guides were fabricated from ultraviolet transmitting (UVT) acrylic at the Universidad Técnica Federico Santa María according to JLab drawings [26–35]. Dimensional tolerances were kept under control to avoid interferences between wedges. The light guides were glued onto the face of the modules at Jefferson Lab using Norland NOA 87 UV adhesive following the procedure documented in Procedure D000000107P003 [36]. Each light guide was covered with a black Tedlar cover to avoid any optical cross talk between the firing cells. Measurements of different materials for the cover showed no significant differences in light collection [37], as might be expected if the collection efficiency is dominated by total internal reflection. Tested LED boards in strings of 10 LEDs were glued onto the face of the light guides during the gluing procedure while there was access. Hardware to attach the readout assembly was mounted to each module and every combination of LED string and high voltage setting was verified to output signals. An overnight run triggering on cosmic rays was taken as a reference for future calibrations. Tracking the gluing procedure and repairs was documented using the JLab Pansophy system [38] .

3.3.7 Silicon Photomultiplier Arrays

The BCAL will reside inside a 2 T superconducting solenoid with the magnetic field – in its readout region — calculated to be 1.5-2 T upstream and ∼0.5 T downstream. We have selected the new technology of silicon photomultiplier arrays (SiPM's), which can operate in fields well beyond this limit. This technology was developed through an extensive R&D effort between

[20] Ross Machine Shop, Ltd. 40 Kress Street, Regina, SK, Canada

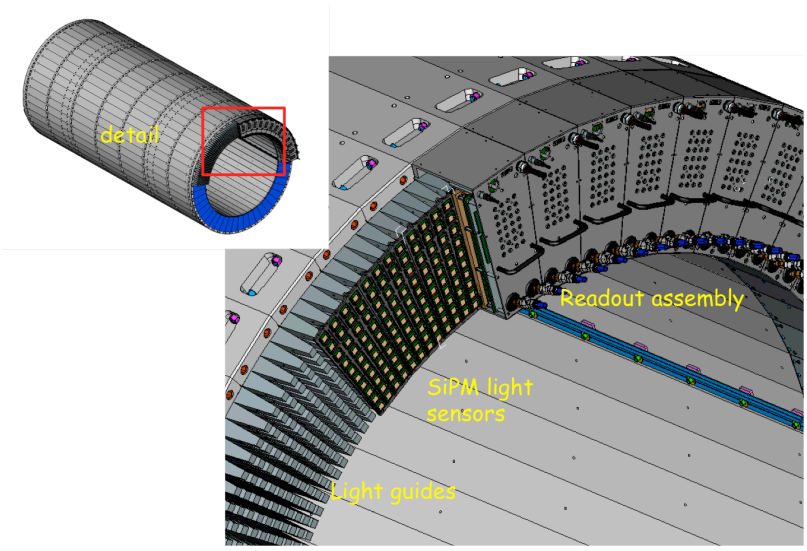

Figure 3.17: Three-dimensional rendition of the light guides mounted at the end of the BCAL as well as the readout assemblies mounted over them and containing the SiPMs and their electronics.

GlueX and SensL[21], a photonics firm from Ireland. This led to the "tiling" of 16 $3 \times 3\, mm^2$ SiPM's into a 4×4 array of cells, having a 1.26 cm^2 area. Such large area units have found broad appeal from subatomic physics to medical applications, with several manufacturers entering the field. Following a competitive bidding process, Hamamatsu[22] was selected to provide the readout devices for the BCAL.

The selected sensors are Hamamatsu S12045 MPPC arrays with a sensitive area of 1.44 cm^2. The basic SiPM unit is a $3 \times 3\, mm^2$ cell with 3600 50 μm micro-pixels, which are joined together on a common substrate and under a common load. The sensor is a 4×4 array of cells with a dynamic range defined by the 57,600 micro-pixels in each array. The single micro-pixel gain is $\sim 10^6$, roughly the same order of magnitude as that of a traditional PMT. While each pixel operates digitally as a binary device, the output signal behaves as an analog detector that is proportional to the incident light intensity.

The SiPM's operate at an operational voltage V_{op} that is 0.9–1.2V above the typical breakdown voltage (V_{br}) of about 71 V at room temperature. The gain is proportional to this over voltage ($V_{over} = V_{op} - V_{br}$). At V_{over}=0.9 V and 23°C, these devices have a typical gain of 0.75×10^6, photon detection efficiency (PDE) of about 21% [39], but a relatively high single-photoelectron dark rate of 16 MHz per array. The relatively low over voltage and the sensitivity

[21] SensL, Blackrock, Cork, Ireland (www.sensl.com)
[22] Hamamatsu Corporation, Bridgewater, NJ 08807, USA (sales.hamamatsu.com/en/home.php)

of the breakdown voltage to temperature imposes considerable requirements on operation. The sensitivity of the breakdown voltage to temperature is nominally 56 mV/°C [40]. The gain, PDE and dark rates all depend on the breakdown voltage and therefore proper operation of the sensors requires careful temperature stabilization.

A total of 3840 SiPM's are needed to instrument the BCAL. The order for the SiPM's was placed based on Specification D000000107S004 [41] and was split between Jefferson Lab (1200 units) and the Universidad Técnica Federico Santa María (USM) (2810 units). The eighty first article samples were checked at Jefferson Lab and verified and in all cases they either achieved or exceeded the design specifications [42,43]. Quality control tests were carried out at Jefferson Lab and USM on each SiPM unit received. Only one unit failed specifications at JLab, and three at USM. All four samples were replaced by Hamamatsu. Regina also conducted selected tests mimicking the experimental conditions although analyzing the data using energy-summing boards (photo peaks not visible) instead of individual readout boards (reading each of the 16 cells of the array individually, thus seeing the photo peaks). The average geometrical mean from the Regina measurements of $(24 \pm 2)\%$ is consistent with measurements at Jefferson Lab $(21 \pm 1)\%$ [42]) and USM $(23 \pm 2)\%$ [**?**]. All measurements produced PDE values $> 19\%$, which was the contract specification and were also consistent to test data provided by Hamamatsu. The characteristics of the arrays measured are shown in Fig. 3.18.

3.3.8 Radiation Damage

It is well known that the performance of silicon detectors degrades after exposure to radiation. We have therefore checked the effect of radiation to the Hamamatsu S12045 MPPC arrays. Only the dark rate seems to be significantly affected, which increases linearly with neutron dose at a rate of about 16 MHz per $10^9 \mathrm{n}_{eq}/\mathrm{cm}^2$ [39,44]. The dark current is essentially unaffected by electromagnetic radiation, tested with 0.67 MeV γ rays from a ^{137}Cs source up to an exposure of 2 krad, which is ten times the dose expected in ten years of operation in HALL D. The calculated neutron dose at the downstream end of the BCAL during high intensity operation, assuming 10^7 live seconds per year and a hydrogen target, is $3 \times 10^8 n_{eq}/cm^2$. The dose at the upstream end is about four times less. Running with a helium target would increase the dose by 50% [45]. Over the course of time, the dark rate at room temperature will exceed our design specification of 100 MHz/array. This increase will be compensated for operating the MPPC's at lower temperature. The dark rate is three times less at 5°C than at 20°C [46], extending the expected useful lifetime of the MPPC's at high intensity to about 7 years. However, initially the sensors will be operated just below room temperature at about 18°C so we can use water in the cooling loops and also avoid any risk of condensation inside the readout assemblies.

3.3.9 Readout Assembly and Granularity

The readout assembly holds all forty MPPC's that collect light from one end of a module, the supporting infrastructure to operate them, and the electronics that produce output signals to feed the flash ADCs and pipeline TDCs. The temperature stabilization is an integral component of the assembly and is addressed using a two-fold approach. First, we have implemented a mechanical cooling system with the goal of maintaining the temperature of the sensors within ±2°C of the operating point. The cooling system is composed of a chiller; the coolant is water during initial operation and later water and 20% propylene glycol for operation at 5°C. The coolant flows through a copper pipe that is glued to a copper cooling plate, which is in thermal

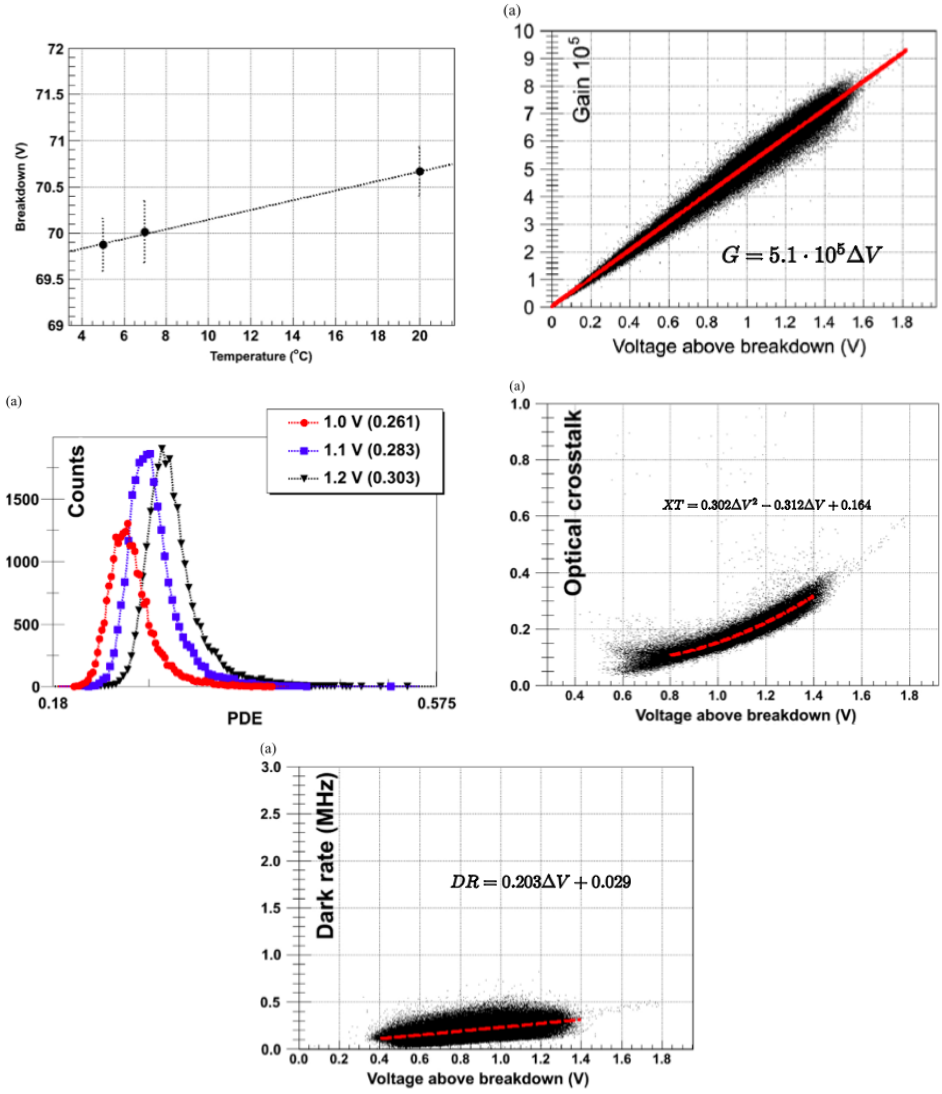

Figure 3.18: Measured characteristics of the production SiPM arrays (Hamamatsu S12045 MPPC's).

contact with the back of the SiPM sensors. Second, a thermistor is incorporated in the sensor bias circuit to compensate for any temperature deviations from the nominal operating point and thereby maintain a stable output under small changes in the environment. The relatively low over voltage results in high sensitivity to the setting and stabilization of the bias voltage. The requirement is to maintain the voltage set point to within 10 mV, which corresponds to a gain variation of less than 1%. The effect of any temperature changes must be kept to less than 1% also.

The layout of the individual MPPC bias and readout is shown in Fig. 3.19. The light guides are arranged in four rows of ten identical columns on the face of the BCAL modules. Each MPPC has its own pre-amplifier but various groups of MPPC's are summed to generate the output signals. The BCAL is divided into four readout rows, within which individual MPPCs

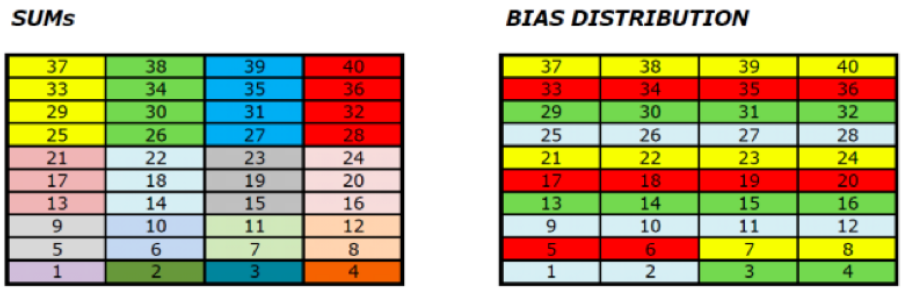

Figure 3.19: *Left panel:* Schematic layout of summed (1:2:3:4) MPPC outputs for the upstream facing downstream. Each number corresponds to a single sensor and colors show the groups that are summed into the readout channels. *Right panel:* Assignment of four bias voltages to groups of ten MPPC's: light blue is bias 1, green is bias 2, red is bias 3 and yellow is bias 4. The summing is radially outward as shown in Fig. 3.15 and the bias channels are assigned along rings of constant radii. The up- and downstream ends are mirror symmetric so that a cell number at the upstream end corresponds to the same number downstream.

are summed column-wise in groups of 1, 2, 3 and 4, respectively. This scheme retains the complete azimuthal segmentation, but results in coarser longitudinal shower segmentation a decision taken based on electronics cost considerations [47]. Thus, forty MPPC's on each end of the BCAL are summed into sixteen groups, which are digitized by 250 MHz Flash ADC's, but only the first twelve sums are discriminated and fed into pipeline TDC's to measure their times. The bias lines deliver power to groups of ten sensors, but the grouping is orthogonal to the readout sums, as shown in the figure. This allows individual MPPC's to produce the sole output of a summed channel by appropriately enabling bias voltages during calibrations.

The temperature compensation circuit for BCAL is a voltage divider with one temperature dependent resistor element (thermistor). The values of the resistances coupled with the value for the V_{Supply} voltage allow the sharing of a single supply voltage among several SiPMs, while still providing a temperature compensated V_{op} value that stabilizes gain. The individual resistor values to tailor the input voltage to different MPPC's were determined based on Hamamatsu datasheet values for the recommended V_{op} (given for 25°C) and adjusted for a presumed operation temperature of 5°C. Operation at a specified temperature and over voltage (V_{over}) requires a formula that takes into account the temperature dependent nature of the voltage divider circuit, and the errors from ideal operation induced by granularity of the trim values. Details are provided in Ref. [48]. The formula has been incorporated into the EPICS control system to set the proper operating parameters for each of the four bias inputs to each side of each module. For this reason, the readout assemblies are not easily interchangeable.

3.3.10 BCAL monitoring

The monitoring system is designed to track the stability of the MPPC output signals between calibrations with particles, about once per day. The system is composed of light emitting diode (LED) light sources, which are distributed one per light guide. They are placed in pockets drilled on the side of the light guide, which are 4 mm in diameter and 2 mm deep and located 3.8 cm from the BCAL module. The monitoring system is presented in more detail in Ref. [49]. Here

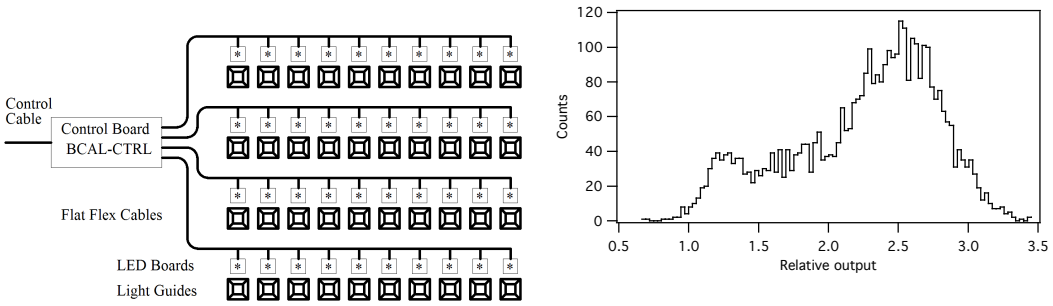

Figure 3.20: *Left panel:* Configuration of the BCAL monitoring system for one side of one module. *Right panel:* Relative output of all ∼4,000 BCAL LEDs driven by their respective boards.

we give a brief overview.

The LEDs[23] come in a standard surface mount package emitting blue light at 471 nm, which is near the peak of the fiber emission spectrum [**?**]. Each LED is attached to a $12 \times 13.5\, mm^2$ PCB board so that it emits light parallel to the PCB, through the near light guide and toward the opposite side of the BCAL module. Light enters the fibers and is transmitted through the module to the sensor at the far end and also reflected from the near end of the module back into the near sensor. With this geometry, the signal in the near sensor exhibits prompt light as well as a delayed reflected pulse from the opposite end of the module. The signal in the far sensor is smoother and reaches a higher peak amplitude.

As mentioned previously, the forty LEDs at each module's end are grouped into four independent groups. The system configuration is shown in Fig. 3.20. Each group is attached to a flex ribbon cable and its 10 LEDs are pulsed simultaneously using a common trigger signal from a control board (BCAL Controller) located on the outer edge of each wedge. Each string is attached to a column of light guides, which is orthogonal to the cabling that provide the bias to the MPPCs. The possibility of noise pickup in a MPPC induced by the BCAL monitoring system was investigated but no such pickup was detected as a result of proximity operation to both LED and controller boards. 3840 production LED mini boards plus 100 spares were tested and divided into groups of similar intensity. The relative light outputs of these LEDs are shown in Fig. 3.20. The variation between the LEDs in a single group of ten is typically less than 1%.

The overall pulsing system is segmented into four quadrants for both the upstream and downstream LEDs. In each quadrant, four independent TTL signals feed the BCAL Controllers of the twelve modules, which can fire the LEDs in a single column simultaneously. The bias and low voltage to the LEDs can also be adjusted for each quadrant independently. EPICS GUIs have been developed that allow pulsing the system at pre-described rates for the purpose of firing the LEDs and triggering the DAQ system. Whenever an LED trigger is enabled, the system also generates a NIM signal, which is used to enable triggers by the DAQ system.

[23] Model SMS1105BWC, Bivar, Inc., CA 92618, USA (www.bivar.com)

3.3.11 Characteristics of the components

Production Fibers

Due to the length of the BCAL, superior quality fibers were required and ordered according to Specification D000000107S001 [50]. Over three quarters of a million, 4-m-long Kuraray double-clad SCSF-78MJ (blue-green) scintillating fibers have been used in the construction of the BCAL. The response and quality of these fibers has been evaluated by employing a 373-nm UV LED to stimulate the fibers along their length and reading out the light using a spectrophotometer and a photodiode in order to extract the spectral response and the effective (bulk) attenuation length, respectively. In addition, diameter uniformity measurements were carried out. Nominally, 0.5-1% of the fibers were tested from each shipment, and the quality assurance results confirmed that the fibers were of high quality and complied with GlueX specifications. The key parameters tested were:

1. dimensional uniformity: outer radius conforming to 1 mm diameter.
2. spectral response: wavelength of maximum emission of the scintillator was specified to be between 450 and 500 nm.
3. bulk (effective) attenuation length: specified to be greater than 300 cm and with $RMS \leq$ 10% over the 100-280 cm source distance range, when measured with a bi-alkali photo-multiplier tube.
4. light output: specified in terms of the number of photoelectrons (N_{pe}) collected at the fiber's end, had to be greater than 4.5 using a bialkali PMT at 200 cm from the source with $RMS \leq 15\%$.

The measurements and conclusions from this extensive Quality Assurance (QA) excercise are summarized herein; detailed interim [51–53] and final reports were produced [54] and detailed summary published in Ref. [55].

In order to assure a uniform matrix during the building, the fibers had to be uniform in diameter and free of defects such as protrusions. To this end, fibers were visually inspected and the fiber diameter was measured at three locations along the length of each sampled fiber (50 cm, 200 cm and 350 cm from one end) using a micrometer caliper, for 883 fibers from Shipments 1-29. The error on each measurement was 0.005 mm. A Gaussian fit to all the data yielded (0.997 ± 0.006) mm. All measurements fell within the specifications: diameter of 1 mm with a $RMS \leq 2\%$.

Spectral Response

Details on the test setup can be found in Refs. [54,56], and, therefore, are recounted only briefly herein. A USB4000 spectrophotometer[24] and the tested SciFi were coupled together in a robust manner. An RLS-UV380 ultra violet LED[25] – having a peak emission wavelength of 373 nm – stimulated the fiber. The LED translated across the length of the fiber and measurements were carried out in near darkness. As an additional precaution against UV damage, UV-absorbing film (TA-81-XSR[26]) was used to cover all overhead fluorescent lights and the desk lamps.

[24] Ocean Optics Inc., Dunedin, FL, USA (www.oceanoptics.com)
[25] Roithner Lasertechnik, Vienna, Austria (www.roithner-laser.com)
[26] Window Film Systems, London, ON, Canada (www.windowfilmsystems.com)

Measured wavelength spectra were fitted using double Moyal functions plus a flat background, with the LED positioned at 10 cm, 30 cm, 100 cm and 300 cm. The Moyal function is of the form:

$$f(x, a, \mu, \sigma) = a \cdot \exp\left(-\frac{1}{2}\left(\frac{(x-\mu)}{\sigma} + e^{-(x-\mu)/\sigma}\right)\right) \tag{3.3}$$

These spectra are overlayed in Figure 3.21 together with the corresponding Kuraray spectra of a fiber from Lot JS072 [57]. The peak intensity and the integrated spectral strength scale as a function of distance from the light source in a similar manner for both sets of measurements. Minor differences in the spectral shapes between our measurements and those from Kuraray are perhaps due to the measurement apparatus and/or specific choice of fibers tested.

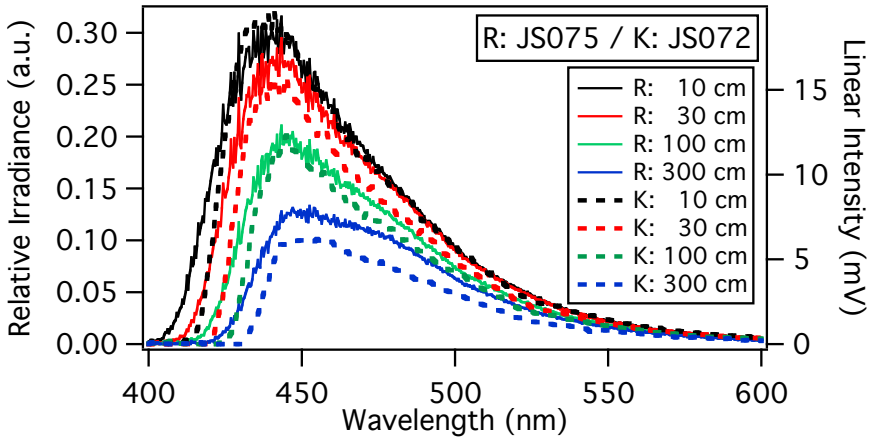

Figure 3.21: Wavelength spectra, measured at Regina ('R' label) at source distances of 10 cm, 30 cm, 100 cm and 300 cm for a JS075-lot fiber are shown as solid lines, with the corresponding Kuraray spectra [57] ('K' label) for a JS072-lot fiber displayed as dotted curves. The former are relative irradiance measurements and the latter are in units of linear intensity.

Attenuation length

Considering the large number of fibers to be tested, an expedient method was developed in order to extract the attenuation length based on a Hamamatsu calibrated S2281 photodiode [54]. It should be mentioned that the spectral sensitivity of this device is relatively flat in the range of the fibre emission spectrum, and as such, the extracted attenuation length reflects the fibre performance exclusively. Each tested fibre was positioned horizontally in a 420-cm-long, 1-mm-deep channel machined in a black polyethylene board that had an attached length scale. The near end of the fibre was polished using a Fibre Fin 4 diamond polisher[27] before being connected to the photodiode using Dow Corning[28] optical grease, and the device was read out using a Keithley 6485 picoammeter[29]. The far fiber end was initially blackened using black

[27] FibreFin Inc., 201 Beaver Street, Yorkville, IL, USA (www.fiberfin.com)
[28] Dow Corning Corporation, Midland, 48686 MI, USA (www.dowcorning.com)
[29] Keithley Instruments, Inc., Cleveland, 44139 OH, USA (www.keitlhey.com)

mat enamel paint (used for scale model painting) and later on was left as un-blackened, factory rough-cut. An RLS-UV380 UV LED stimulated the fibre. The LED could be positioned on the lab bench guided by a holder on the polyethylene board and translated across the length of the fibre.

The data from each fiber were fit using a single exponential fit of the form $I = I_0 e^{-x/\lambda}$ in the 100-280 cm source distance range. The results conform to contract specifications, with λ greater than 300 cm in all cases. The agreement is quite good in the comparison between Regina and Kuraray measurements, and similar features are present in both data sets. Since the measuring setups are different, the features are clearly a result of the fiber properties, which depend primarily on the secondary dye content. Finally, both Kuraray's and Regina cumulative results had a standard deviation less than 10%, and therefore met the contractual specifications.

A single exponential fit to the fiber data is possible only over a limited range of source distance, as was carried out above. When the entire range is examined, and in particular source distances below 100 cm, a double exponential fit is required owing to the capture of short-wavelength light (blue region) which otherwise becomes absorbed leaving only the longer wavelengths. The following function was used:

$$I = I_0 \left(e^{-x/\lambda_L} + \alpha \cdot e^{-x/\lambda_S} \right) \tag{3.4}$$

where λ_L and λ_S are the long and short attenuation lengths, respectively, I_0 is the readout current in units of μA and α represents the relative strength between the two components. Most events were clustered in a peak centered around $\alpha = 0.3$, and average values of $\lambda_L = (482 \pm 5)$ cm and $\lambda_S = (74 \pm 1)$ cm were extracted.

The shipment results are shown in Figure 3.22. The error bars reflect the standard deviation of the distribution from individual fiber measurements. Linear fits show the extracted averages. It is noted that a correction to the attenuation length due to the different treatment of fibers for Shipments 1-3 was not applied (a 3% increase), but this does not change any of the conclusions that all measured parameters were found to be comfortably within contract specifications, and overall this product was of high quality.

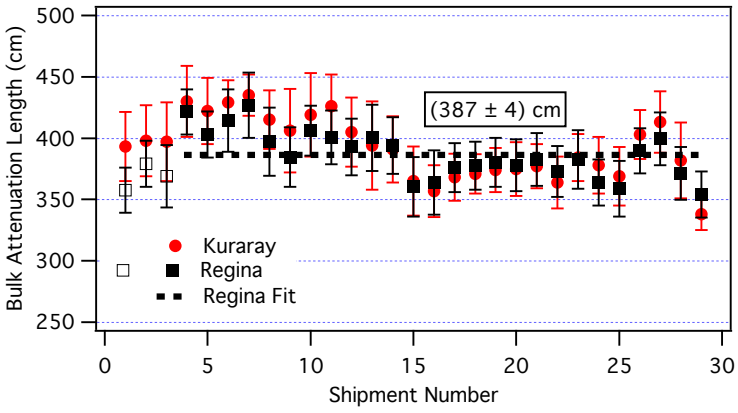

Figure 3.22: The bulk attenuation length, from a single exponential fit between 100-280 cm is shown as a function of shipment number for Regina and Kuraray measurements.

Number of photoelectrons

Details on the N_{pe} measurements can be found in our final report [54], and, therefore, are only summarized herein. Both ends of the fiber were polished and one was blackened. The fiber was then inserted in a dedicated measuring station contained in a 4.5-m-long dark box. A Hamamatsu R329-02 calibrated photomultiplier with a standard progressive voltage divider was used to measure the light from the fiber. A small dab of optical grease[30] was applied to the non-blackened polished end of the fiber before coupling it to the PMT using a piece of machined acrylic as a fiber guide.

The fiber was stimulated using a ^{90}Sr radioactive source, which was placed within a custom-designed lead collimator, the latter positioned over the center point of the fiber, approximately 200 cm from the PMT's end. The collimator consisted of a 4×4 cm^2 Pb block, having an 8 mm diameter partial bore to house the source. Located below the source was a slit having dimensions $13(h) \times 0.5(w) \times 8(l)\,\text{mm}^3$ and a 1×1 mm^2 groove along the bottom of the collimator for accurate placement and illumination of the tested fiber, the groove being parallel to the 8-mm-slit side. The collimator included a lid, since it was determined that a small amount of "backsplash" activity resulted from source electrons striking the lid of the dark box. A ∼9 cm-long scintillator counter was coupled to a Burle 8575 PMT (at 1700 V) and was placed directly below the fiber, thus sandwiching the fiber between it and the source/collimator above.

The results of the fit extractions for the N_{pe} — averaged for each lot and plotted against the lot number with the error bar being the RMS of those distributions — are shown in Figure 3.23. Only fibers from Lots 96–707 (Shipments 4–29) were analyzed; Lots 1–95 (Shipments 1–3) were excluded from this comparison due to different handling of the fiber ends. Clearly, there is lot-to-lot variation apparent in the number of photoelectrons, as was also manifest in the attenuation length measurements [55]. Kuraray observed a similar behaviour in measurements of their own, with the most likely candidate for the difference being small impurities in the secondary dye in the fiber's chemistry, which cannot be controlled in the manufacturing process[31].

3.3.12 Photon Beam Test: Energy and Timing Resolution and Number of Photoelectrons

A photon beam test of Prototype-1 module was carried out in Hall B in 2006 with the objective of measuring the energy and timing resolutions of the module as well as the generated number of photoelectrons [58,59]. This prototype served to establish of baseline for the performance of the final BCAL, but not all its components nor shape were retained for production. The prototype had a rectangular cross section instead of the trapezoidal shape of the final detector modules. It was constructed using Pol.Hi.Tech.0044 fibers[32], while the fibers selected for production were higher quality Kuraray SCSF-78MJ fibers. The prototype readout was divided into 18 readout segments, each with dimensions 3.81×3.81 cm^2 and readout by PMTs, while the production readout has 16 readout segments consisting of MPPC sums. Low current (1 nA) data were collected over the tagged photon energy range of 150 to 650 MeV at multiple positions and angles along the module. The photon beam was collimated with a 2.6 mm collimator, resulting in a beam spot of virtually uniform density with a diameter of 1.9 cm on the BCAL module. The extracted energy resolution at normal incidence and at the center of the module was

[30] EJ-550 Silicone Optical Grease, ELJEN Technology, (www.eljentechnology.com/)
[31] Kuraray, private communication (2011)
[32] Pol.Hi.Tech. S.R.L., Carsoli, Italy.

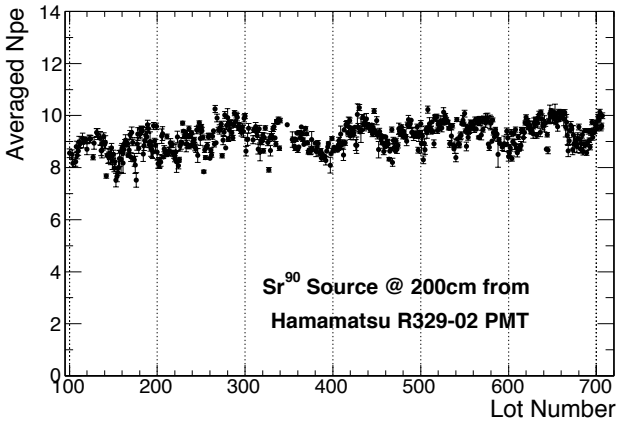

Figure 3.23: The N_{pe} results are averaged by lot number, and their average is graphed against the lot number. The results conform to contract specifications by being greater than 4.5 using a bialkali PMT at 200 cm from the source with $RMS \leq 15\%$.

$\sigma_E/E = 5.4\%/\sqrt{E(\text{GeV})} \oplus 2.3\%$, i.e. the fits were consistent with $c = 0$ of Eq. 3.1. Small variations in the fits produced relatively large variations in the floor term ($2.3 \pm 1\%$) but little variation in the stochastic term ($5.4 \pm 0.1\%$). The energy resolution plotted versus the mean tagger energy for the respective bin is shown in Figure 3.24 and demonstrate the design will meet our requirements.

We also studied how the resolution changed for showers produced by photons incident at forward angles. The extracted energy resolution shows the degradation as the incident photon angle decreases. Specifically, the stochastic term a in Eq. 3.1 increases from 5.4% at 90° ($z = 0\ cm$[33], center of module) to over 7% at 15° ($z = 100\ cm$). The change in the parameter a, shown in Figure 3.24, is expected since fluctuations from intrinsic properties of the interaction mechanisms increase with the number of particles created as the shower develops. As the angle decreases, the particles transverse more of the radiator mass resulting in more interactions and of course increased fluctuations [17]. This expectation has been corroborated with Monte Carlo simulations [60].

The time difference between opposite ends of the BCAL will provide position information for neutral particles, which is needed to reconstruct their four-momentum. The position resolution is related to the time difference resolution by the effective speed of light within the calorimeter. Thus, by using measurements of the effective speed of light in the calorimeter ($v_{\text{eff}} = 17 \pm 0.4$ cm/ns from a previous beam test at TRIUMF [61]), the position resolution of the calorimeter can be easily extracted. The double-ended readout of the BCAL allowed for time difference measurements to be made. The timing for an event was found by summing the TDC values of all the segments in an event cluster, weighted by their energy. The floor term from the fits was equal to the finite width of the beam, as expected. This implies that the intrinsic time resolution of the BCAL is consistent with zero for the constant term, and this why we quote the timing without a floor term below. The time difference resolution, after subtracting the beam

[33]The coordinate system for the beam test, in contrast to the GLUEX global coordinate system, has the coordinate z along the length of the module with the origin at the center of the module.

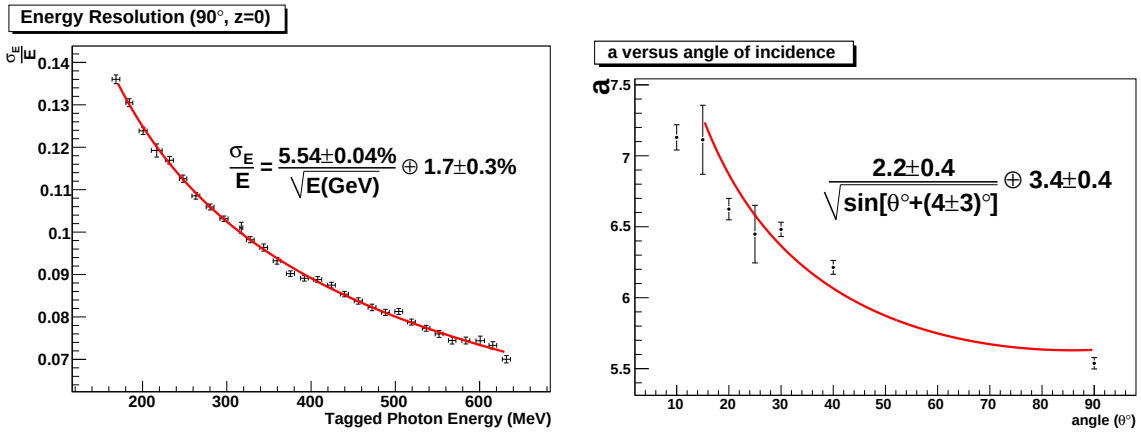

Figure 3.24: Results of the photon beam test. Left: Energy resolution at normal incidence (θ=90°) as a function of tagged photon energy. Right: Resolution parameter a (Eq. 3.1) versus angle of incidence. As the angle decreases the energy term degrades, which is expected because the energy leakage from the sides and also from backsplash out of the front face of the module, increases.

width from the constant term, was found to be

$$\sigma_{\Delta T/2} = \frac{70 \text{ ps}}{\sqrt{E(\text{GeV})}}. \tag{3.5}$$

The position resolution can be computed as $\sigma_z = \sigma_{\Delta T/2} \cdot v_{\text{eff}}$, which gives $\sigma_z = 1.1$ cm for a 1 GeV photon.

The number of photoelectrons per end of the prototype BCAL module, N_{pe}, was estimated at $z = 0$ cm and $\theta = 90°$. The distribution in the ratio, R, of the North to the South readout sums, for each of ten bins in beam energy, E_j, from 150 MeV to 650 MeV, was expressed as

$$R(E_j) = \frac{\sum_{i=1}^{18} E_{\text{N},i;j}}{\sum_{i=1}^{18} E_{\text{S},i;j}}. \tag{3.6}$$

Using this ratio results in the suppression of shower fluctuations that dominate the statistical variance of the individual sums for each readout end. Under the assumption that each of the amplitude spectra has a Poisson-type shape, the ratio spectra were fitted to the function:

$$f(r) \sim \int P(x, N_{pe} \cdot \sqrt{R}) \cdot \frac{1}{r} P\left(\frac{x}{r}, \frac{N_{pe}}{\sqrt{R}}\right) \left[\frac{x}{r} dx\right], \tag{3.7}$$

where r is the event-by-event North/South amplitude ratio, R is an average North/South amplitude ratio, N_{pe} is the average number of photoelectrons, and P is a Poisson-type probability. The resulting photoelectron yield per end was plotted as a function of beam energy and fit to a linear function, holding the y-intercept fixed at zero. This resulted in $N_{pe} = 662 \pm 1$ photoelectrons per end at 1 GeV. In comparison, KLOE reported $N_{pe} \sim 700$ per end at 1 GeV.

3.3.13 Simulation

Shower Profile and Energy Resolution

Details of the response of the full BCAL detector to photons has been simulated using a stand-alone Monte Carlo program that incorporated fine details of the geometry that are not included in the standard Hall D Monte Carlo HDGeant [62]. This allows the description of the shower development in fine steps as well as computation of the sampling fraction, which are not treated accurately in HDGeant. We conducted a series of simulations using GEANT3 [60], without the inclusion of the BCAL magnetic field. However, a description of the geometry of the fibers inside the matrix was included as it is important to determine the correct sampling fraction. Individual fiber and epoxy volumes were programmed into the Monte Carlo with the appropriate Pb:SciFi:Glue ratios and material properties resulting in the geometry shown in Fig. 3.16. The micro geometry of the fiber matrix was encoded in two different ways. In the first, the glue boxes were approximated by trapezoids between the fibers and in the second, strips of glue were placed "inside" the lead with the fiber volumes on "top". The first is termed *traps* and the second *strips*. Since these yielded consistent results only the latter were considered further.

We first fit the shower development to the standard parameterization [63]. If the depth of the shower in the material, expressed in radiation length units, is $t = x/X_0$ and the energy of the incident particle is E_0 then

$$\frac{dE}{dt} = E_0\, b\, \frac{(bt)^{a-1}\, e^{-bt}}{\Gamma(a)} \tag{3.8}$$

describes the evolution of the electromagnetic cascade in the material and, therefore, the shape of the longitudinal shower profile in the lead-fiber-glue matrix. The parameters a and b depend on the nature of the incident particle and the type of the absorbing material. The depth in the material, where the shower maximum occurs, depends on the incident particle's energy E_0 and the critical energy E_c. This parametrized longitudinal development of electromagnetic shower describes the shower reasonably well when the incident photon energy is larger than 1 GeV [64].

Simulations were run from normal incidence down to the minimum acceptance angle of the BCAL. The longitudinal shower profile is shown in the left panel of Figure 3.25 for three different angles of the incident photon with respect to the beam direction. Note that the abrupt termination of a curve corresponds to the end of the matrix due to the exhausted number of radiation lengths. The discrete simulations have been fitted with Equation 3.8. The simulated profiles exhibit the characteristic shower profile shape and expected evolution with increasing energy. At 14° the low energy particles deposit almost all of their energy in the first segment of the module. This explains why the fitted function does not describe the shower development as well as it does for 45° or 90°.

The simulated energy resolution is graphed in the right panel of Figure 3.25 and is in agreement with past simulations [65]. The energy resolution reaches its best value at angles 45° and larger as a result of the improved ability of the module to contain the electromagnetic shower at those angles. At 14° the situation is quite different. The resolution is worse, which is a manifestation of the increased shower leakage from the front of the module (albedo). The shower path at 14° is long enough to eliminate leakage from the back of the module.

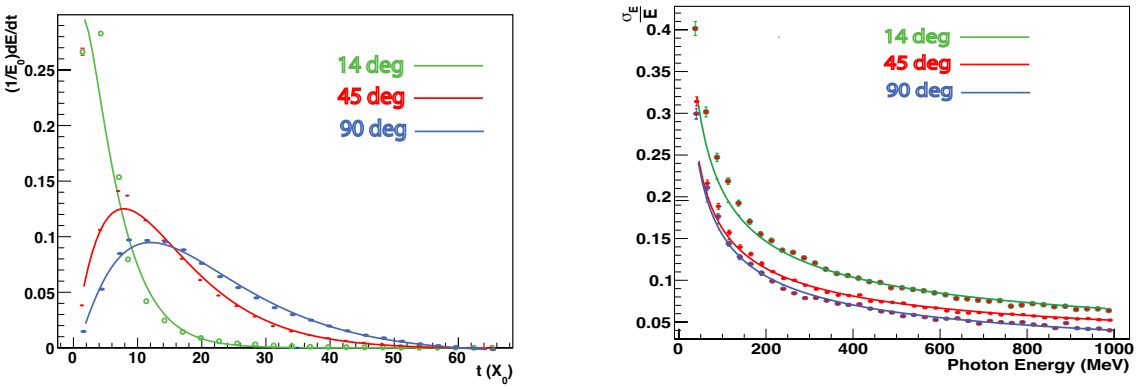

Figure 3.25: *Left panel:* Longitudinal shower profile for 200 MeV simulated photons impinging at 14°, 45° and 90°. The data points correspond to the Monte Carlo results and are fitted with Equation 3.8 represented by the lines. *Right panel:* Energy resolution as a function of incident photon energy for photons impinging at 14°, 45° and 90°. The points are simulated data whereas the lines represent fits to Equation 3.1. The extracted fit coefficients for the energy and floor term (a, b) were $(6.56 \pm 0.02,\ 0 \pm 0.2)\%$, $(4.98 \pm 0.02,\ 0 \pm 0.2)\%$, and $(5.01 \pm 0.03,\ 0.5 \pm 0.6)\%$, for the three angles respectively.

Sampling Fraction and Leakage

The sampling fraction – the fraction of energy deposited in the SciFi's – can be expressed as a ratio with respect to either the total energy deposited in the BCAL module (f) or the incident photon energy (f_γ), with $f_\gamma < f$ since $E_{mod} < E_\gamma$ owing to energy leakage outside the calorimeter volume. These quantities are difficult to measure in an experiment but fairly simple to simulate. Simulations indicate that f_γ decreases as a function of photon energy due to leakage, with the loss being approximately constant above 200 MeV. Clearly, f depends only on the energy deposited in the matrix itself and is independent of the incident photon energy or overall geometry of the module. Our most recent sampling fraction simulations are in general agreement with earlier ones, although the magnitude is less: 9.5% [60] instead of 11.5% in [64, 66]. This is expected due to the refining the SciFi volume to include the insensitive[34] two layers of cladding. The sampling fluctuations, σ_f/f, are the dominant contributor to the energy resolution, at about $4.5\%/\sqrt{E(\mathrm{GeV})}$. Subtracting the simulated sampling fluctuation contributions from the measured energy resolution yields photoelectron statistics contribution to the energy resolution of about $3.1\%/\sqrt{E(\mathrm{GeV})}$ [66]. This is similar to the estimated value of $\sim 2.7\%/\sqrt{E(\mathrm{GeV})}$ from a KLOE beam test [67].

The percent energy leakage out the calorimeter volume is shown in Figure 3.26. The different symbols correspond to energy leaking out from different faces of the module. Front and back refers to the inner and outer faces of the module, respectively, with respect to the radial direction. Leakage from the ends refers to the energy leaking out from the faces of the module along the direction of the beam, where photo sensors will be placed. Leakage from the sides refers to the faces of the module that will be in contact with it's nearest neighbor modules.

[34] Insensitive in this context has the meaning of not contributing to the energy deposited in the fibers.

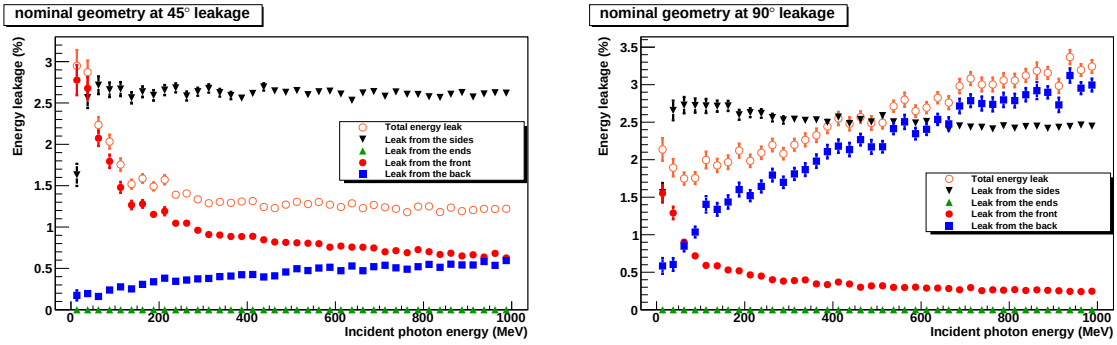

Figure 3.26: Simulated energy leakage (in percent) versus incident photon energy. Energy leakage from the sides is plotted but not added to the total energy leak curve. The leakage out the ends is consistent with zero in all cases except at 12°.

As the latter will be recovered in adjacent modules during the experiment, it was not included in the leakage sum. Indeed, total energy leakage refers to the sum of all energy leaking out the module from front, back and ends. For incident photon angles of 90°, irrecoverable energy leakage occurs mostly from the back of the module and it increases monotonically, following the evolution of t_{max}. It is interesting to note that the amount of energy leaking out from the sides is of similar magnitude as the energy leaking from the back, although the former will be recoverable in the experiment. There is little energy leaking out the front face of the module (albedo) at 90°, but it increases with decreasing angle and dominates the leakage at small angles (12°-14°). The fraction also tends to be larger at lower energies. Low energy particles have increased probability of interaction with only a few layers of lead before the secondary particles drop below the energy threshold for generation of secondaries. Furthermore, there is increased probability of low energy particles to back scatter and end up leaving the module out the front.

Photon-Neutron Separation

Dedicated simulations were carried out contrasting the energy deposition and patterns of photons to neutrons [68]. The aim was to separate photon-caused and neutron-caused showers of the same energy deposited in BCAL fibers. The kinetic energy of selected neutrons (of about $1200 MeV$) was significantly larger than the energy of correspondent photons [69]. A suppression of neutrons by a factor of about 2.5 is achievable without reducing the photon efficiency. The difference in the patterns between the two species is evident in Fig. 3.27. Finally, for each photon- or neutron-induced shower event, the probability was formed that this event came from the photon. The efficiencies in these probability for photon- and neutron-induced showers were simulated as a function of threshold on the photon probabilities and gave good photon ID with suppression of neutrons up to a factor of 4. It should be noted that the higher neutron energy (viz., the more difficult the use of TOF), the better the proposed method works.

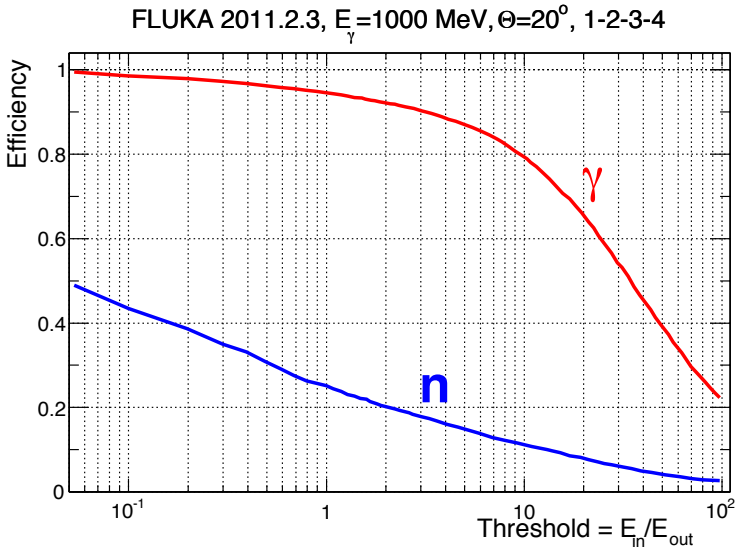

Figure 3.27: The efficiency of photon and neutron detection is plotted versus threshold.

3.4 Forward Calorimeter

3.4.1 FCAL Summary [35]

The main parameters and properties of the FCAL are given in Tables 3.9 and 3.10. The assembly drawing for the FCAL module is D000000106-1000.

Table 3.9: FCAL properties.

Property	Value
Lead Glass F8-00 block dimensions	$4 \times 4 \times 45$ cm^3
Lead Glass density	3.61 g/cm^3
Lead Glass radiation length	3.1 cm
Lead Glass index of refraction	1.62
Radius of the array (59 blocks/2)	$\sim$ 118 cm
Beam hole 3×3 blocks	12×12 cm^2 square
Photomultiplier tube operating voltage	1300-1900 V
Magnetic shielding	1026 steel, 3 mm thickness ave. over square
Magnetic shielding	0.36 mm AD-MU-80 μ-metal
Dark room enclosure	5 (deep) $\times$ 9 (wide) $\times$ 11 (high) ft^3
Energy resolution σ_E/E	$5.6\%/\sqrt{E} \oplus 3.5\%$
Time resolution σ_t	$\sim$0.4 ns for 100 mV
Position resolution	6.4 mm $/\sqrt{E}$

Table 3.10: FCAL channel counts.

Description	Type	Quantity
Lead glass blocks	Lead glass F8-00	2800
Photomultiplier tubes	12-stage FEU 84-3	2800
Voltage dividers	Custom IU Cockcroft-Walton (C-W) bases	2800
Flash ADCs	JLab fADC250-MHz, 16 ch	176
Monitoring Plexiglas pane	UVT PMMA, $\approx 1.5 \times 1.5$ m^2, 1.3 cm thick	4
Monitoring violet LED	Satistronics SS-1206-UV, 10 per quadrant	4×10
Monitoring blue LED	Kingbright KPTD-3216QBC-D, 10 per quadrant	4×10
Monitoring green LED	Kingbright KPTD-3216MGC , 20 per quadrant	8×10
Monitoring controllers	Custom. One per quadrant, serves 40 LEDs	4
CAN-bus for C-W controls	ribbon cables (100 C-W bases per cable)	28
	bridge modules (4 ribbon cables per module)	7

[35] *SVN revision ID:* tdr_summary_fcal.tex 13854 2014-06-12 04:42:15Z gen

3.4.2 Forward calorimeter design

The forward calorimeter is designed to detect photons in the forward region that typically result from the decays of mesons such as π^0 and η. It is a lead glass calorimeter: electromagnetic showers in the lead glass produce Cherenkov light, which is then measured by a photomultiplier tube. The amount of Cherenkov light detected in any individual block scales approximately linearly with the energy deposited in that block. A typical photon shower spreads over multiple blocks. An offline reconstruction algorithm is utilized to group neighboring blocks together and measure the energy and impact position of the photon.

Performance characteristics

The FCAL is expected to measure the energy, position, and arrival time of photons at the detector. The energy and position are obviously useful for reconstructing the four-momenta of photons. The timing information will be used to discriminate signal events of interest from other out-of-time electromagnetic backgrounds.

The nominal design parameter for shower energy energy resolution is $5.6\%/\sqrt{E\ [\mathrm{GeV}]} + 3.6\%$. The leading (statistical) term is obtained by attempting to extrapolate from the performance of the RadPhi calorimeter, which used the same glass and PMTs. The extrapolation studied the contribution of the photostatistical fluctuations to the resolution and took into account the improvements in efficiency for collecting Cherenkov photons made in the optical design for GlueX (discussed below). The 3.6% is a systematic calibration term and is typical of previous detectors of the same type.

Based on previous experience with the E852 and RadPhi calorimeters, both of which utilized the same lead glass and PMTs, we anticipate the position resolution to be $6.4\ \mathrm{mm}/\sqrt{E\ [\mathrm{GeV}]}$. The distance from the center of the target to the upstream face of the FCAL is 560 cm. This results in an angular resolution of order 1 mrad for a 1 GeV photon in the FCAL.

The use of flash ADCs to readout the calorimeter gives an opportunity to make precision measurements of the arrival time of PMT pulses. A signal processing algorithm in the firmware of the flash ADC interpolates samples on the leading edge of the pulse and measures the time at which the pulse crosses one-half of its maximum height. Using a pulsed LED the resolution of this measurement is 600 ps for 100 mV pulses and 240 ps for 500 mV PMT pulses [70]. These timing resolution are at the single block level; for photons, a weighted average over all blocks in the shower can be constructed.

In order to validate the final design, a 5×5 array was constructed using the production components. The array was placed under the Hall B photon tagging array (at Jefferson Lab). The beam for the study was therefore the recoil electron arising from the generation of the photon beam in the Hall B radiator. The strong position versus momentum correlation from the tagging dipole magnet was utilized to select approximately monoenergetic electrons for study. The energy resolution was measured for 110 MeV and 260 MeV electrons, near the low end of the operating range, and found meet design specifications. The timing resolution was determined be 400 ps for 100 mV PMT pulses, exceeding earlier expectations. There was no mechanism for measuring position resolution in this test. Details of the beam test are provided in Ref. [71].

Detector geometry

The forward calorimeter is a planar detector that consists of 2800 lead glass modules stacked in an approximately circular array. The size of the array is such that photons originating from the center of the target but just missing the active downstream end of the barrel calorimeter (BCAL) will be detected by the FCAL. In practice the BCAL light guides and associated readout electronics encroach into this space which will make the ultimate useful acceptance of the FCAL somewhat smaller.

The center of the FCAL contains a square opening that is the size of 3×3 block array (approximately 12 cm square). The opening is filled with a square beam pipe with four walls made from 1/2" stainless steel that was precision-ground for flatness. Steel was chosen because MC simulations showed that the high density tended to shield the lead glass blocks nearest the beam line from low energy background.

The stacking pattern for the surrounding blocks is generated by assuming a 4 cm $\times$ 4 cm block size and placing a block in every location in a rectangular array in which the center of the block would be less than 1.2 m from the center the of the beam opening. This algorithm generates a roughly circular array with exactly 2800 blocks. The longest rows and columns contain 28 blocks on either side of the beam opening.

3.4.3 Forward calorimeter components

In this section we review the detailed technical design of a single lead glass module, 2800 of which make up the entire detector.

Lead glass

The lead glass is reused from the E852 and RadPhi experiments. It was produced in Russia and is called type F8-00. Its chemical composition is 45% PbO, 42.8% SiO_2, 10.4% K_2O and 1.8% Na_2O. This glass has an index of refraction of 1.62, a density of 3.6 gm/cm^3, a radiation length of 3.1 cm and a nuclear collision length of 22.5 cm. Each block has dimensions of $4 \times 4 \times 45$ cm. The blocks were machined to a precision of about 25 microns in transverse dimensions and flatness so stacking the array does not result in gaps.

It is known that lead glass develops color centers and darkens in response to large doses of radiation. Radiation damage of the glass was observed in the RADPHI experiment, especially for those modules nearest the beam line. The radiation damage affects light transmission in the blue part of the spectrum (see Fig. 3.28). As part of the glass assessment process, each block for use in GlueX was checked for damage by examining the light transmission at 410 nm as a function of distance down the bar. Those blocks that were deemed to have radiation damage were then baked in an oven for several hours at 260 °C to cure the damage. After heat treating the bars were indistinguishable from undamaged bars.

In GlueX it is expected that some blocks near the beamline will incur radiation damage throughout the life of the detector. The blocks nearest the center of the detector are expected to receive local doses of radiation at the upstream ends of the block of about 10 kRad per 10^7 s (about 115 days) of running at a rate of 10^8 γ/s on target. After 3×10^7 s of running at a rate of 10^8 γ/s it is expected that that the energy resolution for blocks at a radius less than 24 cm will be degraded by about 10%-20% relative to undamaged glass. Details estimates can be found in Ref. [**?**]. Replacement of the inner portion of the array with radiation hard

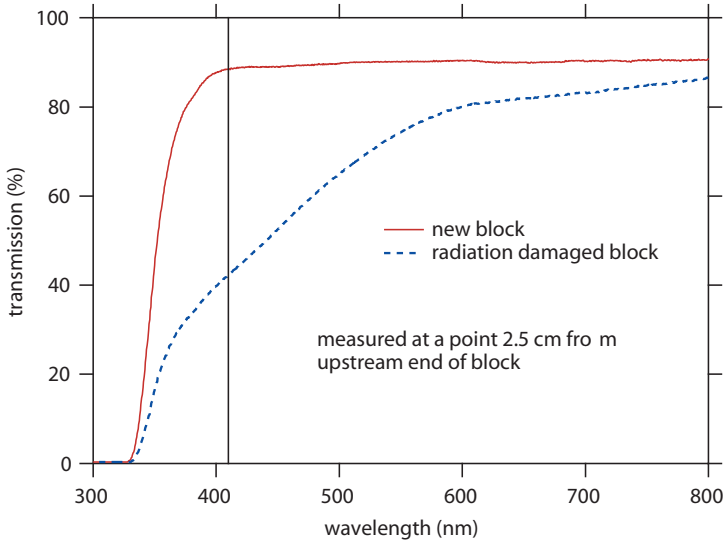

Figure 3.28: Transmission as a function of wavelength for radiation-damaged lead glass and undamaged glass. At about 410 nm the undamaged glass reaches a transmission plateau.

glass was considered. Using radiation hard glass from the outset would have resulted in a 20% worse resolution (relative to F8-00), but would have had the advantage that the resolution was constant with time. At the time of construction the cost of radiation hard glass machined to the specifications of the existing glass blocks was about $2k per block and about 100-150 blocks would have been needed. The monitoring system (discussed below) provides the capability to monitor optical transmission at various wavelengths. This system should provide indication of radiation damage, poor optical transmission at low wavelengths, which can be monitored. If the damage is severe, corrective action such at UV curing *in situ* may be considered.

Optical design

In order to maximize resolution of the calorimeter, one needs an efficient optical connection from the lead glass bar to the PMT. This problem is complicated by the fringe field from the GlueX solenoid in the region of the calorimeter, which is expected to be on the order of 200 Gauss. This requires soft iron shielding of a few of millimeter thickness around the PMT in addition to μ-Metal shielding. This shielding needs to extend beyond the photo-cathode; therefore, the PMT must be coupled to the lead glass block via a light guide.

In developing a design for the light guide, it is important to consider the unique angular distribution of Cherenkov photons as they strike the back of the block (shown in Figure 3.29). Increasing the index of refraction of the interface between the glass block and PMT reduces total internal reflection that traps light inside of the block and increases light collection efficiency. The choice of the best geometric form for the light guide is based on Monte Carlo simulations [**?**] and a cost vs. performance optimization. A suitable, easy-to-machine choice of material is UV transparent Plexiglas. Using a MC simulation based on a Geant4 modeling of the surface properties of the lead glass block, the light guide geometry and the optical coupling between the two and the PMT was studied. It was shown that using a simple cylindrical form was nearly as effective as more complicated Winston cone designs [**?**]. This is predominantly due to

Figure 3.29: Simulated distribution of incident angle for Cherenkov photons produced by an incident 1 GeV photon. The critical angle for total internal reflection for a lead glass and air interface is shown; photons above the dashed line cannot escape the block.

the fact that the majority of the efficiency gains come in eliminating total internal reflection at the back face of the block. Even though the PMT only covers roughly 30% of the area of the back of the block focusing geometries proved not to be effective for the (divergent) Cherenkov photon angular distribution. The light guides will be cemented onto the PMT window. The joint between light guide and lead glass bar is made with a flexible, clear optical coupling material[36]. Simulations indicate that eliminating the air gap between the block and the light guide increases the photon yield by a factor of 2.5.

Since Cherenkov photons, on average, tend to have a relatively high incident angle distribution, a variety of reflective coatings were considered to improve the efficiency of the light guide. Our bench test setup utilized fiber optic connections to inject blue light from an LED into a test lead glass bar at a variety of angles. This allowed us to effectively probe the light guide efficiency and compare with the same GEANT model of the setup discussed above. We tested cylindrical light guides of varying length with three types of surface treatments: (1) no coating or wrapping, (2) a vapor deposited aluminum coating, and (3) a loose aluminized mylar wrapping. In general we found that loose aluminized mylar wrappings, were most effective. The efficiency showed a mild dependence on length with a loss of roughly 4%/cm.

The final light guides are fabricated from 3.175 cm diameter UV-transparent acrylic rod, each with a length of 5.1 cm. The rods were rough cut to length and then finished on a lathe with a diamond tool. The surfaces are clear but show visible machining marks. There was no discernible benefit in polishing the surfaces as the surface imperfections are filled in by epoxy or the optical coupling material. The light guides were glued to the PMTs using Bicron optical epoxy and then loosely wrapped in aluminized mylar.

FEU 84-3 photomultiplier tubes

The PMT's used for the GLUEX experiment are Russian-made FEU 84-3 PMTs. This is a twelve-stage PMT with a active photocathode diameter of 2.5 cm. The average quantum efficiency is 20% with a peak response int the blue (420 nm - 500 nm) portion of the spectrum and a gain at 1800 V is about 5×10^6. Many PMTs were recycled from the E852 and RADPHI experiments. At the start of construction about 2700 PMTs were available. In order to have a sufficient number to operate the detector and have spares on hand an additional 451PMTs were fabricated by a Russian company MELZ according to the design of the original FEU 84-3 PMT. These replacement PMTs had performance characteristics that met or exceeded the original PMTs.

The PMT's available for GLUEX were used in E852 starting in 1994. There was some concern about the aging of the PMT's so a program of testing the PMT's was carried out. A similar process was used prior to constructing the E852 LGD for rating PMT's and is described in reference [72]. The tubes were tested in a light tight box and illuminated diffusely by LEDs

[36]Material is manufactured by Eljen: EJ-560 Optical Interface Material

behind a frosted glass plate. Under computer control the gain as a function of high-voltage was recorded and random noise and correlated noise rate was measured. The correlated noise rate will be measured within a fixed gate delayed by a few hundred nanoseconds after the LED's are pulsed. In total, nearly 3200 PMTs were tested. Of these, about 3100 were deemed acceptable for production use in the detector. Details of the testing and analysis can be found in Ref. [**?**].

Magnetic shielding

The FCAL sits near the open downstream bore of the GLUEX solenoid. Calculations of the maximum field in the vicinity of the FCAL suggest a field on the order of 150 Gauss may be present during operation[37]. Based on testing of an FEU 84-3 PMT in a Helmholtz coil, the maximum allowable magnetic field transverse to the axis of the PMT was determined to be 2 Gauss. The most sensitive portion of the PMT is the large volume of space between the photocathode and the first dynode. (No degradation in PMT gain was observed for relatively large fields applied to the downstream end of the tube.) The 2 G requirement necessitated that the PMT photocathode be recessed inside of a double-layer magnetic shield.

The outer shield was made from 1026 seamless steel tubing that had been machined on the outside to have a square profile. The inner diameter was 3.81 cm and the average thickness of the steel in the radial direction is about 3 mm. The steel was coated with a zinc-phosphate coating to prevent rusting. The inner shield was made from 0.36 mm thick μ-metal[38] rolled into a tube with an inner diameter of 3.49 cm and a length of 13.46 cm. The rolled shield was welded and then subsequently annealed. The shield combination was tested in a dipole magnet at Jefferson Lab and was capable of attenuating a 185 G field to less than 2 G at a distance of about 3 cm from the opening of the shield, and 0.5 G at 5 cm from the opening. This is more than sufficient to meet the requirement of 2 G at 5 cm for a 150 G external field.

Cockcroft-Walton PMT bases

The Cockcroft-Walton (CW) base design described in reference [73] was modified somewhat for GLUEX and 100 prototype bases were constructed in 2003. These were tested at IU from 2003 - 2009. In 2009 work began on the final production design for the GLUEX FCAL base.

In the new design, the supply voltage of 24 Volts is boosted up to 180 Volts by an inductive boost circuit. The 180 Volts feeds a diode-capacitor Cockcroft-Walton multiplier which provides cathode and dynode PMT bias voltages directly. An ST Microelectronics STM8S208RB processor chip enables and disables the multipliers and handles bi-directional communication via a Controller Area Network (CAN) bus. The processor chip also includes ADCs, seven of which which are used to monitor various voltages in the base as well as the base temperature and current consumption. The CAN bus is limited to 100 nodes per segment, so this means the FCAL is divided into 28 segments for control and monitoring.

A major change from previous versions is a square cross section case. Previous versions were housed in a round cross section case which limited the internal board arrangement and required hand wiring or flex circuitry. Going to a square cross section allowed the use of standard board stacking connectors. The internal circuitry is divided onto 4 boards: The COMM

[37] This estimate was based on earlier calculations that included no additional iron cladding on the solenoid. Iron cladding was added to the solenoid to reduce saturation in the iron yoke at the downstream end and, consequently, reduce the fringe field at the FCAL.

[38] The material specification is AD-MU-80 provided by Advance Magnetics in Rochester, IN.

board contains the processor and CAN bus communication. The MULT board contains all the voltage multiplication circuitry. The TRAN board rearranges the various dynode voltages for connection to the PMT. The SOCK board connects these voltages to the PMT socket, and contains some bypass capacitors for the last few dynodes as well as a self-test pulser. A short piece of RG-196 coax carries the PMT anode signal from the PMT socket to the back panel LEMO 00.250 output connector.

The temperature stability of this base has been tested and compared to conventional resistor based voltage dividers [**?**]. No temperature dependence was found within the accuracy of the measurement by monitoring the gain stability. The gain is found to be stable on the order of 0.1%/°C. Long term operational tests have also been performed and no indications of base failure were observed.

The use of CW PMT bases has many advantages over conventional resistor bases. The most notable difference is power consumption and consequently generated heat. When operating normally the CW bases consume less than 150 mW of power per base. Since high voltage is generated directly on the base, the design eliminates the need for an 2800-channel high voltage distribution system resulting in not only reduced cost but also improved safety.

The CW PMT bases are powered from 24 Volts DC. Rack mounted 1U chassis were constructed which contain 8 modular, high efficiency switching supplies. Each supply can power one string of 100 bases. This chassis also has interlock inputs and outputs as well as fanouts for base RESET and test pulse SYNC signals. An internal STM8S208RB processor's ADCs are used to monitor the voltage and current for each string of 100 bases via CAN. Fuses protect the ribbon cable wires which carry the power to bases on each string.

LED-based monitoring system

The FCAL relative-gain monitoring system is designed to track the stability of the PMT output signals between calibrations with particles and, at the same time, check for any possible radiation damage. The system is composed of light emitting diode (LED) light sources. Since the radiation damage – if present – is expected to be more pronounced in the blue region of the visible spectrum, we opted to calibrate using LEDs of different colors in order to continuously monitor the whole spectrum where the PMTs are sensitive.

The monitoring system is mounted on Plexiglas panes which are mounted very close to the front faces of the 2800 FCAL modules. The layout of the FCAL monitoring system is shown in Fig. 3.30. The space between the Plexiglas and the front faces of the Pb-glass is about 3/8". The Plexiglas is divided into four different quadrants leaving a square hole in the middle for the beam passage. Each quadrant is flashed by a group of 10 LEDs, five on one side and five on the side perpendicular to the first one as shown in Fig. 3.30. Each group of four LEDs of different color is assembled on the same board, called *FCAL-LED4* board.

The LED boards shown in the top panel Fig. 3.31, have a height of 15 mm – approximately equal to the thickness of the Plexiglas panes – and are driven by control boards (*FCAL-CRTL*) shown in the bottom panel. Each LED of different color is triggered independently of the other colors but is self triggered. So every *FCAL-CRTL* of each quadrant, receives four triggers from the outside world which are, in turn, fanned out, together with DC voltages for the LEDs, to the *FCAL-LED4* boards by ten ribbon cables. On the *FCAL-CRTL*, a connector to the outside world where the triggers and the low voltage power will be connected is shown in Fig. 3.32.

The ten *FCAL-LED4* boards are clamped on the side of the Plexiglas, along its width, as

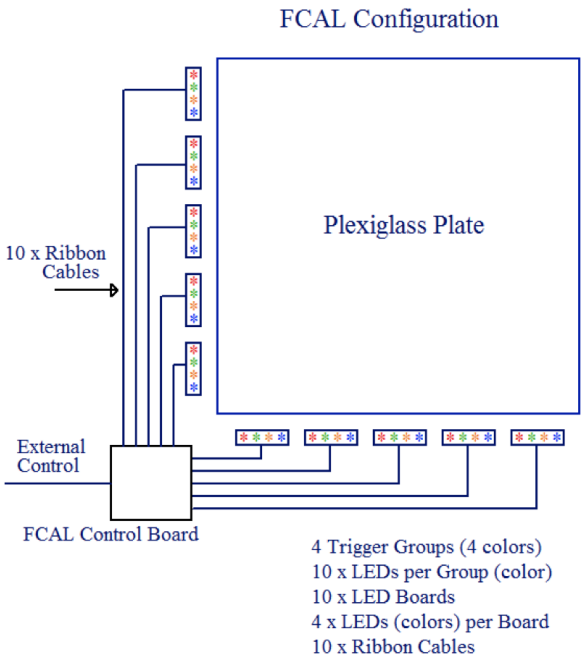

Figure 3.30: FCAL LED monitoring system configuration.

shown in Fig. 3.33. The different color LEDs come from the following companies: Satistronics emitting at 390nm (UV) and Kingbright emitting at 470nm (blue), 525nm (green) and 574nm (green). The LEDs are attached to a single PCB board as explained above so that they emit light parallel to the long axis of the Plexiglas.

Mechanical assembly

Detector operation

Environmental monitoring and control

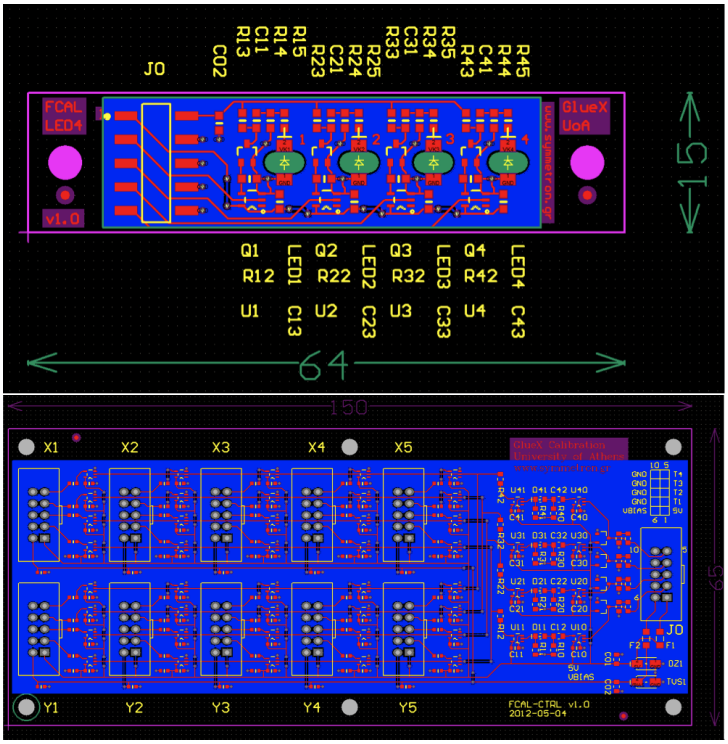

Figure 3.31: FCAL monitoring system LED and Controller boards.

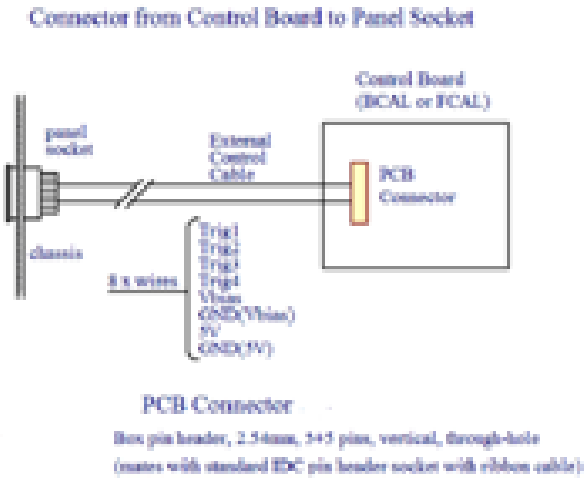

Figure 3.32: FCAL monitoring system PCB connection.

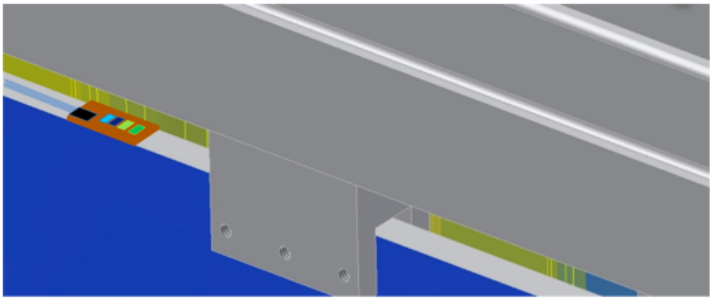

Figure 3.33: FCAL monitoring LED positioning on the Plexiglas edge.

3.5 Straw-tube Central Drift Chamber

3.5.1 CDC Summary [39]

The main parameters and properties of the CDC are given in Tables 3.11 and 3.12. The assembly drawing for the CDC is D000000102-1000.

Table 3.11: CDC properties.

Straw Length	150 cm
Straw ID	15.52 mm
Wall thickness	109 μm
Aluminum layer	30 nm
Thickness (28 layers)	
Mylar	2.22% Rad.Length
Gas	0.34% Rad.Length
Thickness(End Plate)	2.14% Rad.Length
Gas	50% Ar / 50% CO_2
Gas Flow	$\sim$ 3 ℓ/min
Preamps (GASS-2)	149 cards
fADC125-MHz, 72 ch	50 modules
HV CAEN A1550P	+2110V
LV, MPOD MPV8008	$<$ 8V, 0.47A/card
Drift position σ	$\sim$ 200 μm

Table 3.12: CDC channel counts.

Layer	Type	Straws
1 (inner)	Axial	42
2	Axial Close Packed	42
3	Axial	54
4	Axial Close Packed	54
5	Stereo +6°	66
6	Stereo Close Packed	66
7	Stereo +6°	80
8	Stereo Close Packed	80
9	Stereo -6°	93
10	Stereo Close Packed	93
11	Stereo -6°	106
12	Stereo Close Packed	106
13	Axial	123
14	Axial Close Packed	123
15	Axial	135
16	Axial Close Packed	135
17	Stereo -6°	146
18	Stereo Close Packed	146
19	Stereo -6°	158
20	Stereo Close Packed	158
21	Stereo +6°	170
22	Stereo Close Packed	170
23	Stereo +6°	182
24	Stereo Close Packed	182
25	Axial	197
26	Axial Close Packed	197
27	Axial	209
28 (outer)	Axial Close Packed	209
Total		3522

[39] *SVN revision ID:* tdr_summary_cdc.tex 13854 2014-06-12 04:42:15Z gen

3.5.2 Overview

The Central Drift Chamber (CDC) is used to track charged particles, providing timing and energy loss measurements. The CDC is a cylindrical straw-tube drift chamber situated within the upstream end of the GlueX solenoid that surrounds the target and start counter, as shown schematically in Figure 3.34, with dimensions given in Table 3.13. Its active volume is traversed by particles coming from the target with polar angles between 6° and 168°, with optimum coverage for polar angles between 29° and 132°.

Prior to construction of the CDC, the materials were evaluated and used to build two smaller prototype chambers. These prototypes were then used to study chamber characteristics and performance, including choice of gas mix and dE/dx simulations, reported elsewhere [74].

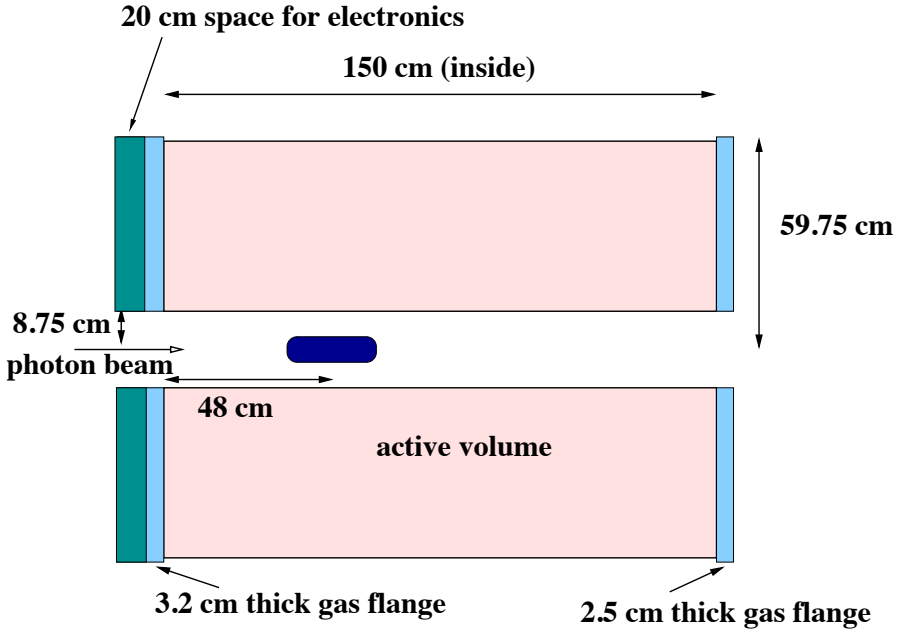

Figure 3.34: A side view of the CDC.

Active volume inner radius:	9.92 cm
Active volume outer radius:	55.54 cm
Active length:	150.0 cm
Chamber assembly inner radius:	8.75 cm
Chamber assembly outer radius:	59.74 cm
Upstream gas plenum length :	3.18 cm
Downstream gas plenum length :	2.54 cm

Table 3.13: Geometry of the CDC's active volume and gas plenums

The CDC contains 3522 straw tubes of diameter 1.6 cm in 28 layers, located in a cylindrical volume with an inner radius of 10 cm and outer radius 56 cm, as measured from the beamline. Each straw tube contains an anode wire of 20 μm diameter gold-plated tungsten. The inner wall of the tube forms the cathode, ensuring uniformity of electric field around the wire. The

straws contribute structural rigidity to the assembly, supporting the tension on the wires, and also prevent the wires from making contact with their neighbors, which would cause electrical problems in the event that one should break. The number of straws within each layer is given in Table 3.14.

Layer	Straws	Radius (cm)	Layer	Straws	Radius (cm)
1	42	10.7219	15	135	34.4343
2	42	12.0797	16	135	35.8128
3	54	13.7802	17	146	37.4446
4	54	15.1447	18	146	38.8314
5	66	16.9321	19	158	40.5369
6	66	18.3084	20	158	41.9248
7	80	20.5213	21	170	43.6152
8	80	21.9009	22	170	45.0038
9	93	23.8544	23	182	46.6849
10	93	25.2362	24	182	48.0737
11	106	27.1877	25	197	50.3747
12	106	28.5712	26	197	51.7597
13	123	31.3799	27	209	53.3631
14	123	32.7577	28	209	54.7464

Table 3.14: The number of straws in each layer of the CDC, and the central radius of each layer, as measured from the beamline at a point halfway between the endplates.

The tracking volume is enclosed by an inner wall of G-10, outer wall of aluminum, a downstream carbon fiber endplate, and an upstream aluminum endplate. The endplates are linked by 12 aluminum support rods which were bolted into place to maintain the relative location and orientation of the endplates after alignment. Fig. 3.35 shows the endplates, inner shell, and support rods before the straws were installed. The holes in the endplates were milled precisely to correctly position the ends of the straws.

There is a cylindrical gas plenum next to each endplate - the upstream plenum has polycarbonate walls and a polycarbonate endplate, while the downstream plenum has Rohacell sidewalls and a ring-shaped end-wall of mylar film, aluminized on both sides. The inner and outer shells are sealed along their seams and where they meet the endplates, forming an outer plenum around the straws. The materials used for construction were chosen to minimize the amount of material in the tracking volume, especially at the downstream end. They are listed in Table 3.15.

A length of 20 cm is reserved for the electronics, which are mounted on standoffs on the polycarbonate endplate. Threaded holes in the polycarbonate endplate allow signal wires to pass through the gas plenum. These are sealed with an O-ring and a threaded bushing which is torqued into place.

3.5.3 CDC construction

Straws

The straw tubes are 0.8 cm radius aluminized mylar tubes, manufactured by Lamina Dielectrics from 100 μm thick mylar tape with approximately 30 nm of aluminum vapor-deposited onto

Figure 3.35: CDC frame prior to the installation of the straw tubes.

one side, wound into a tube with the aluminum facing inside. The electrical resistance of each straw, from one end to the other, is between 75 Ω and 100 Ω. The straws are arranged in 28 radial layers surrounding the inner shell, as shown in Fig. 3.36. 12 of the layers are axial (parallel to the beam axis) and the remaining 16 are placed at stereo angles of ±6°. These are ordered such that the innermost 4 layers are axial, followed by (at increasing radius) 4 layers at +6°, 4 layers at −6°, 4 axial layers, 4 layers at −6°, 4 layers at +6° and 4 axial layers. The layers are paired and located so that the first layer of each pair contains the largest number of straws possible for its radius, and the straws in the second layer are close-packed against those in the first. This is illustrated in Fig. 3.37.

A non-conductive epoxy is used to glue each straw tube to its neighbors within the same layer at three points evenly distributed along its length. In the first layer of each pair, every sixth straw is also glued to the straw behind it. In the second layer of each pair, every straw is glued to the straw behind it. Fig. 3.38 shows straws in opposing stereo layers 8 and 9 and Fig. 3.39 shows the outermost row of straws, with the outer shell partly installed. The number of straws in each layer is listed in Table 3.16, together with the radial distance of each wire, relative to the beamline at the center of the chamber, and at the inside face of the two endplates. Table 3.20 gives the position of the wires at each endplate, and relative to the chamber center.

Upstream endplate:	0.9525 cm Al (3/8" plate)
Downstream endplate:	0.6 cm Carbon Fiber
Support rods (12):	Al
Upstream inner hub	Al
Downstream inner hub	G-10
Thickness of inner shell (mm):	0.5 mm G-10
Upstream outer hub	G-10
Downstream outer hub	G-10
Thickness of outer shell (mm):	1.6 mm Aluminum 6061
Outer shell joints:	Scotch 27 glass cloth electrical tape
	5.04 cm wide strip of military duct tape
	2.54 cm wide 1.27 mm thick Cu tape
Outer shell connections to endplate (21) :	approx. 3 cm x 2.54 cm x 0.05 mm Al tabs
Outer shell connections to endplate (2) :	approx. 3 cm x 2.54 cm x 0.05 mm Cu tabs
Strawtube (inner diameter):	1.552 cm
Strawtube (material):	Aluminized Mylar
Strawtube (thickness):	114(0.1) μm Mylar(Al)
Upstream donuts and feedthroughs (3522):	Al
Downstream donuts and feedthroughs (3522):	Noryl plastic
Pinholders (7044):	Noryl plastic
Crimp pins (7044):	Au plated Cu
Anode wires (3522):	20 μm gold-plated W
Upstream plenum sidewall:	3 mm Polycarbonate and 1.27 mm Cu tape
Upstream plenum endwall:	15.8 mm Polycarbonate
Downstream plenum sidewall:	2.54 cm Rohacell
Downstream plenum endwall:	50 μ m Aluminized Mylar
Gas pipes (6):	Al, inner diameter 6.35 mm
Gas line widgets (6):	plastic
Gas line widgets (6):	Al
Hose barbs (6):	stainless steel
Thermocouples (10)	Constantan Cu-Ni, Kapton coating
Conductive epoxy:	920-H
Non-conductive epoxy:	DP-190 (straw assembly)
Non-conductive epoxy:	DP-460NS (outer shell and hubs)

Table 3.15: Construction materials

Layer	Straws	Radius (cm) (center)	Radius (cm) (end plate)	Stereo (radians)
1	42	10.7219	10.7219	0.00000
2	42	12.0797	12.0797	0.00000
3	54	13.7802	13.7802	0.00000
4	54	15.1447	15.1447	0.00000
5	66	16.9321	18.6765	0.10470
6	66	18.3084	20.1945	0.11314
7	80	20.5213	21.9827	0.10470
8	80	21.9009	23.4606	0.11168
9	93	23.8544	25.1226	−0.10470
10	93	25.2362	26.5780	−0.11072
11	106	27.1877	28.3070	−0.10470
12	106	28.5712	29.7475	−0.10999
13	123	31.3799	31.3799	0.00000
14	123	32.7577	32.7577	0.00000
15	135	34.4343	34.4343	0.00000
16	135	35.8128	35.8128	0.00000
17	146	37.4446	38.2650	−0.10470
18	146	38.8314	39.6822	−0.10855
19	158	40.5369	41.2959	−0.10470
20	158	41.9248	42.7099	−0.10826
21	170	43.6152	44.3216	0.10470
22	170	45.0038	45.7326	0.10801
23	182	46.6849	47.3455	0.10470
24	182	48.0737	48.7539	0.10779
25	197	50.3747	50.3747	0.00000
26	197	51.7597	51.7597	0.00000
27	209	53.3631	53.3631	0.00000
28	209	54.7464	54.7464	0.00000

Table 3.16: The number of straws in each layer of the CDC. The radius at the center is the wire location half-way between the two endplates. The radius at the endplates is where the wire passes through the end plate. For axial layers, both radii are the same. For the stereo layers, the radius at the endplate is larger than it is at the center.

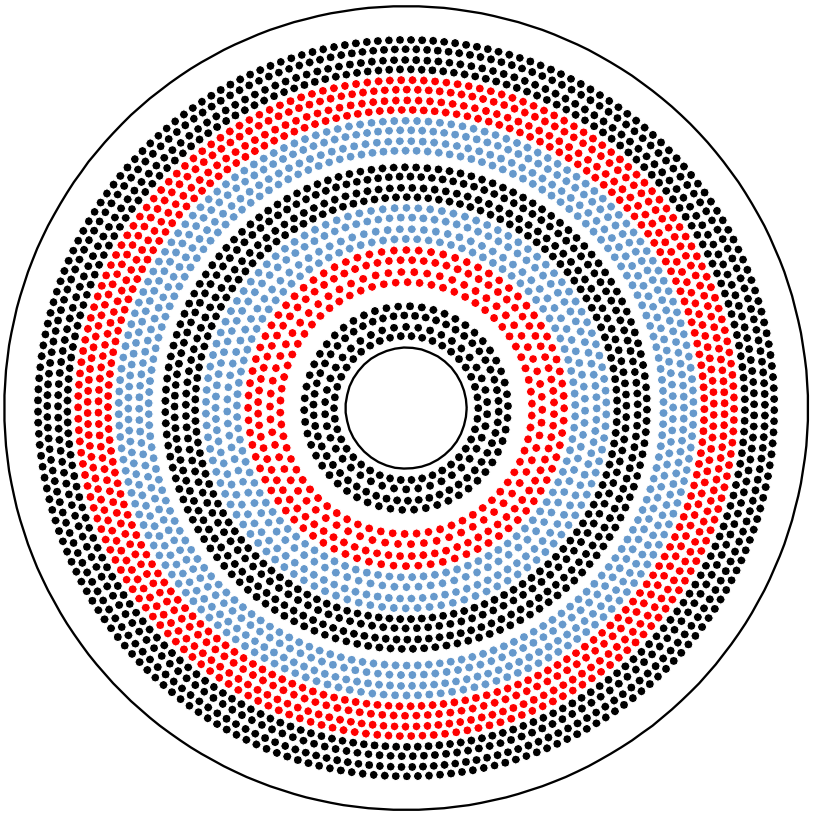

Figure 3.36: Diagram showing the position of the straws at the upstream endplate. The axial straws are shown in black, the $+6^\circ$ stereo layers are shown in red and the -6° stereo layers are shown in blue.

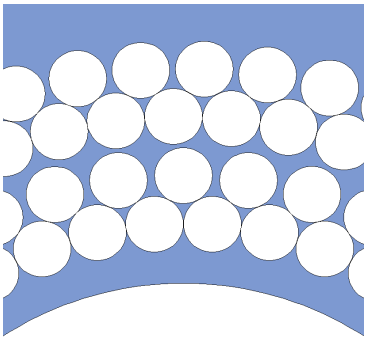

Figure 3.37: Diagram showing close-packing of the straws in a small section of rows 1 to 4.

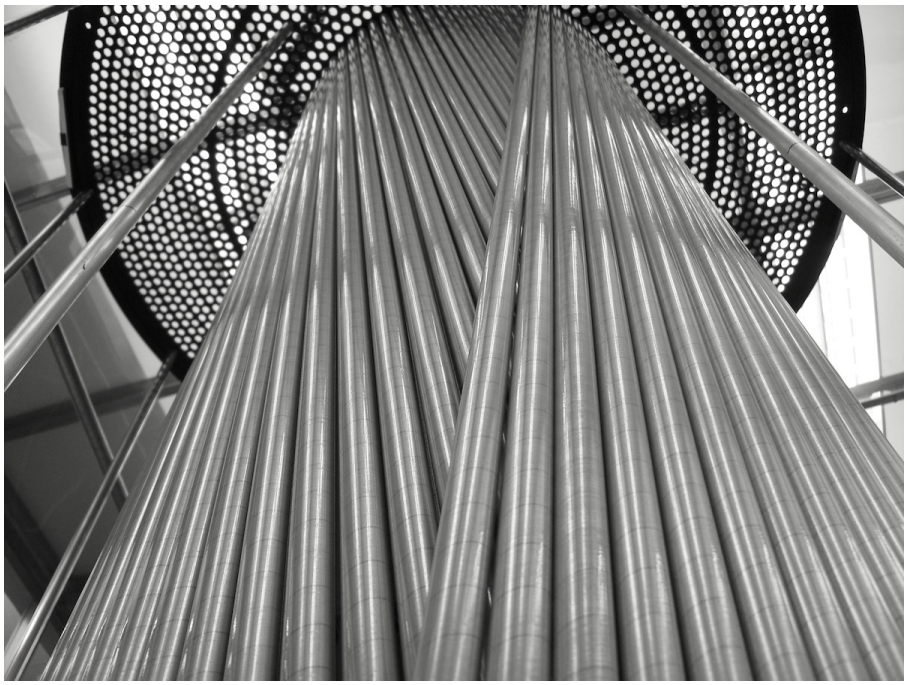

Figure 3.38: Straw tubes in stereo layers 8 and 9.

Figure 3.39: Straw tubes in layer 28, with one half of the outer shell in place.

Straw and wire assembly

The straw assembly components are shown in Fig. 3.40. A 'donut' ring is glued inside each end of the straw, and a 'feedthrough' tube is glued through the endplate into the donut, and holds the straw in position. Depending on the endplate, there are two types of donuts, feedthroughs, and epoxy used: Noryl plastic donuts and feedthroughs are glued into the carbon fiber endplate with non-conductive epoxy, and aluminum donuts and feedthroughs are glued into the aluminum endplate with silver conductive epoxy. The conductive epoxy ensures that the electrical grounding of the aluminum endplate is shared with the aluminum feedthroughs, donuts, and the aluminum layer on the inside of the straw. Sufficient epoxy is used to make each joint gas-tight.

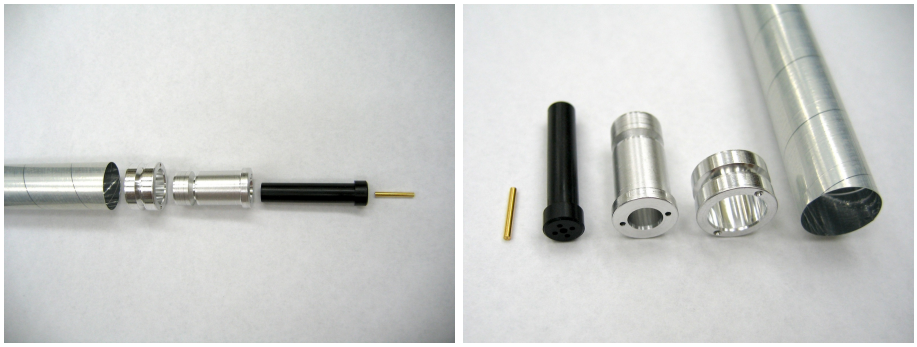

Figure 3.40: Straw, donut, feedthrough, pinholder and crimp pin.

The donuts and feedthroughs were manufactured to a CMU design which features a recess ('glue trough') partway down the outside of each component, accessed by 2 small holes ('glue-ports') bored lengthwise into the component wall. This permitted epoxy to be injected through one glue-port into the glue trough, allowing for air to exit through the partner glue-port, thus enabling a strong joint to form as the epoxy makes good contact with both surfaces. The dimensions of these components are given in Table 3.17.

Component	Inner diameter	Outer diameter	Length
Straw (straight)	1.552 cm	1.575 cm	149.809 cm
Straw (stereo)	1.552 cm	1.575 cm	150.571 cm
Donut (top)	1.111 cm	1.575 cm	0.063 cm
Donut (rest)	1.111 cm	1.552 cm	0.889 cm
Al feedthrough (top)	0.635 cm	1.270 cm	0.254 cm
Al feedthrough (rest)	0.635 cm	1.111 cm	2.159 cm
Noryl feedthrough (top)	0.635 cm	1.270 cm	0.254 cm
Noryl feedthrough (rest)	0.635 cm	1.111 cm	1.803 cm
Pinholder (top)	0.147 cm	0.787 cm	0.396 cm
Pinholder (rest)	0.508 cm	0.635 cm	2.906 cm
Crimp pin	0.0203 cm	0.147 cm	1.206 cm

Table 3.17: The dimensions of the straw assembly components

The anode wires are held in place by gold-plated copper crimp pins inside Noryl plastic tubes 'pinholders', which were inserted into the feedthroughs. The inner diameter of the pin-

holder top is at first 1.47 mm, a very close fit with the crimp pin, then after 6 mm of length the diameter is reduced to 1.27 mm for a further length of 1.63 mm to hold the crimp pin in place, before opening out to a diameter of 5.08 mm for the rest of the length.

The pins were crimped when the wire was under 30 g-force of tension, applied by suspending a weight from the wire, with the chamber orientated so that the wire was hanging vertically. The anode wire is 20 μm diameter tungston with a flash coating of gold, supplied by Luma-Metall Each pinholder has 4 additional holes surrounding the crimp pin which permit gas to flow in and out of the straw.

Wire tension measurements

The tension on each wire was measured a few weeks after stringing, and again some time later, using two Helmholz coils and a control device which alternated between applying a sinusoidal voltage along to the wire and measuring the induced current on the wire. The wire tension was calculated from the frequency of the applied voltage when the system reached resonance. This technique is described elsewhere [75]. The tension measurements were interleaved with the stringing work and a few wires with very low tension were found and replaced during this time. When stringing was complete, all the wires had tension between 27 and 32 g-force. The chamber is shown with the Helmholz coils in place in Fig. 3.41.

Figure 3.41: Wire tension measurement

Gas flow

Six aluminum tubes of inner diameter 6.35 mm run the length of the CDC, close to the inside wall of the outer cylindrical shell, taking the gas supply from outside the upstream end through the polycarbonate plate and both endplates into the downstream plenum, where the gas enters the straw tubes through the holes in the pinholders. The gas passes through the straw tubes into the upstream plenum and then through ten holes in the lower half of the aluminum endplate into the void between the straws and the outer shell of the CDC. Six holes near the top of the aluminum endplate permit the gas to leave the void through exhaust tubes. Five thermocouples within each plenum enable the temperature of the gas to be monitored. The gas used is a mixture of 50 % CO_2 and 50 % Ar at atmospheric pressure.

Electrical shielding

Electrical shielding is required to minimize the amount of electromagnetic noise picked up by the signal wires. The aluminum endplate is the common ground for the straw tubes and also the outer shell, which provides electrical shielding around the tubes. Each half of the outer shell is glued to the aluminum endplate and G-10 outer hub with non-conductive epoxy. In order to ensure a good electrical connection, tabs of aluminum are glued over the join between the outer shell and the endplate with conductive epoxy at twenty points around the outer radius.

The long straight edges of the two halves of the outer shell were covered with non-conductive glass-cloth electrical tape and then joined together with a layer of 2-inch wide military duct tape. A strip of 1-inch wide copper tape with a non-conductive backing was applied along the center of the duct tape. The copper tape is grounded to the endplate by a tab of copper attached with conductive epoxy and then covered over with two more layers of the military duct tape. This arrangement ensures that the sidewalls of the cylindrical outer shell have a good connection to the grounded aluminum endplate, while the discontinuity between the two halves of the shell prevents eddy currents from spiraling around the CDC in the event of a magnet quench.

The upstream outer gas plenum sidewall is covered with 0.005 inch thick copper tape. A copper braid is soldered to the tape at intervals and glued to the aluminum endplate with conductive epoxy. The downstream plenum endwall material is mylar, aluminized on both sides. Rectangular tabs extend outwards from the endwall around its radius. These are glued to the sidewall and outer shell with conductive epoxy.

Grounded shielded extension cables are used for the downstream thermocouples along the length of the CDC, and for all the thermocouples from the upstream end to the electronics racks, in order to minimize any electrical pickup.

3.5.4 Electronics

The hookup wires, which pass through the polycarbonate endplate and onto the crimp pins inside the upstream gas plenum, were made from RG−316 wire as follows: at one end of the wire, the inner conductor was exposed for approximately 5 mm and the teflon dielectric was exposed for a further 5 mm. The end of the shielding braid was sealed with epoxy to prevent gas from migrating along the cable inside the braid. A silver bead was soldered onto the end of the center conductor and then covered with a narrow tube of conductive rubber, approximately 15 mm long, which fits tightly over the bead. Heat-shrink was then used to seal over the region

from the end of the outer covering and braid to the end of the conductive rubber tube. An O-ring and threaded bushing were fed onto the hookup wire before its other end was finished by stripping back the braid 10 mm and then soldering a ferrule to the braid, then stripping the dielectric 5 mm from the end of the wire. Two hookup wires, one complete and one partly assembled, are shown in Fig. 3.42. The length of wire used for each connection was between 9.3 cm and 12.5 cm; this was chosen to be as short as possible, without causing excessive strain on the solder joints.

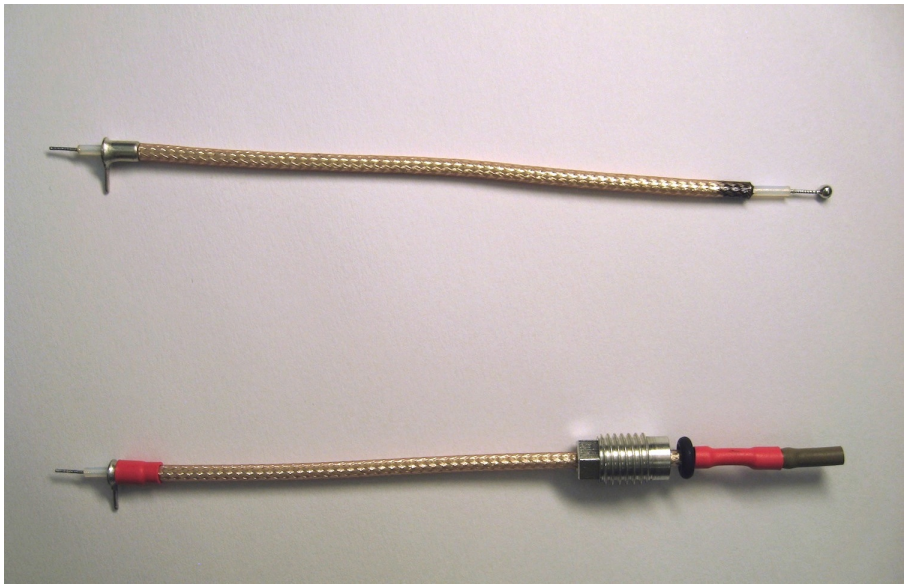

Figure 3.42: Two hookup wires, the upper wire is part-assembled and the silver bead is visible.

The polycarbonate endplate was polished to transparency so that the crimp pins would be clearly visible through it. Each hookup wire was installed by insertion through a threaded hole in the polycarbonate endplate and sliding the conductive rubber over the corresponding crimp pin until it made a snug fit as the silver bead made contact with the end of the pin. The O-ring and threaded bushing were then fitted into the hole in the endplate, and the ferrule and center conductor at the other end of the hookup wire were soldered onto pads of a transition board. The transition boards are mounted onto standoffs located on the polycarbonate endplate - one standoff mounts directly to the polycarbonate endplate while the other (grounding) standoff threads onto another standoff which is mounted onto the Al endplate and protrudes through a hole in the polycarbonate endplate, sealed with an O-ring.

There are 149 transition boards with each board having between 20 to 24 hookup wires soldered to it. The hookup wires that are attached to any given transition board come from 3 to 4 neighboring rows of straws. Some of the transition boards and standoffs are shown in Fig. 3.43. Each transition board houses a 30-pin connector for installation of a high voltage board (HVB) that provides approximately 2 kV for up to 24 wires, 2 connections of approximately 2 kV for the shielding braids, 2 ground connections to the grounding standoffs and 2 unused connections which are located between the HV and ground connections. In addition to providing voltages, the HVB boards also house the preamplifier cards.

The preamplifiers have 24 channels per board, are charge-sensitive, and capacitative coupled to the CDC. The preamplifiers are connected to 125 MHz 12-bit flash ADCs, with three

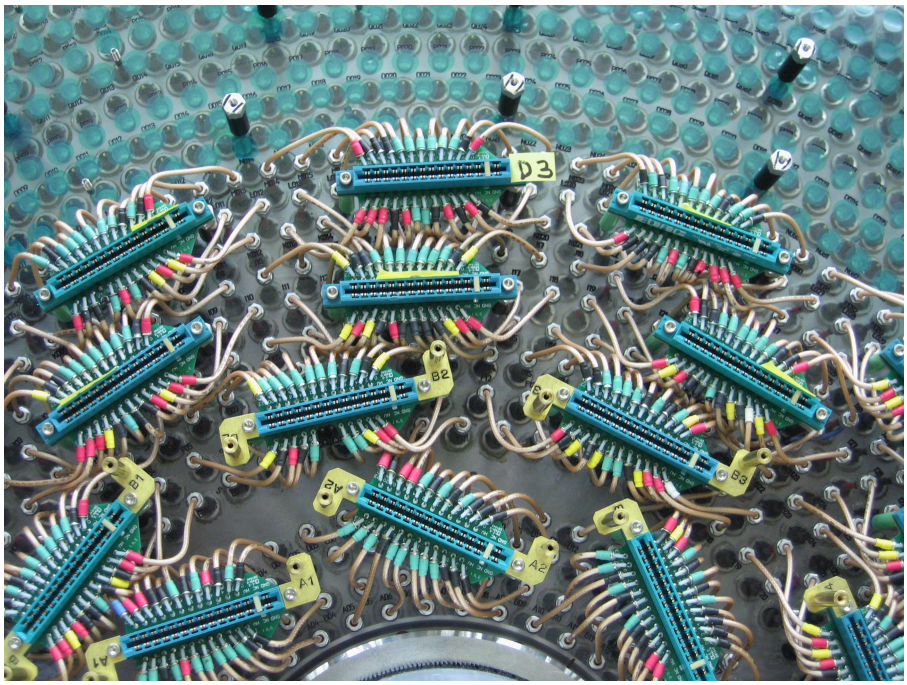

Figure 3.43: Hookup wires and transition boards.

preamps to each fADC. The preamplifiers and fADCs are described in detail in the section on electronics.

3.5.5 Chamber operating parameters

The background noise present on the wires is important in determining the operating parameters for the CDC, and thus the range of dE/dx measurements possible. During calibration, measurements are made of the mean and standard deviation (σ) of the pedestal height (the ADC value in the absence of an event). The pedestal height is adjusted by downloading a data file into the fADC, it is set at approximately 3σ to 4σ in order to maximize use of the fADC range.

The choice of the gas mixture is described elsewhere [74]. The anode voltage is chosen such that the minimum ionizing peak in the amplitude histogram, from tracks at 90° to the straws, lies above the background noise. This is done by setting the anode voltage to match the hit threshold, typically 5σ, to a low percentile (1% to 5%) of the distribution within the 4095 channel range of the fADC. Table 3.18 shows estimates of the dynamic range for conditions typical of the small prototype chamber operating at voltages close to $2\,kV$ with a gas mixture of 50 % CO_2 and 50 % Ar at atmospheric pressure giving a gas gain of approximately 3×10^5, and the 5σ hit threshold matched to the 1^{st} percentile. For σ of 15 channels this gives a dynamic range of approximately 20 times minimum ionizing at 90°. Table 3.19 shows similar estimates for the hit threshold matched to the 5^{th} percentile, which gives greater dynamic range at the expense of detection efficiency for the minimum ionizing particles.

Pedestal σ	Minimum ionizing peak	Dynamic range
10	140 (170 to 120)	30 (24 to 34)
15	210 (250 to 180)	20 (16 to 22)
20	280 (340 to 240)	15 (12 to 17)
25	350 (420 to 300)	12 (10 to 13)
30	420 (500 to 360)	10 (8 to 11)

Table 3.18: Table of estimates of the dynamic range of the CDC. There is some variation due to the shape of the Landau distribution, the data are given for ratios of the Landau parameters 4MPV/FWHM of 3.3 (3.0 to 3.6) and the 5σ hit threshold is matched to the 1^{st} percentile of the distribution within the range of the fADC, where MPV is the most probable value

Pedestal σ	Minimum ionizing peak	Dynamic range
10	90 (100 to 90)	44 (41 to 47)
15	140 (150 to 130)	29 (27 to 32)
20	180 (200 to 170)	22 (20 to 24)
25	230 (350 to 210)	18 (16 to 19)
30	280 (300 to 260)	15 (13 to 16)

Table 3.19: Table of estimates of the dynamic range of the CDC. There is some variation due to the shape of the Landau distribution, the data are given for ratios of the Landau parameters 4MPV/FWHM of 3.3 (3.0 to 3.6) and the 5σ hit threshold is matched to the lower 5^{th} percentile of the distribution within the range of the fADC, where MPV is the most probable value

3.5.6 Timing method and position resolution

The fADCs are programmed to output data in two alternative modes - a 'raw' mode, intended for development and diagnostics, where a full sample window of 512 samples is read out for each channel, and a 'run' mode, where the output consists of only a few quantities, representing drift time, pedestal height and integrated charge, for only those channels where a hit occurs. The algorithms used to determine the drift time and energy loss were developed using the small 24-channel prototype chamber and are included in the fADC firmware. The drift time is converted into a drift distance in offline software.

The timing algorithm is activated by the trigger signal and performs a search through the raw sample data buffered in the fADC to identify a hit signal, if there is one, and return the time corresponding to its leading edge. It uses several thresholds which can be related to the pedestal standard deviation, σ. These are determined during calibration and uploaded into the fADC firmware as constants. Values optimized using the small prototype are available as a starting point: hit identification threshold $T_{hit} \sim 5\sigma$, high timing threshold $T_h \sim 4\sigma$, low timing threshold $T_l \sim \sigma$ and pedestal lead time $N_p \sim 4$ for σ of 15. The hit search window, W_s to W_e, specifies the range of samples to be searched for a hit, following the trigger.

1. The event pedestal, P_{evt}, is found, as the mean of 4 samples ending at the start of the hit search window, sample W_s.

2. The samples within the hit search window are searched for a hit, which is found if the data exceed a high threshold $P_{evt} + T_{hit}$ at point x. If no hit is found, no further action is taken.

3. The local pedestal, P_{loc}, is obtained as the ADC value at N_p samples before x.

4. The algorithm searches through the samples from $x - N_p$ toward W_e to find sample x_h, where the ADC value first exceeds or equals the high timing threshold, $P_{loc} + T_h$. If this is not found, the algorithm returns an error code and the value of $10(x_h - T_{const})$. The value of T_{const} is set in configuration parameters.

5. It then searches the samples from x_h back toward $x - N_p$ to find sample x_l, where the ADC value is less than or equal to the low timing threshold, $P_{loc} + T_l$.

6. The ADC data are upsampled by a factor of 5 to calculate values at $1.6\,ns$ intervals, from $x_l - 0.2$ to $x_l + 1.2$.

7. The upsampled values are searched from $x_l + 1.2$ down to $x_l - 0.2$ to find the point where the values fall equal to or below $P_{loc} + T_l$, and then interpolated to find the threshold crossing to the nearest tenth of a sample. This quantity is returned by the algorithm as an integer.

The time quantity returned by the algorithm is converted to a time in offline software by multiplying by 0.8 ns, which is one tenth of the sample period. It includes a constant offset, corresponding to the earliest possible drift time (when a track passes through a wire). This offset is determined during offline analysis and subtracted from the drift time returned by the algorithm to give the net drift time, which is then converted to a drift distance using look-up tables calculated beforehand using a GARFIELD [76] model.

The CDC was designed to achieve a position resolution of 150 μm. Data obtained with the small prototype and cosmic rays and analyzed with a simple straight-line track-fitting code give a position resolution which averages around 110 μm; the resolution improves with track distance from the wire, and also signal amplitude, as shown in Fig. 3.44.

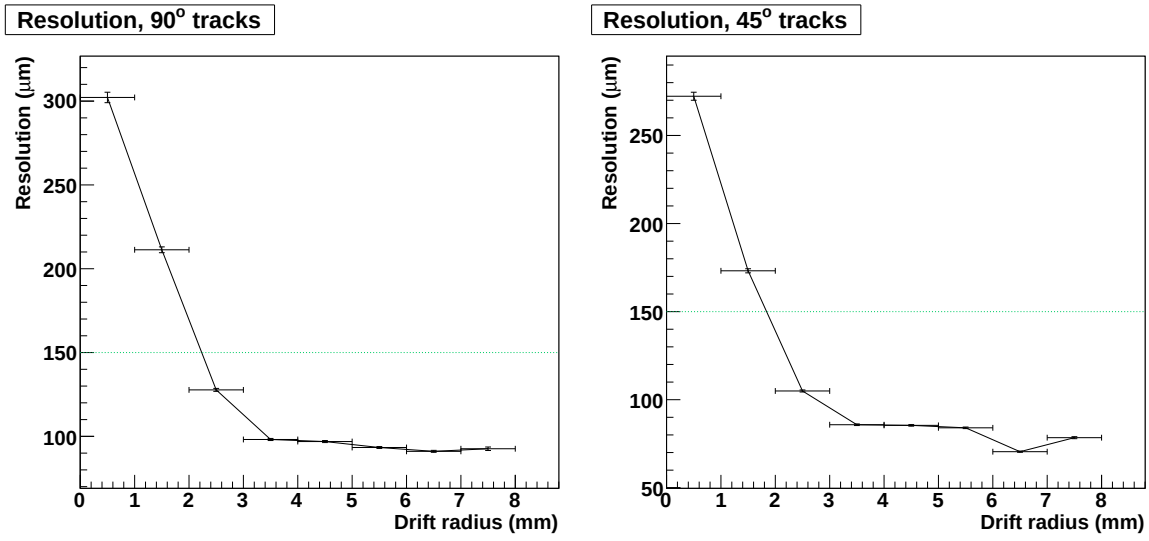

Figure 3.44: Position resolution for cosmic rays with 50/50 mix of Ar and CO_2 at 2090V, with tracks at 90^o (left) and 45^o (right) to the wires.

Layer	Straws	$\Delta\phi$	x_u	y_u	x_c	y_c	x_d	y_d
1	42	0.14960	10.7219	0.0000	10.7219	0.0000	10.7219	0.0000
2	42	0.14960	12.0460	0.9027	12.0460	0.9027	12.0460	0.9027
3	54	0.11636	13.7703	0.5246	13.7703	0.5246	13.7703	0.5246
4	54	0.11636	15.0746	1.4555	15.0746	1.4555	15.0746	1.4555
5	66	0.09520	16.9321	7.8813			16.9321	−7.8813
6	66	0.09520	17.8821	9.3834			18.6931	−7.6411
7	80	0.07854	20.6456	7.5497			20.3917	−8.2109
8	80	0.07854	21.7003	8.9161			22.0898	−7.9018
9	93	0.06756	23.8544	−7.8813			23.8544	7.8813
10	93	0.06756	25.5034	−7.4808			24.9402	9.1854
11	106	0.05928	27.1173	−8.1203			27.2560	7.6418
12	106	0.05928	28.7376	−7.6853			28.3924	8.8759
13	123	0.05108	31.3782	−0.3259	31.3782	−0.3259	31.3782	−0.3259
14	123	0.05108	32.7540	0.4965	32.7540	0.4965	32.7540	0.4965
15	135	0.04654	34.4335	0.2324	34.4335	0.2324	34.4335	0.2324
16	135	0.04654	35.7966	1.0749	35.7966	1.0749	35.7966	1.0749
17	146	0.04304	37.5553	−7.3360			37.3260	8.4250
18	146	0.04304	39.1008	−6.7679			38.5115	9.5679
19	158	0.03977	40.4909	−8.1144			40.5816	7.6479
20	158	0.03977	42.0358	−7.5580			41.8055	8.7427
21	170	0.03696	43.5551	8.2073			43.6730	−7.5549
22	170	0.03696	44.7775	9.2977			45.1997	−6.9613
23	182	0.03452	46.7735	7.3376			46.5901	−8.4239
24	182	0.03452	48.0273	8.3862			48.1186	−7.8451
25	197	0.03189	50.3719	−0.5328	50.3719	−0.5328	50.3719	−0.5328
26	197	0.03189	51.7589	0.2780	51.7589	0.278	51.7589	0.2780
27	209	0.03006	53.3622	0.3193	53.3622	0.3193	53.3622	0.3193
28	209	0.03006	54.7343	1.1504	54.7343	1.1504	54.7343	1.1504

Table 3.20: The location of the wires in the CDC. For each layer, the number of tubes, the angular rotation $\Delta\phi$ between tubes, and the (x, y) coordinates of the wire at three z positions are given. The up-stream pair (x_u, y_u) are on the inside face of the up-stream endplate ($z = 0$). The center pair are at the center of the chamber ($z = 0$), and the down-stream pair (x_d, y_d) are on the inside face of the down-stream endplate ($z = 150$). All distances are given in cm and angles in radians.

3.6 Forward Drift Chambers

3.6.1 FDC Summary [40]

The main parameters and properties of the FDC are given in Tables 3.21 and 3.22. The assembly drawing for the FDC package is D000000103-1030.

Table 3.21: FDC properties.

Item	Value
Gas	40% Ar /60% CO_2
Gas flow	$\sim 4\times$ 0.23 ℓ/min
Sense voltage range	+2100 to +2200 V
Field voltage range	0 to -500 V
Sense wire pitch	10 mm
Distance between sense and field wires	5 mm
Cathode strip width	4 mm and 1 mm gap
Cathode thickness	2 μm Cu on 25 μm Kapton
Distance between wire and cathode planes	5 mm
Cathode central area with no copper, diameter	2.6 cm
Insensitive area (thick signal wires) packages 1-2, diameter	6.0 cm
Insensitive area (thick signal wires) packages 3-4, diameter	7.8 cm
Material in the active area (normal)	$4\times$ 0.43 (% r.l.)
Material in the 2.6 cm diameter central area	$4\times$ 0.26 (% r.l.)
Preamps cooling: liquid (Fluorinert) 24°C	0.5 ℓ/s
Wire position resolution	200 μm
Cathode position resolution	280 μm
Resolution along wire	200 μm

Table 3.22: FDC channel counts.

Item	Description	Quantity
Package	6 Cathode-Wire-Cathode assemblies at 0,60,120,180,240,300°	4
Sense wires	20 μm gold-plated W	96×6×4
Sense wire HV	CAEN A1550P, 24 ch	4
Field wires	80 μm gold-plated Cu-Be	97×6×4
Field wire HV	CAEN A1550N, 24 ch	4
U Cathodes	75° to wires, central 24 strips are split in the middle	216×6×4
V Cathodes	-75° to wires, central 24 strips are split in the middle	216×6×4
Preamp Cards	Card (24 ch) with 3 ASIC (GASS-2) @8 ch/chip	528
TDCs (Wires)	JLab F1TDC V3, 48 ch, 97 ps	48
Flash ADCs (Cath.)	JLab fADC125-MHz, 72 ch	144
LV Power	MPOD MPV8008, 8 ch, 5A/ch	9
FDC Vth	MPOD MPV8030, 8 ch, 2.5A/ch	1

[40] *SVN revision ID:* tdr_summary_fdc.tex 13854 2014-06-12 04:42:15Z gen

Overview

The Forward Drift Chamber system (FDC) is used to track charged particles coming from the target with polar angles up to 20°. Tracks at angles greater than 10° also pass through the CDC detector and its associated downstream end-plate. Due to the spiraling trajectories of the charged particles and the high multiplicity of charged tracks passing through the FDC, this system must be able to provide a sufficient number of measurements with appropriate redundancy to enable the linking of hits from the different tracks with high accuracy, while providing good spatial resolution with reasonable direction information. The chosen technology is a Cathode Strip Chamber in which the two cathode planes facing each wire plane are divided into strips at an angle with respect to the wires. In addition to the charge induced on the strips, the timing information from the wires is read out, enabling reconstruction of both a coordinate along the wire, as well as a coordinate transverse to the wire (using the drift time). This allows the reconstruction of "space points" and facilitates the association of adjacent hits with each other, thereby enhancing pattern recognition.

The most critical requirement in the FDC design is to minimize the amount of the material in the active area of the chamber and at the periphery: frames, supporting systems, and cables. At low momenta, the thickness of the detector in the active area limits the momentum resolution. Photons from meson decays may convert in the detector frames or other materials and may not be properly reconstructed by the BCAL due to the strong magnetic field. Therefore the amount of material at the periphery affects directly the efficiency of photon reconstruction. At the same time the mechanical structure must be robust enough to minimize the frame deformations and to allow for a good gas containment.

The central region of each chamber is close to the beam line and require a special configuration to handle the otherwise unmanageable rates on the strips in this region.

The chambers are positioned inside the bore of the solenoid where the strength of the magnetic field is largest. The direction of the magnetic field is roughly perpendicular to the wires. Not only does this affect the drift time of the electrons toward the wires but the Lorentz force causes a deflection of the avalanche position along the wire relative to the case where there is no magnetic field. The latter effect can be minimized with an appropriate choice of gas mixture. Further details are provided in Section 3.6.1.

The FDC detector includes four separate but identical [41] disk-shaped packages as shown in Fig. 3.45. Each package includes six independent planar drift chambers, or cells, with separate gas volumes. Each cell consists (Fig. 3.46) of a wire frame with alternating anode and field-shaping wires sandwiched between two cathode strip planes. Aluminized Mylar planes (ground planes) in between the cells shield the strips electrically and also separate the gas volumes of the different cells. Additional layers of thicker Mylar are added at the two ends of the package (end windows) to close and provide mechanical protection.

Wire planes

The basic chamber element is a circular frame on which alternating sense and field wires are strung as cords across the chamber in one plane. Each plane contains 96 sense and 97 field wires, with the two side wires being field ones. The length of the sense wires varies from 20 cm to 97 cm. The sense wires are 20 μm diameter gold-plated tungsten, while the field wires are

[41] Except for the size of the deadened area on the wires discussed later

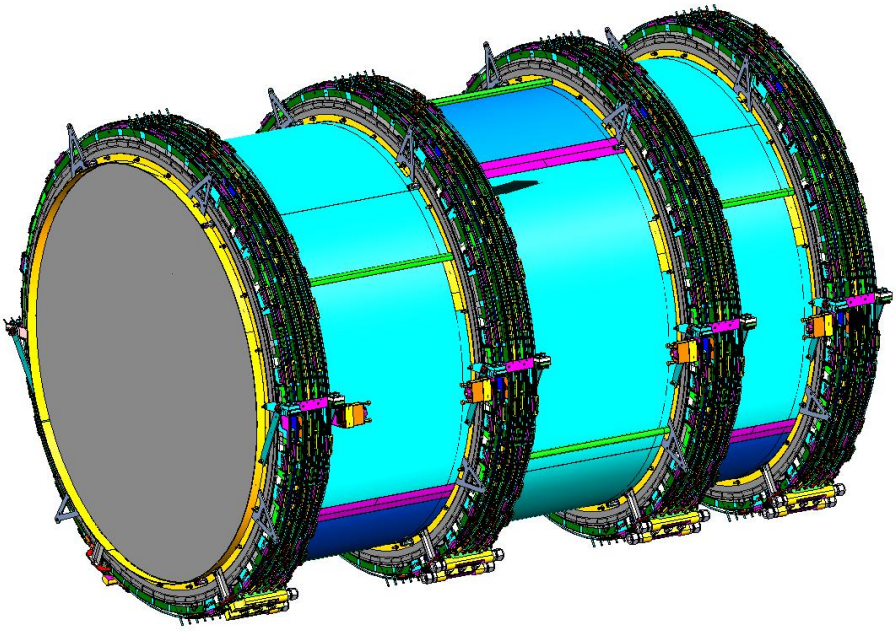

Figure 3.45: FDC detector: four tracking packages, each having six separate drift chambers (cells). The active area diameter is 97 cm with a total detector diameter of 120 cm, and total length of 174 cm.The positions of the second, third and fourth packages with respect to the first one are at: 58.43, 168.86, and 155.30 cm.

80 μm gold-plated copper-beryllium. The field-to-sense wire spacing is 5 mm and the distance to both cathodes is also 5 mm, resulting in a 10x10 mm^2 electric-field cell formed around the sense wires in a plane perpendicular to the wires. Positive HV is applied on the sense wires to achieve a gas gain of $\sim$5 10^4. Negative HV is applied on the field wires to improve the circular symmetry of the electric field in the cell (Fig. 3.47 right panel).

The frame containing the the sense and field wires is a 5 mm thick lamination (Fig. 3.48) consisting of three rings: a fiberglass (G10) ring, a Rohacell ring, and a printed circuit board (PCB) ring, with all three elements glued together [42]. The inner diameter of the frame is 100 cm with an outer diameter of 120 cm. To reduce the amount of the frame material, 80% of the fiberglass G10 ring thickness was milled from 4.14 mm down to 0.8 mm. The milled region was filled with sectors made out of Rohacell glued together [43] as a ring. The remaining 20% form a solid G10 ring that covers the holes for the mounting rods and mechanically supports the package assembly.

The PCB ring is formed by gluing [44] together six separate circuit boards. Two of the boards (4-layer PCB) are at the signal side of the wires, another two boards (2-layer PCB) are at the high voltage side of the wires, and the last two boards form the sides of the ring. As a first step, the G10 and Rohacell rings are glued together, after which the PCB ring is laminated to them.

The sense and field wires are strung between the high voltage and signal PCBs. First, the

[42] Using Hysol epoxy RE2039 resin and HD3561 hardener
[43] Using Scotchweld 1838 epoxy
[44] Scotchweld 1838 epoxy

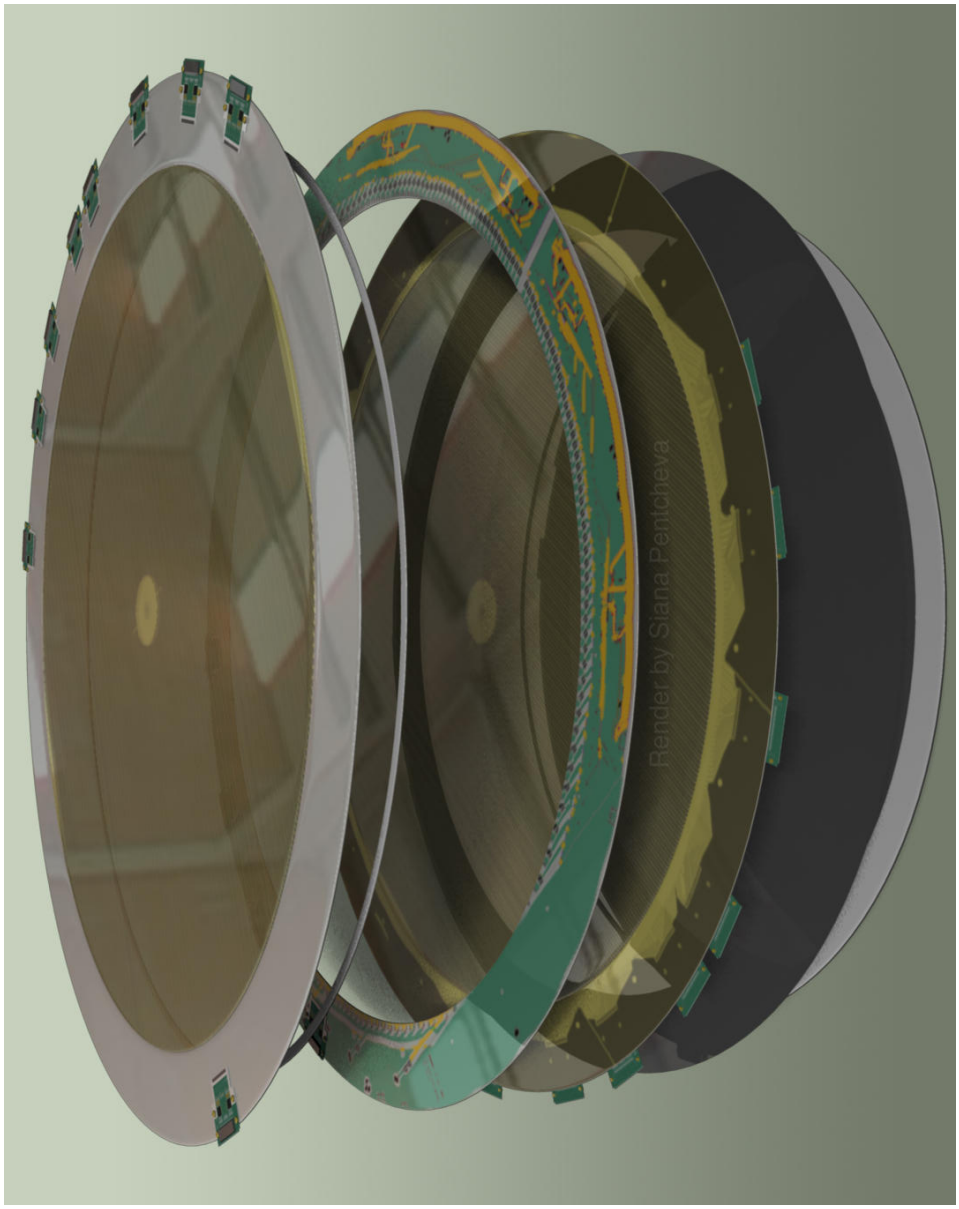

Figure 3.46: One detector cell (artistic view) from left to right: upstream cathode, spacer ring, wire plane, downstream cathode, ground plane (black disk) glued to the back of the downstream cathode, end window (gray) only at the end of the package.

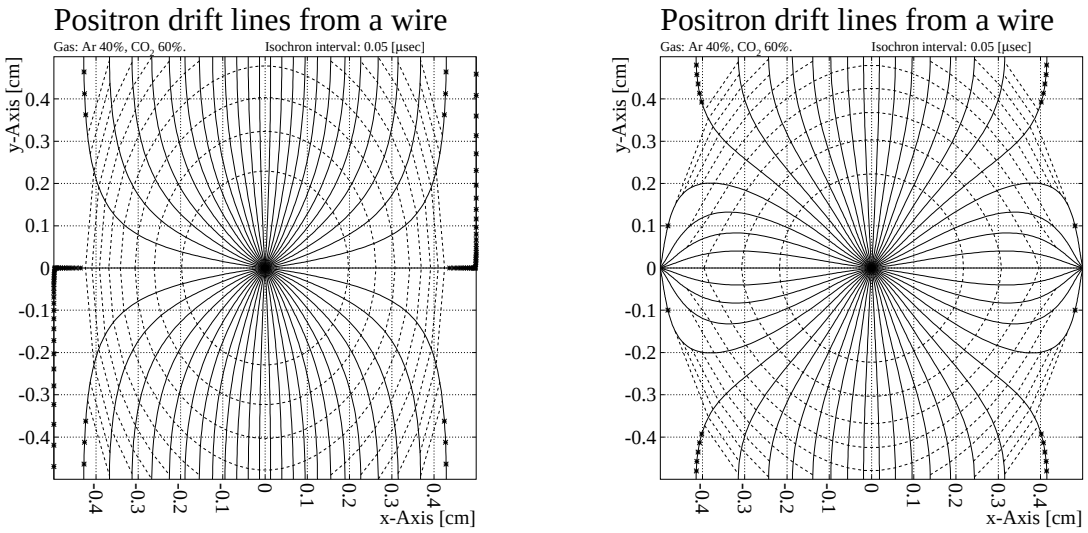

Figure 3.47: GARFIELD calculations of electric field lines (for a $B = -2.3$ T field configuration) within a square drift cell for a 40% argon - 60% CO_2 gas mixture for electrode configurations without (left) and with (right) field-shaping wires. The x-axis is perpendicular to the wires in the wire-plane, y-axis is along the beam line, with the sense wire at zero, and field wires at $\pm$ 5 mm.

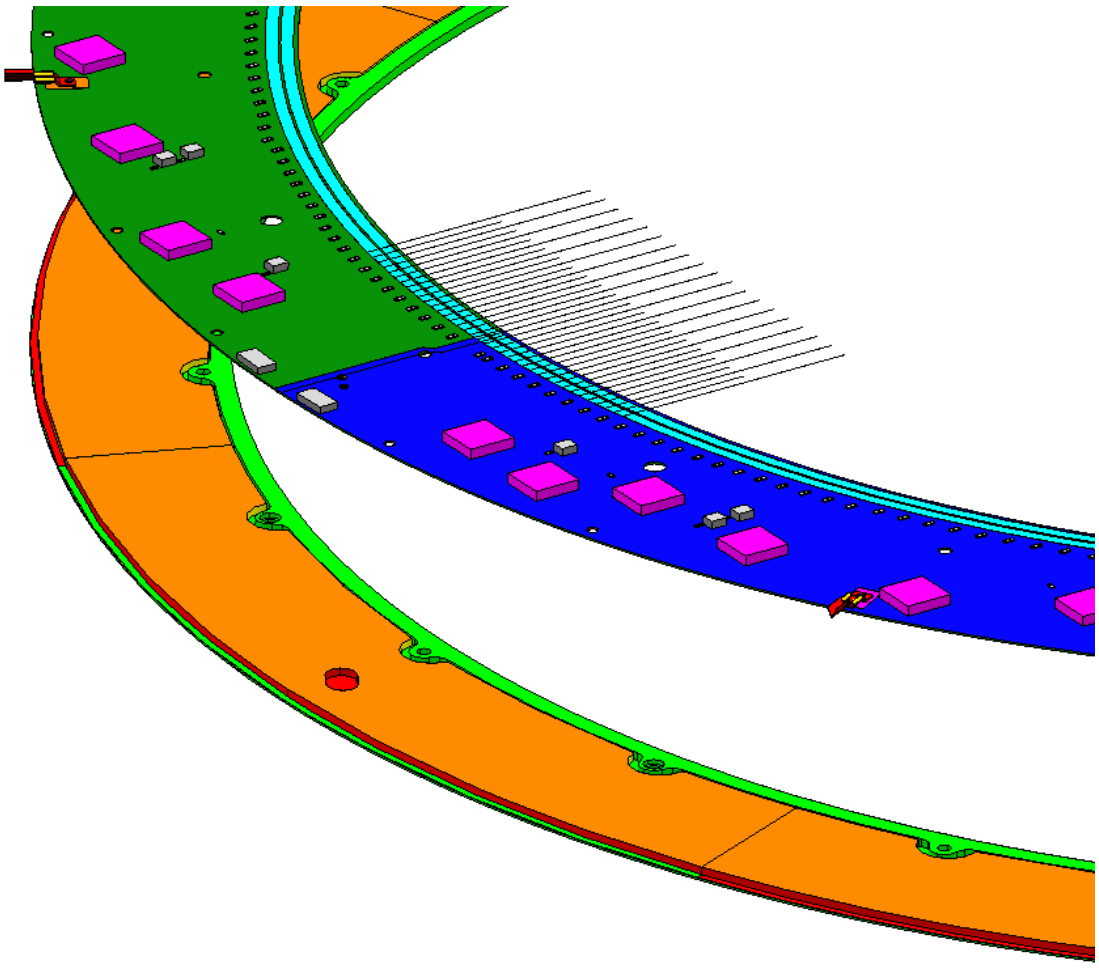

Figure 3.48: Wire frame lamination: PCB ring (top green and blue) with sense and field wires soldered on it (not all wires shown), Rohacell sectors (bottom orange with red sides), G10 frame (bottom green)

wire frame is mounted on a strong-back placed on a granite stringing table. Then the wires are strung above the frame between high precision pins attached with rails to the ends of the table. Next, the position of the strong-back (and the wire frame) is adjusted with respect the wires, and the frame is raised so that the wires are just touching the wire pads on the boards. At this position the wires are fixed to the boards by applying small adhesive Kapton dots. Then the wires are glued [45] and soldered [46] to the boards.

The wire positions are measured (and corrected if needed) using a stepper motor [47] attached to a worm gear with a sensor running across the wires. The positions are kept within 50 μm from the nominal value with a R.M.S. less than 25 μm. Tensions of 20 and 130 g (force) are applied on the sense and field wires respectively. They are checked using a permanent magnet placed close to the wire and applying variable current from a function generator, thus finding the main resonance frequency that is related to the tension. The measured tensions did not vary by more than 2 g for the sense and by 10 g for the field wires.

Each high voltage PCB is divided into two independent sectors supplying positive HV for 20 (inner) and 28 (outer) sense wires. Similarly, the negative HV supply is split in two on each board. In total, for each wire plane, there are 4 positive and 4 negative independent HV sectors connected to different channels on the HV supply.

The signal PCBs have HV capacitors separating the sense wires from the signal part of the board. The capacitors are positioned at the inner side of the PCBs, which is inside the gas volume. Due to improper soldering by the manufacturer that resulted in enhanced leakage currents, all the HV capacitors were replaced [48]. Each signal PCB has two connectors for the pre-amplifiers, each serving 24 sense wires; in total there are four connectors or 96 channels per wire plane. Protective resistors of 1 MΩ are installed on both HV and signal PCBs. These resistors limit the current on each sense and field wire to inhibit sparks.

Cathode strip planes

The cathode planes are copper coated Kapton foils stretched on G10 frames. The cathode G10 frame is similar in shape to the wire G10 frame. It has a thick ring covering the mounting holes and thin periphery on which the Kapton foil is glued [49]. Unlike the wire frames, there is no Rohacell material in the cathode frames. The Kapton foil thickness is 25 μm while the copper layer is only 2 μm to minimize the amount of the material in the active region.

Due to the large size of the cathode, one cathode foil is made out of three separate foils. The three pieces are first cut, aligned together, and then attached by gluing [50] thin (25 μ) Kapton tape over the non-copper side of the foils. Thus, the cathode foil is made as a circle with the copper layer forming the strips, grounds, traces and connectors. The foils, and therefore strips, are aligned with a precision better than 100 μm. The cathode foil is first glued to a transfer ring so that the surface tension can be set to 500 N/m, and then glued [51] to the cathode frame.

The optimum cathode readout pitch is determined by the width of the induced charge

[45] Epon Resin 828 and Versamid 140 hardener
[46] Almit Solder PN-KR19SHRMA Sn60-P2-0.3mm
[47] Parker S/SX 83-93 with ACR 9000 controller
[48] Using 220 nF AVX 1825JC102 rated for 4 kV except a few of the boards where AVX 1825HC102 rated for 3kV were used
[49] Using Hysol epoxy RE2039 resin and HD3561 hardener
[50] Using Hysol epoxy RE2039 resin and HD3561 hardener
[51] Using Hysol epoxy RE2039 resin and HD3561 hardener

distribution. It has been shown by several groups that minimal differential non-linearity is achieved when the cathode pitch is equal to the wire-cathode distance of 5 mm (e.g. [77]). This value is employed in the FDC design. Due to the higher rates, the central 24 strips are split in two halves. Thus, on one cathode there are 216 strips with lengths varying from 29 to 100 cm.

The strips have traces on one side leading to 24-channel connectors with the pads imprinted on the cathode. The strips are connected to the pre-amp cards with rigid-flex assemblies, each consisting of a flexible PCB (flex) and a daughter board on which the pre-amp is plugged. The flex part is needed to accommodate connection to the opposite side of the cathode frame (through an opening there) where there is space for the daughter boards to be installed. The soldering of the flex to the cathode is a delicate operation with some possibility of destroying the thin (2 μm) copper pads and thus the whole cathode. Therefore, the flexible sections are glued to the cathode pads using anisotropic conductive tape [52] that conducts only in the direction perpendicular to the surface. The tape is a head-bondable film with small (50 μm) silver-covered glass balls distributed randomly. After the tape is placed between the two contact areas, a specially designed tool is used, along with pressure and heat to make the bond between the contacts.

To investigate this new technology, samples were made and tested at significant temperature changes and irradiated up to 1 kRad (expected dose to be accumulated at this place of the detector in the hall for 10 years). During the cathode production it turned out that some of the channels may have a resistance on the contacts that varies from few Ohms to several tens of Ohms, depending on the pressure applied and deformation at the contact area. The tests show that this is not aging but a mechanical problem related to frame deformations when handling of the cathodes. To mitigate the problem, special tools were designed to keep the cathodes flat in all the operations after the cards are glued.

In addition to the type-1 cathode described above, there are two other types of cathodes that are described in the next subsection.

Package design

The chamber elements described above are installed in the package forming six separate cells. In addition at the two sides of the package there are end windows: 2 mil aluminized Mylar stretched on G10 frames similar to those for the cathodes. The ground planes (0.5 mil aluminized Mylar) that separate the cells are part of the type-2 cathodes, a modification of the described above type-1 cathode, on the back side of which, 5 mm apart from the cathode foil, a 0.5 mil aluminzied Mylar foil is stretched and glued to the frame. All the cells have the same structure except the outer cathodes of the two outer cells. These are type-3 cathodes, a modification of the type-2 cathode with holes punched through the ground plane. In this way, the end windows accommodate the pressure difference between chamber and atmosphere.

Thus, starting from the upstream side, the package consists of:

- Upstream end window,
- cell #1 with type-3 cathode, spacer ring, wire frame, type-2 cathode
- cell #2 with type-1 cathode, spacer ring, wire frame, type-2 cathode
- ... same for cells #3, #4, and #5

[52] 3M Anisotropic Conductive Film Adhesive 7303 (5 mm width)

- cell #6 with type-1 cathode, spacer ring, wire frame, type-3 cathode
- Downstream end window

In each cell, the strips of the top and bottom cathode are oriented with respect to the wires at 75° and 105° respectively. Neighboring cells are rotated by 60° with respect to each other in order to improve track reconstruction on the corresponding anode wire left/right ambiguities, hence improving the overall resolution.

Each cell forms a gas volume (Fig. 3.49) separated from the neighboring cells by the ground planes. There are gas holes at the periphery of all cathode planes to equalize the pressure on both sides and keep the cathode foil flat. The gas containment of the package is achieved by Viton O-rings [53] installed in between all the chamber elements. There are O-ring grooves on one side of the the wire frames, type-1 cathodes and end-windows, and on both sides of the spacer rings. While testing the first production package it was found that there is significant oxygen contamination, up to few percent, inside the gas volume. It turned out that the oxygen penetrates between the O-rings and grooves especially on the G10 frames due to the fiber structure of the machined grooves. Therefore, the wire and cathode grooves are coated with epoxy [54]. In addition, vacuum grease [55] is applied on all the O-rings. Thanks to this, the oxygen contamination in a package is reduced down to a negligible level of less than 100 ppm.

At the same time, it was found that the combination of Viton O-ring and vacuum grease prevents the appearance of corrosion on the copper layer of the cathodes that faces the O-rings. Significant damage of the thin copper layer, especially at the traces leading to the connectors, was found on the first packages where EPDM O-rings were used, which required their refurbishment.

Two aluminum gusset rings (L-shape profile) at both sides of the package connected with 24 aluminum threaded rods through holes in all the package planes are used to compress the O-rings and hold the package elements together. Cuts are made in the gusset rings and then connected with carbon fibers to avoid closed loops inside the magnet.

The total thickness in the active area of each package in terms of radiation length is estimated to be $\sim$0.43 $\%X_0$ (Table 3.23), where X_0 is one radiation length. Most of it comes from the cathode materials, dominated by the 2μm copper layer and then from the Kapton itself.

Central chamber region

The region of the chamber close to the beam line requires special treatment. First, the material along the beam should be minimized to reduce the additional background production. There is no copper on the cathodes in the area around the beam line within 2.4 cm diameter. This reduces the material along the beam line to 0.26 $\%X_0$ per package (from Table 3.23), or 1.04 $\%X_0$ in total, to be compared to 3.5 $\%X_0$ thickness of the LH target.

Second, the detector itself should be insensitive near the beam line so that the rates on the electronic channels are reduced to a manageable level. The rates on the FDC have been studied by Monte Carlo simulations of the electromagnetic background [**?**]. A safe limit of $\sim$130 kHz was assumed for all the electronics channels. This requires insensitive areas with diameters 5.8

[53] Viton 55 durometer
[54] Hysol epoxy RE2039 resin and HD3561 hardener
[55] Apiezon-L

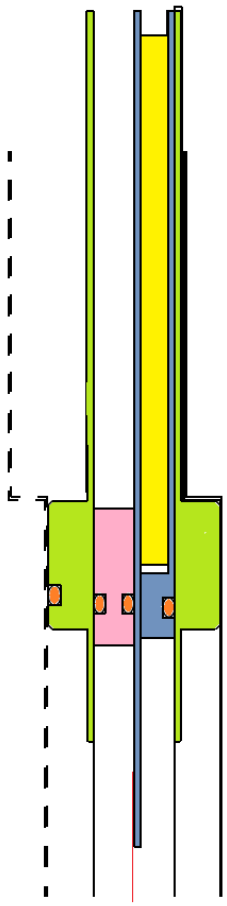

Figure 3.49: Cross-section showing separation of the different frames within one chamber cell. Top corresponds to the outer side of the detector, the gas volume is at the bottom side. From right to left: cathode type-2 (green frame) with ground and cathode foils on it (black lines), wire plane (blue frame with yellow Rohacell) with wires (red line), spacer ring (pink), cathode type-1 with cathode foil (black line), cathode type-2 from the next cell which ground foil and frame are shown with dashed line. The orange regions indicate the O-rings.

Material (description)	Thickness μm	Quantity	Total cm	X_0 cm	Fraction of X_0 %
Kapton (on all cathodes)	25	12	0.030	28.60	0.105
Copper (on Kapton)	2	12	0.0024	1.43	0.168
Mylar (on type-2,3 cathodes)	13	7	0.009	28.7	0.031
Aluminum (on type-2,3 cathodes)	< 0.1	7	< 0.00007	8.9	< 0.0008
Mylar (on end-windows)	50	2	0.010	28.7	0.035
Aluminum (on end-windows)	< 0.1	2	< 0.00002	8.9	< 0.0002
Argon (gas mixture)	13cm $\times$ 40%	1	5.2	10944	0.047
CO_2 (gas mixture)	13cm $\times$ 60%	1	7.8	18310	0.043
Total					0.430

Table 3.23: FDC material in the active area for one package

cm, 6 cm, 6.1 cm, and 7.8 cm respectively for the first, second, third, and fourth packages. To have two pairs of interchangeable packages it was decided the insensitive region of the first two packages to be 6 cm and for the last two packages 7.8 cm in diameter about the beam line.

An electroplating technique with copper sulfate solution was used to thicken the sense wires (Fig. 3.50) from 20 μm to $\sim$80 μm, making the chamber insensitive in that region near the beam line. The procedure consists of several plating cycles intervened with polishing cycles

Figure 3.50: Wire deadening: a container filled with $CuSO_4$ is raised against the wires; voltage is applied between the sense wires and a copper electrode inside the container.

in which the polarity is reversed. The current on the electrodes and the timing of the cycles

were optimized to obtain a smooth surface. A micro-controller system was developed [**?**] to control the electroplating procedure. After the procedure, the wires were cleaned with water and alcohol.

Package subsystems

- Gas system.

  The six cells of the package are supplied with gas in parallel with manifolds at the supply and exhaust side. The gas enters the cell volume through nine 1 mm holes in the spacer ring of the cell (supply side) and exits the volume in the same way at the opposite side of the ring (exhaust side). In addition there is a hole in the spacer ring connected to an individual gas line that is used to monitor the internal pressure of each cell separately. We assume a nominal gas flow through one package of 250 sccpm (standard cubic centimeters per minute) and a pressure in each cell of $\sim$ 100 Pa above atmospheric pressure..

- Grounding.

  To minimize the noise, the grounds of the wire and cathode planes are connected at many places at the periphery of the package. There are 16 connections per cell that bridge the grounds of the downstream cathode, wire frame, upstream cathode, and the downstream cathode of the next cell. The connections are done with 4 mil copper strips 1 cm wide pressed against the ground areas with clips. There are 16 additional connections per cell that bridge the elements of one cell on both sides (where possible) of the cathode readout cards. This is needed to ground the cards as close as possible to them. At the same time this provides mechanical strength of the cathode frame at the places where the cards are installed, thus avoiding deformation of the conductive tape contacts. In total there are about 200 such ground connections per package.

- Cooling system.

  The power dissipated by the pre-amplifier cards of one package is expected to be $\sim$200 W and therefore cooling is needed. Fluorinert [56] is used as coolant which compared to water, will avoid fatal damages of the detector and the electronics in case of leakage. Six copper tubes (one per cell) of 4 mm outer diameter and 0.6 mm wall thickness, are shaped as circles and installed around the package using brackets attached to the pre-amplifier cards. There are two plastic manifolds at the input (each serving three cells) and two at the output of the tubes connected to the Fluorinert supply. Care has been taken to avoid closed conductive loops. A nominal gauge pressure of 37 psi at the input and 4 psi at the output will allow temperature variations over the cooling loops to be less than 3^0 C.

- HV connections.

  All the positive high voltage (HV) sectors of one package are connected to a Radial 52-pin connector mounted at one of the package holding brackets with wires running to the upstream side of the package. Each individual channel has connectors at the upstream side of the package which simplifies the package assembly and allows for additional testing of each HV sector. The wiring of the negative HV sectors is analogous. The wires are running to the downstream side and a 52-pin connector is attached to the other holding

[56] FC-770 by 3M

bracket. Two HV cables coming from CAEN A1550P/N HV units are connected to one package serving the 24 positive/negative HV channels of the package.

- LV connections.

  The low voltage (LV) of 3 V needed for the pre-amplifier cards (each drawing ∼0.5A) is distributed with 18 m long cables, each supplying four cards in parallel. In addition, the same cables are used to distribute the threshold voltage to the wire discriminator cards. Due to the space limitation for the LV connectors the thickness of the wires is limited such that a voltage drop along the cables is about ∼3 V. This increases the power dissipated inside the magnet by about 20%. Three types of cables are used that differ by the number of connectors (2 for the wire planes and 4 for the cathodes), and the distances between the connectors.

- Signal cabling.

  132 signal cables are connected to the pre-amps of one package. To reduce the stress on the connectors, the cables are tightened to the gusset rings and the package spacers. The cables are shielded with copper braid and thin aluminum tape, but the braid is removed for the part of the cables that are inside the magnet. The cables are subdivided into four quadrants and bundled together outside of the magnet.

- Fiducialization.

  Four prism reflectors are attached to the gusset rings of each package. Even when the detector is cabled and installed in the bore of the magnet, they can be surveyed from the downstream side in direction parallel to beam line with a precision of 0.1 mm.. Additional spherical targets have been attached to the gusset rings of each package during the initil detetctor survey.

Readout Electronics

Two types of pre-amplifier cards are mounted on the chambers. One is for the strip readout which is a charge-sensitive preamplifier with pulse-shaping. It has a gain of 2.6 mV/fC, 130 fC dynamic range and 14 ns peaking time. The other type, used to read the sense wires, has a 0.77 mV/fC pre-amplifier with 260 fC dynamic range and in addition - a built-in discriminator that outputs LVDS signals. Both cards use GAS-II ASIC and have resistors that define the different settings.

The FDC readout will employ 100 *ps* F1 TDCs for the anode wire drift time readout and 125 MHz FADCs for the cathode readout. This enables commonality with the readout electronics of the other GlueX detector subsystems. Note that with a clock rate of 125 MHz on the FADCs, time fitting algorithms matched to the chamber pulse shape can be employed to provide a time resolution of ∼2 ns This timing information from the cathode signals would aid in pattern recognition of multiple tracks passing through the chamber volume.

Gas Considerations

There are several basic requirements that need to be met by the chamber gas that will be used for the FDC system. These include a high drift velocity (50-60 μm/ns), low Lorentz angle ($< 10^{\circ}$), and for safety, a non-flammable mixture. It is important to understand that the performance

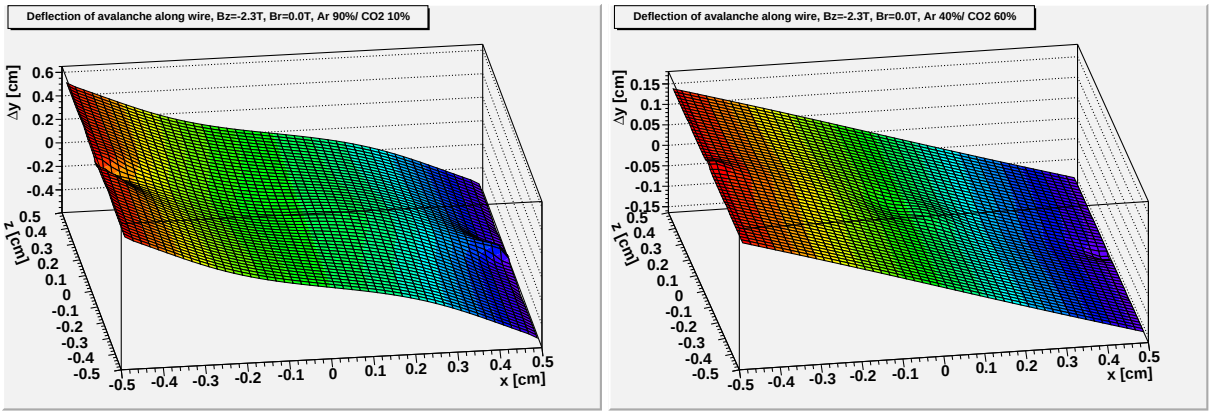

Figure 3.51: Results of GARFIELD calculations for the deflection of the avalanche position (relative to the B=0 case) as a function of the position of the ionization within the cell for two different gas mixtures: 90% Ar / 10% CO_2 (left) and 40%Ar / 60% CO_2 (right). The high voltage settings were S=+1550 V, F=-200 V, and S=+2200 V, F=-500 V, respectively.

of a cathode chamber in terms of cathode position resolution is reasonably insensitive to the exact values of the gas parameters. Here variations of the drift velocity or non-uniform drift velocities as a function of E/p (i.e. electric field/pressure) are relatively unimportant. For the same reason, the cathode readout operation is immune to modest variations of temperature and pressure. Variations in gas gain on the order of 20% do not strongly affect the cathode resolution since a relative charge measurement in adjacent strips is involved.

However, the gas mixture and its control are essential for the operation of the MWDC. In order to enable accurate calibrations of the drift times, it is essential that the gas mixture is stable, which amounts to constructing a gas handling system that carefully controls the gas mixture, as well as hall-controls to fix the temperature and relative humidity as much as possible.

For the electric field configurations under consideration, increasing the percentage of argon, within a mixture of argon/CO_2, results in greater deflection of the avalanche position along the wire. Figure 3.51 compares the deflection along the wire as a function of the position of the ionization within a drift cell for a 90%/10% Ar/CO_2 mixture, and a 40%/60% mixture. We have opted for the 40% Ar/ 60% $C0_2$ mixture. At the highest magnetic field we expect to see in the chambers, the 40% Ar/ 60% $C0_2$ mixture has a maximum deflection of about one quarter of that for a 90%/10% Ar/CO_2 mixture. Figure 3.47 shows the field lines for two possible wire configurations (with and without field-shaping wires). The drift-to-time relationship for the 40%/60% mixture is shown in Figure 3.52. The presence of a non-zero magnetic field lengthens the minimum drift time for ionizations occurring near the field wires by a small amount relative to the B=0 case.

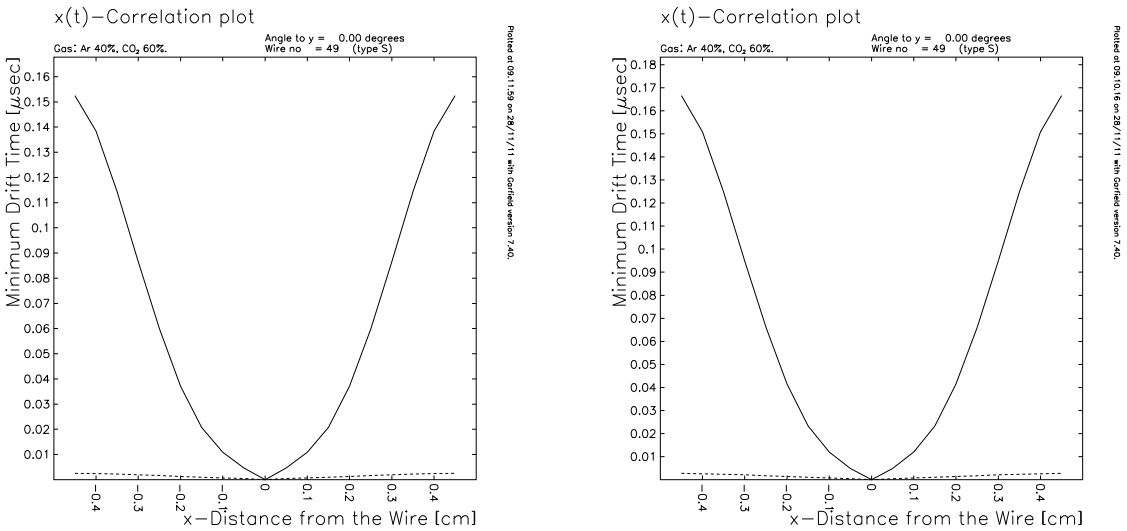

Figure 3.52: Relationship between drift time and distance for B=0 (left) and B=-2.3 T (right) from a GARFIELD calculation for an FDC cell.

3.7 Time of Flight

3.7.1 TOF Summary [57]

The main parameters and properties of the TOF are given in Tables 3.24 and 3.25. The assembly drawing for the TOF is D000000105-0000.

Table 3.24: TOF properties.

Item	Value
Scintillator Type	Eljen EJ-200
Scintillator Dimensions (cm^3)	
standard	$2.54 \times 6.0 \times 252$
half-width	$2.54 \times 3.0 \times 252$
half-length	$2.54 \times 6.0 \times 120$
Read-Out Channels per Module	
standard	2
half-width	2
half-length	1
Light Guide Material	UVT PMMA
Light Guide Length (standard module)	approx. 30 cm
Wrapping Material Thickness (mils)	
inside: 3M ESR Daylighting Film	2
outside: Tedlar	1
Module count	
standard	2×38
half-width	2×4
half-length	2×4
total	92
Layers	2
Mean-Time Resolution (one standard module, rms)	90-95 ps
PMT operating voltage	approx. 1750 V

Table 3.25: TOF instrumentation.

Device	Description	Quantity
Photomultiplier Tube	Hamamatsu H10534MOD	176
Splitter	JLab 50/50 splitter, 48 ch	4
Flash ADCs	JLab fADC250-MHz, 16 ch	11
Discriminator	JLab LE Discriminator, 16 ch	11
TDCs	CAEN 1290A TDC, 32 ch	6
HV for PMTs	CAEN A1535SN, 24 ch	8

[57] *SVN revision ID:* tdr_summary_tof.tex 13854 2014-06-12 04:42:15Z gen

3.8 Start Counter

3.8.1 Start Counter Summary [58]

The main parameters and properties of the ST are given in Tables 3.26 and 3.27. The drawings for the ST can be found at D000000101-0001.

Table 3.26: ST properties.

Item	Value
number of counters	30
scintillator material	Eljen EJ-200
scintillator thickness	3 mm
length of barrel straight section	39.5 cm
length of nose straight section	16.2 cm
radius of curvature of bend section	12.0 cm
total angle of bend	18.5 degrees
inner width of the counter	16.29 mm
aluminum wrapping	16.5 μm
distance from Z-axis to the counter	77.5 mm
inner Rohacell shell ID/OD	133.3 mm / 152.1 mm
Time resolution, σ	0.35 ns
Thickness including structure (rad.len.)	1.2%

Table 3.27: ST read-out instrumentation

Item	Description	Quantity
photodetector	Hamamatsu MPPC, S10931-50P	4×30
discriminator	JLab LE discriminator, 16 ch	2
TDC	JLab F1TDC V2 60 ps, 32 ch	1
Flash ADC	JLab fADC250-MHz, 16 ch	2
MPPC Bias supply	ISEG EHS 201P-F-K, 16 ch, 10mA for 4 MPPC/ch	2
LV power	MPOD MPV8008, 8 ch, 5 A/ ch	1

[58] *SVN revision ID:* tdr_summary_st.tex 13854 2014-06-12 04:42:15Z gen

3.8.2 Start Counter Overview

The purpose of the GlueX Start Counter will be, in coincidence with the tagger, to identify the electron beam bucket associated with the detected particles resulting from 9 GeV linearly polarized photons incident on a liquid H_2 target. It is designed to operate at tagged photon intensities of up to $10^8\,\gamma/s$ and will provide a fast signal which is used in the level–1 trigger of the experiment. Furthermore the Start Counter detector will proved excellent solid angle coverage, $\sim 90\%$ of 4πhermicity, and a high degree of segmentation for background rejection. EJ-200 scintillator material manufactured by Eljen Technology, which provides a decay time on the order of 2 ns and a long attenuation length, will be used in order to properly identify the beam buckets which are about 2 ns apart. The detector consists of a cylindrical array of 30 scintillators with *pointed* ends that bend towards the beam at the downstream end. The support structure will be kept at an absolute minimum in the active region of the detector, and is to be made up of Rohacell and carbon fiber. Silicon PhotoMultiplier (SiPM) detectors have been selected as the readout system. These detectors are not affected by the high magnetic field produced by the GlueX superconducting solenoid magnet. Moreover, the SiPMs will be placed as close as possible (< 1 mm) to the upstream end of each scintillator element, thereby minimizing the loss of scintillation light.

3.8.3 Paddle Geometry

Each individual paddle of the Start Counter is machined from a long, thin, plastic (polyvinyl toluene) EJ-200 scintillator bar that is initially manufactured by Eljen Technology to be 600 mm in length, 3 mm thick, and 20 ± 2 mm wide. Eljen Technology bends each scintillator around a higly polished aluminum drum by applying localized infrared heating to the bend region. The bent scintillator bars are then sent to McNeal Enterprises, a plastic fabrication company, where they are machined to the following desired geometry (see figure 3.53). The paddles are designed to consist of three sections, described from the upstream to the downstream end of the target. First is the straight section, that runs parallel to the target chamber, is 394.65 mm in length. Second is the bend region which consists of a 18.5° arc of radius 120 cm which is downstream of the straight section. Third is the tapered region, which is downstream of the target chamber, that bends towards the beam line and ends at a height of 20 mm above the beam line. After the straight bar is bent to the desired geometry, the two flat surfaces that are oriented orthogonal to the wide, top and bottom surfaces, are cut at a 6° angle. During this process the width of the top and bottom surfaces are machined to be 16.92 mm and 16.29 mm wide respectively. Each of the 30 paddles may be rotated 12° with respect to the paddle that preceded it so that they form a cylindrical shape with a conical end (See figure 2). The geometry of the Start Counter increases solid angle coverage while minimizing multiple scattering. The complete assembly is designed to have a diameter of ~ 155 mm at the upstream end and a diameter of 40 mm at the downstream end of the target(see figure 3.54).

3.8.4 Support Structure

The 30 scintillator paddles will be placed atop a Rohacell support structure which envelopes the vacuum chamber. Rohacell is a rigid, low density foam ($\rho = 0.075\,\mathrm{g/cm^3}$). The Rohacell, which is 11 mm thick, will be rigidly attached to the chassis and will extend down the length of paddles however, not to include the end of the conical section (see figure 3.55). Glued to the

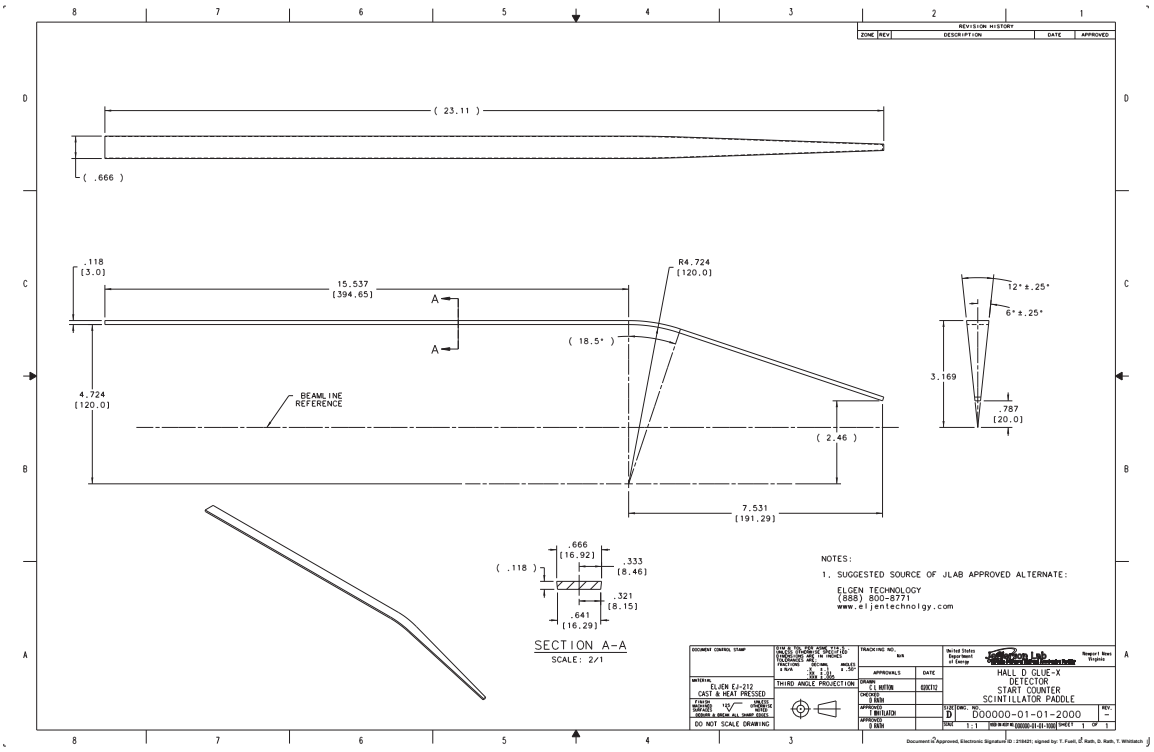

Figure 3.53: The geometry of a single Start Counter paddle.

inner diameter of the Rohacell support structure is 3 layers of carbon fiber ($\rho = 1.523\,\mathrm{g/cm^3}$) which each are 650 μm thick (see figure 3.56). The carbon fiber serves to provide additional support during the assembly process. The SiPM detectors are held in a fixed position while being attached to the lip of the chassis *via* two bolts. The scintillators will be placed as close as possible, without directly touching surfaces, to the active region of the SiPMs.

SiPM Detectors & Electronics

The Start Counter (ST) will have its scintillators coupled, *via* an air gap (< 1 mm), to groups of four SiPMs set in a circular arrangement. The individual SiPMs are single-cell SiPMs (Hamamatsu MPPC, S10931-50P) with a $3 \times 3\,\mathrm{mm^2}$ active area. Four individual SiPMs, grouped together in a linear array (see figure 3.57), will be arranged such that they are parallel to the end of the upstream end of the scintillator. Four SiPMs, reading out one individual paddle, are to be current summed prior to pre-amplification. The output of each preamp is then split, buffered for the Analog to Digital Converter (ADC) output, and amplified for the Time to Digital Converter (TDC) output. The ADC outputs will be readout *via* of two 16 channel flash ADCs (JLab 250 MHz Flash, fADC250), while the TDC outputs will be applied to two 16 channel leading edge discriminators (JLab LE discriminators), followed by a 32 channel flash TDC (TDC JLab F1-TDC). Furthermore, each group of four SiPMs utilizes a thermocouple for temperature monitoring. There are 120 SiPMs in total, for a total of 30 pre-amplifier channels (see figure 3.58). After many tests, it was found that there was no substantial difference be-

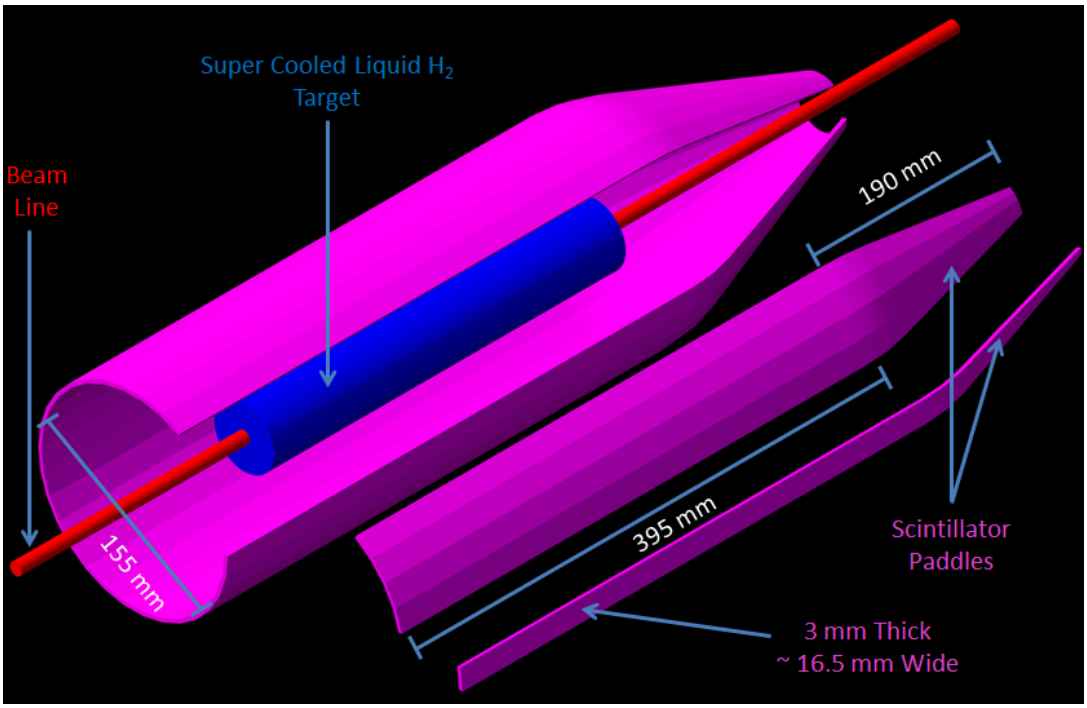

Figure 3.54: Start Counter with pieces removed revealing the target and beam line.

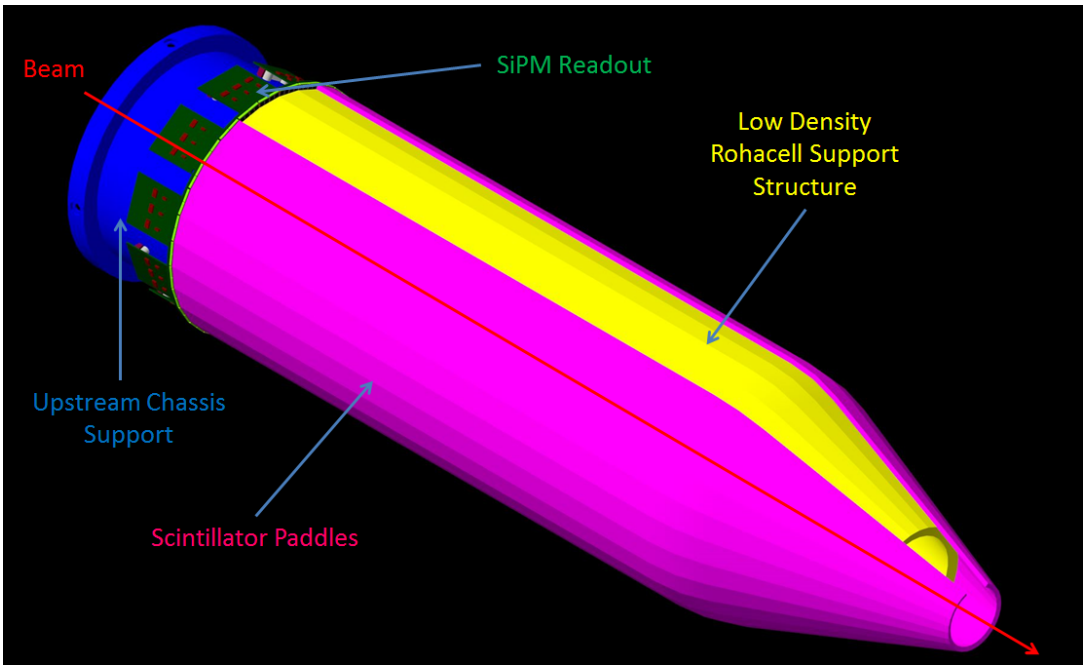

Figure 3.55: Partially assembled Start Counter.

tween the time resolution achieved with the SiPM design and with a traditional PMT. Because of studies that indicated light loss through the use of light guides coupled to PMTs, and the

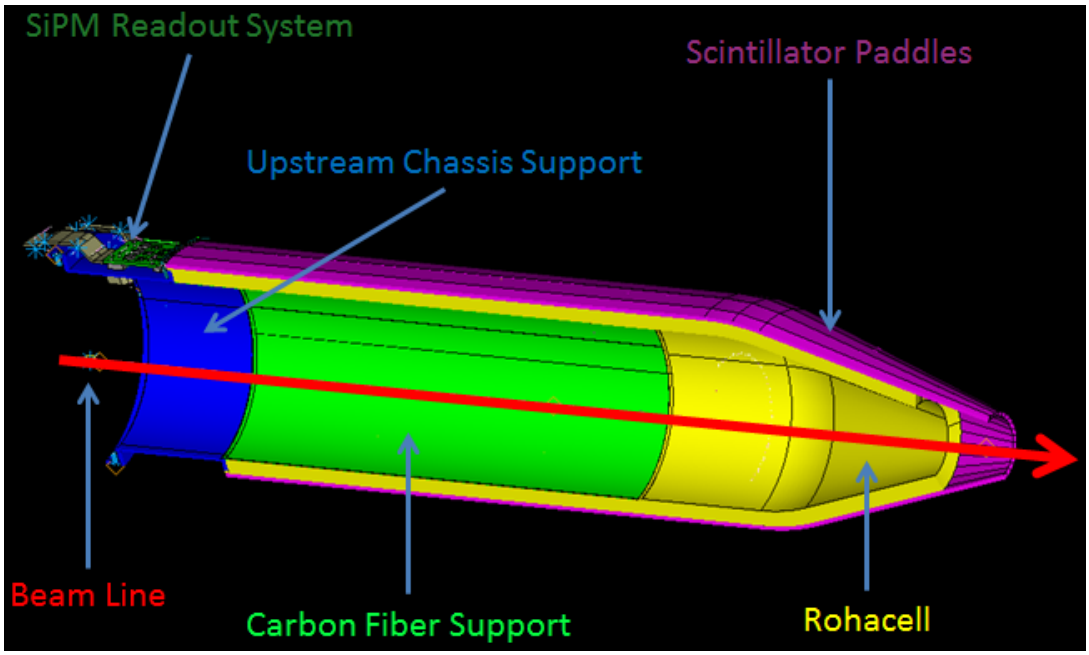

Figure 3.56: Cross sectional view of the fully constructed Start Counter.

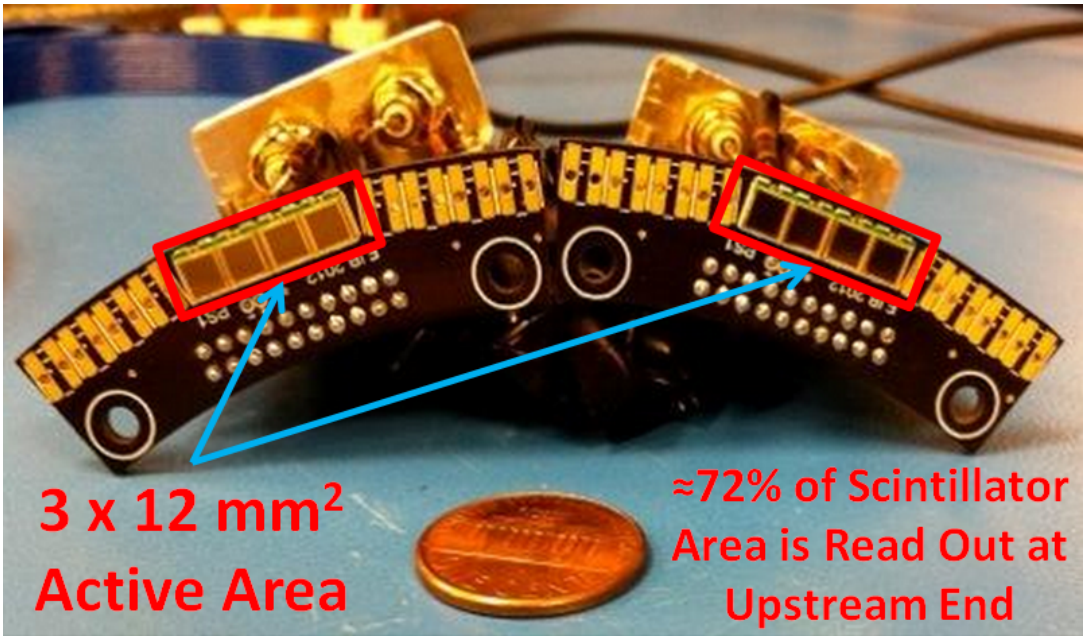

Figure 3.57: Two ST1s of the SiPM readout system placed side by side. The two holes at the bottom of ST1s PCB is the point of attachment for the SiPMs to the upstream chassis support. The SiPMs will be connected to the chassis *via* two pairs of nuts and bolts.

advantage of the magnetic field-insensitivity properties of SiPMs, it was decided that the SiPM design would be the most suitable readout system for the GlueX Start Counter. There are

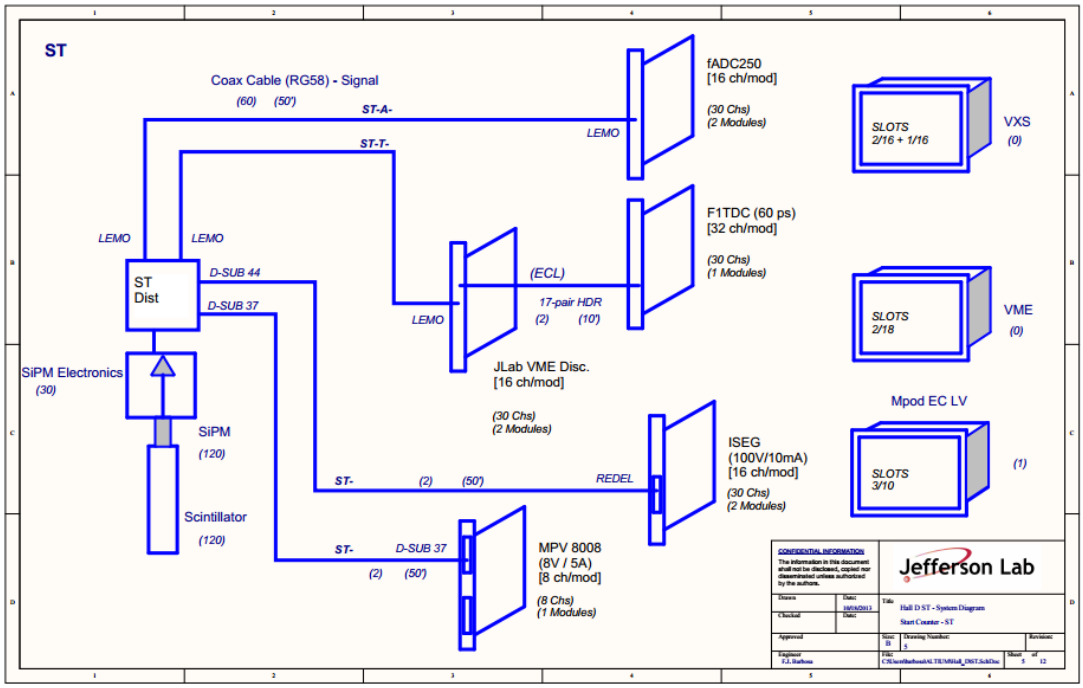

Figure 3.58: Start Counter electronics diagram.

three components that comprise the SiPM detector and readout system. The first component is the ST1 which holds 3 groups of 4 SiPMs ($3 \times 12\,\mathrm{mm}^2$ active area). The SiPMs are housed in a ceramic case, while being rigidly attached to the ST1. In order to mimic the geometry of the 30 paddle design, one group (of four SiPM's) is offset by 12° relative to the central group, while another group is offset by −12°. One ST1 unit will collect light from three paddles individually. The ST1 implements the current sum and bias distribution per group of 4 SiPMs. It also has thermocouple for temperature monitoring. The second component is the ST2 which is a Printed Circuit Board (PCB) that houses the electronics of the readout system. It has 3 channels of pre-amplifiers, 3 buffers (for the ADC channels), and 3 factor five amplifiers (for the TDC channels). Furthermore, it has 3 bias distribution channels with individual temperature compensation *via* thermistors. The ST2 is attached to the ST1 *via* 90° hermaphroditic connector. The third component, the ST3, provides interface to the power and bias supplies. It also routes the 3 ADC, and 3 TDC outputs as well as the thermocouple output. The ST3 connects to the ST2 *via* a signal cable assembly (see figure 3.59). The ST3 will be installed in the upstream chassis upstream of the Start Counter and next to the beam pipe.

3.8.5 Measurements

Many data have been collected regarding long thin scintillator bars, of different dimensions, and varying scintillator materials. Data was also taken to study the different responses of various PMTs and SiPMs coupled to scintillator bars. These data consist of measurements for both straight bars as they were received from Eljen Technology, and bars that have been machined to the specific geometry of a GlueX Start Counter paddle. The data proved that the optimal dimensions of the pre-machined paddles were to be $600 \times 3 \times (20 \pm 2)\,\mathrm{mm}^3$. Moreover, it was

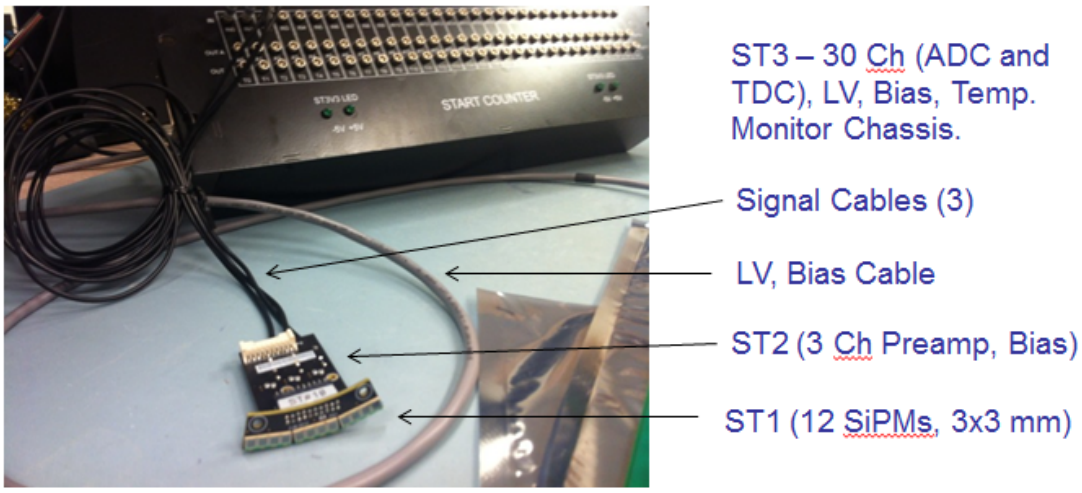

Figure 3.59: Complete Start Counter readout system.

determined that the aforementioned SiPM and readout system would be suitable for our needs. In addition, studies showed McNeal Enterprises provided better quality machined scintillators than the competing plastics companies, *e.g.* Plastic Craft. While many tests of machined scintillators utilized the EJ-212 scintillator material, manufacturing requirements from Eljen Technology stipulated a change to the EJ-200 scintillator material. Further tests showed that there is no substantial difference between the two types of scintillator material.

Experimental Set-up for Testing Scintillators

In order to test individual paddles, a radioactive Strontium-90 (^{90}Sr) source was placed at fixed distances along the path of the scintillator. ^{90}Sr undergoes β^- decay to ^{90}Y (yttrium). In turn, ^{90}Y undergoes β^- decay to ^{90}Zr (zirconium). The resulting decay of ^{90}Sr provides a continuum of electron energies from $\sim$ 0.5 MeV to 2.2 MeV which closely mimics the energy of minimum ionizing particles. The scintillation light is produced in the scintillator by the electrons traversing through the scintillator material. The subsequent photons are then detected using a SiPM that is coupled to the upstream end of the scintillator. A trigger PMT coupled to a scintillator is employed to provide timing information. The signals from the two detectors are then processed through various Nuclear Instrumentation Modules (NIMs) and Computer Aided Measurement And Control (CAMAC) modules. These signals are processed through a Data AcQuisition (DAQ) system and software where the ADC and TDC data are stored in ROOT files for analysis. The resulting spectra are fit with Gaussian distributions and the fit data are stored in data files. These data are then analyzed utilizing custom computer programs to illustrate the scintillator properties, *e.g.* L_{attn}, and σ_{tr}

Results

Five scintillator bar prototypes machined to the finalized geometry were tested extensively upon arrival (06/2013) at FIU. The aforementioned testing procedure was implemented in an identical manner for all five of the scintillators. Figure 3.60 shows the typical behavior that is observed when measuring the various time resolutions as a function of source distance for

scintillator paddles which are machined the unique Start Counter geometry. The red vertical line indicates the end of the straight section and the beginning of the bend/nose region. It is clear that the time resolution increases linearly in the straight section (0 - 39.5 cm), as one expects, while we observe the worst time resolution, *i.e.* least amount of light, in the bend region (39.5 - 43.3 cm), see figures 3.60 & 3.61. An interesting phenomenon occurs in the nose

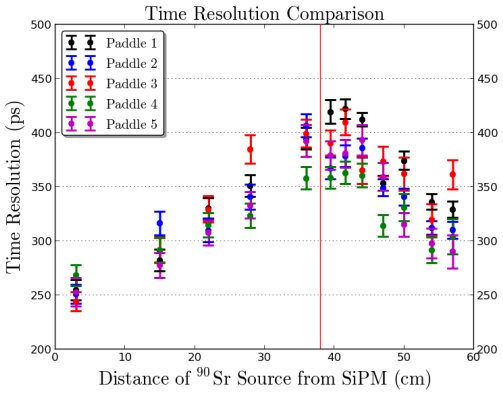

Figure 3.60: Time resolution.

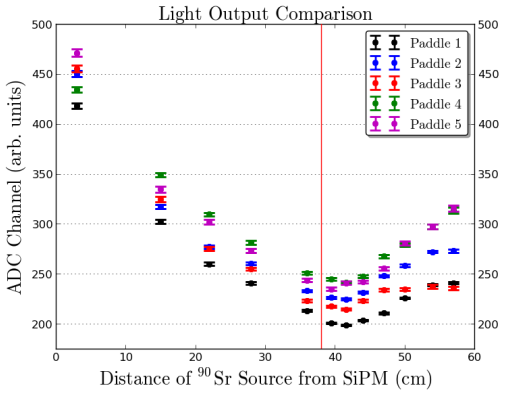

Figure 3.61: Light output.

region (43.3 - 59.5 cm) downstream of the bend. The time resolution begins to decrease, *i.e.* improve, as the source moves downstream of the SiPM. This effect was studied extensively *via* GEANT4 simulations, and the same result was observed. Thus, it is clear that this effect is purely a consequence of the unique geometry of the nose section. Upon comparing figures 3.60 & 3.61 it is clear that time resolution is clearly dominated by light output. This effect is advantageous for our purposes as the majority of the charged particles produced in GlueX will be forward going, *i.e.* small θ_{lab} values. Based on the data and simulations, the Start Counter will be able to provide a $\sigma_{tr} < 350$ ps and be able to successfully identify the electron beam buckets to within 99 % accuracy.

Wrapping of Scintillators

In order to increase the amount of light collected at the scintillator-detector interface, it is common practice to wrap plastic scintillators with reflective materials. Both 2 μm thick aluminized Mylar and 16.5 μm thick food grade aluminum foil were investigated extensively as potential wrapping materials for individual scintillator paddles (see figure 3.62). It should be noted that the bar that was tested in this study is a prototype manufactured prior to the batch of five paddles that was discussed previously. The time resolution achieved with this bar (labelled Bar 3) was worse than what was achieved with the batch of five prototypes. To ensure light tightness in the event of microscopic holes in the reflective wrapping material, it is advantageous to wrap the scintillator, in addition to the reflective material, with black Tedlar film. Figure 3.63 illustrates the effect of wrapping a machined bar with 2μm aluminized Mylar and food grade aluminum foil, as well as black Tedlar Film. As can be seen in figures 3.62 & 3.63 the data indicates that wrapping the scintillators with both reflective material and black Tedlar film has no effect on the quality of the time resolution and light output. While the time resolution only improved by about 10% when comparing wrapped and unwrapped scintillator paddle, the reflective materials did indeed improve the amount of light that was collected by the SiPM. These measurements

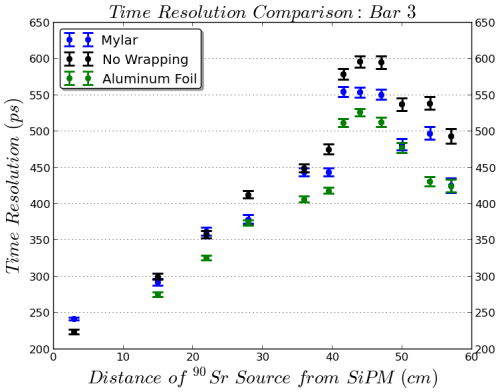

Figure 3.62: Reflective material.

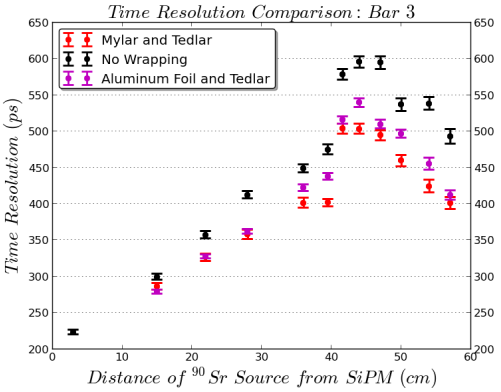

Figure 3.63: Reflective material & Tedlar.

prove the advantage of utilizing reflective materials in order to increase light output. Cross talk measurements were also conducted in order to determine the effect of the reflective materials ability to reducing the amount of cross talk between two adjacent scintillator paddles. These measurements verified the advantage of wrapping scintillators in reflective material in that the cross talk was reduced by a factor five when compared to scintillators that were tested with no reflective material between them. However, no difference was noticed between wrapping the scintillators with Mylar and food grade aluminum foil. This, coupled with previous wrapping tests indicating no substantial difference in time resolution between utilizing the Mylar and aluminum foil wrapping materials, it was decided that the individual scintillator paddles would be wrapped in aluminum foil since it is much easier to handle when wrapping scintillators.

Deterioration

A common occurrence in scintillators is a phenomenon known as crazing. Crazing can occur in scintillators for a multitude of reasons. Some of the most common causes of crazing is that the scintillator comes into contact with chemicals other than isopropyl alcohol. Even the acids and oils from ones skin can diffuse into the medium of the scintillator and cause them to craze. Furthermore, machining of scintillators increases the possibility of crazing occurring. Due to the stresses and strains undergone during the machining process, it is possible for the scintillators to develop crazing over time, which may have not been visible during the initial visual inspection. In going through many prototypes of Start Counter paddles, it was found that some scintillators deteriorated in quality over time (see figure 3.64) and began to show visible signs of both surface and internal crazing. Many prototypes were made, and many of them deteriorated over time and were rendered useless. After extensive discussions with both Eljen Technology and McNeal Enterprises, the minimization of these deteriorating effects was accomplished. The most recent batch of five prototypes were monitored closely for a period of three and a half months in order to monitor for deterioration, which has proven to be a problem with previous prototypes. After close monitoring it was discovered that the scintillators were in fact not deteriorating (see figures 3.65 & 3.66) over time. The quality of the five scintillators received in the most recent batch of prototypes from McNeal Enterprises have proven to be of the necessary quality to fulfil the needs of the GlueX Start Counter.

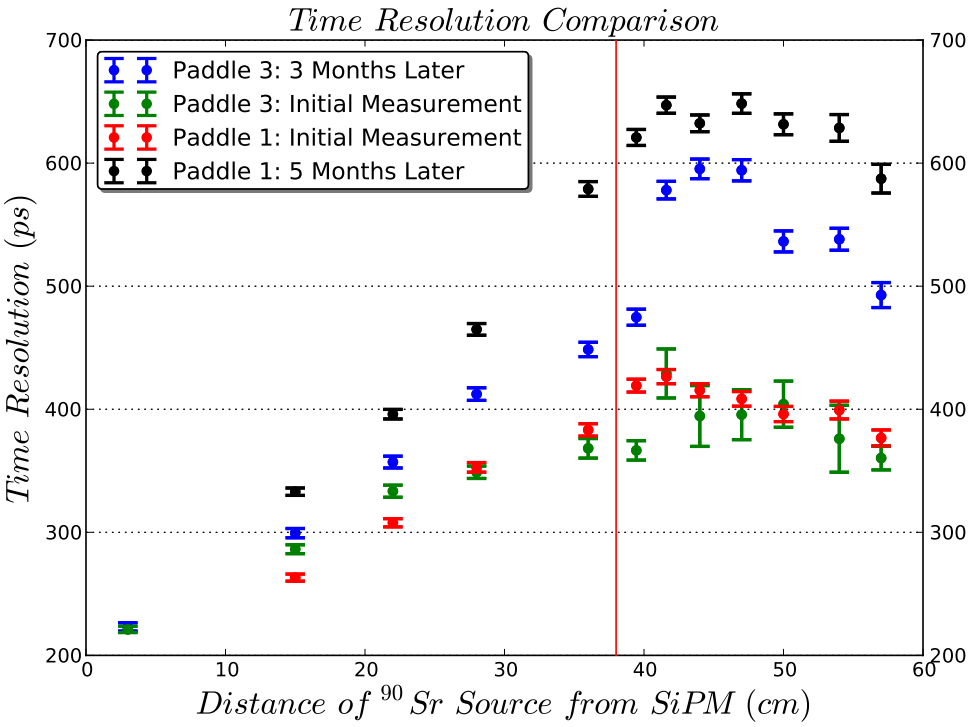

Figure 3.64: Deterioration Measurements. These data are an example of a batch of prototypes that deteriorated over time. It was discovered that after five months time, a ($\sim$ 175 ps), or 36% increase in time resolution had ensued resulting in an unacceptable quality of scintillator material.

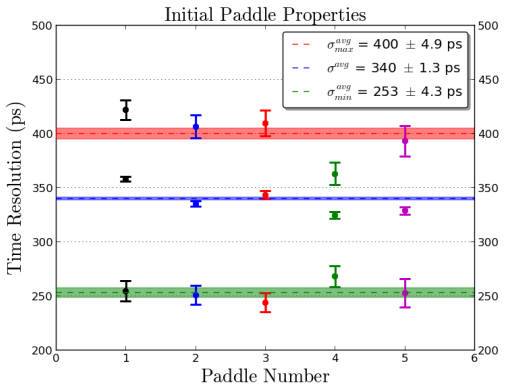

Figure 3.65: Initial Measurements.

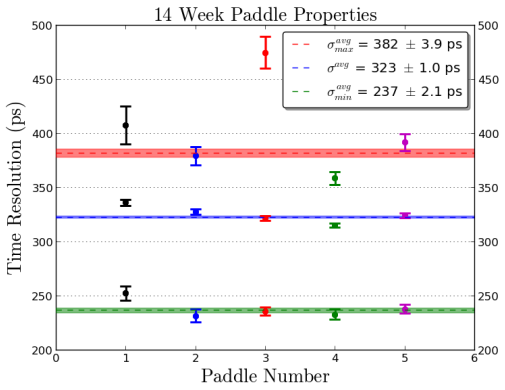

Figure 3.66: 14 Week Measurements.

Test Stand

A new test stand was designed and built in order to improve the reproducibility of the measurements conducted on machined scintillator paddles (see figure 3.67). The scintillator is held in place by two scintillator support pieces that are rigidly attached to the frame of the test

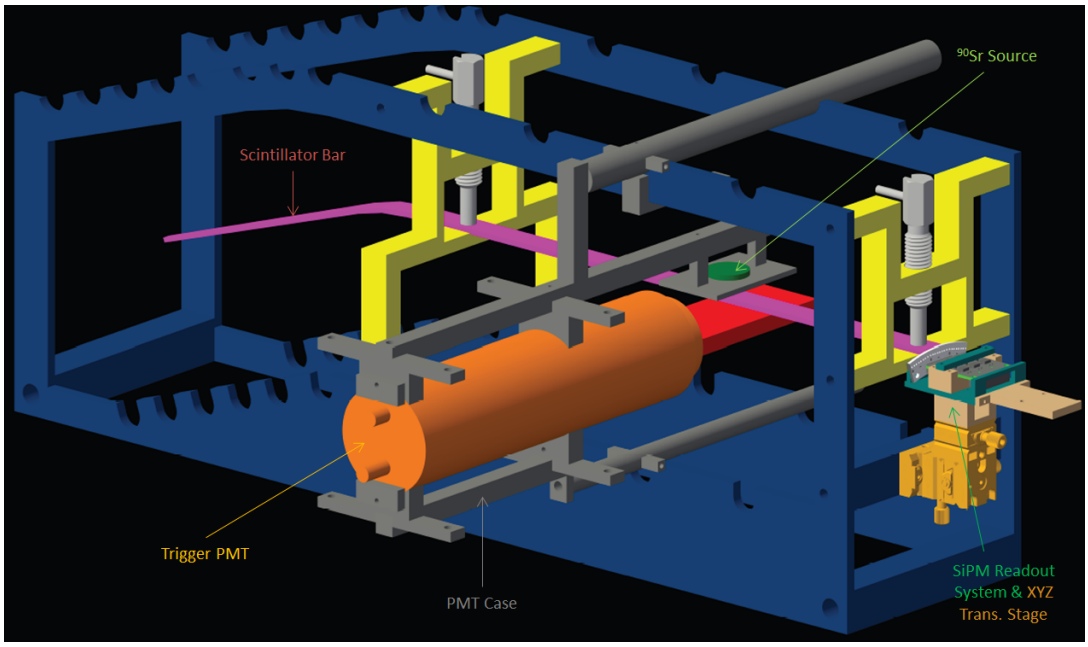

Figure 3.67: Start Counter test stand.

stand at fixed locations. The scintillator is held in place by spring loaded locking plungers that come into contact with a piece of protective foam which sits atop the surface of the scintillator. The frame has twelve grooves, machined at precise locations, cut out of the frame so that the trigger PMT may be held fixed at well defined locations along the path of the scintillators. The trigger PMT is held in place by a custom case designed to mount the ^{90}Sr source above the scintillator and the PMT below the scintillator. This design allows for the source and PMT to be moved as one unit, reducing the possibility of misalignment relative to one another, as well as their alignment relative to the scintillator. A SiPM and its readout system is placed at the upstream end of the scintillator while sitting atop a miniature dovetail XYZ translation stage. The translation stage allows for precise coupling of the SiPM relative to the upstream end of the scintillator. This design reduces any misalignment of the scintillator-SiPM interface which is crucial for maximizing the amount of light collected by the SiPM.

Assembly of the GlueX Start Counter

Description & Components

A preliminary design of an assembly jig is complete. The Rohacell support structure will be rigidly attached to a cylindrical chassis. A locking rotation device that is able to rotate in 12° intervals will be placed between two square bracket bearings that are centered on a square plate that is attached to the chassis. 10 ST1 and ST2 components will then be attached at fixed locations to the lip of the chassis. All of the devices will be supported by a stand. Two identical rings will each have 30 holes tapped through, separated by 12° of arc relative to the surface of the rings. Swivel screws with pads will then screw into the holes of the rings which will be placed around the Rohacell. The rings will be free-floating, only supported by swivel screws, and placed at two locations along the path of the straight section of the Rohacell support

structure. Two pneumatic cylinders, with steel rods that extend to a predetermined stroke length, are to be controlled by a pressurized air system and solenoid valves. The cylinders will be oriented perpendicular to the plane of the table that the stand will rest on. They will be supported by a bar that is to be welded to a large existing metal frame. The retractable steel rod of the pneumatic cylinders are extendible so that the tip will come into contact with surface of a scintillator that is being installed.

Installation

To install a scintillator paddle, the pneumatic cylinders will be retracted, as well as 2 of the 30 swivel screws that are oriented perpendicular to table. The scintillator will then slide down the surface of the Rohacell until it is placed as close as possible to the active area of the SiPM. The pneumatic cylinders will then be extended to hold the scintillator in place. Fine adjustments of the scintillator will be made so that the best possible alignment is achieved. The alignment of the scintillators with the SiPMs will be monitored closely with specialized camera optics. Once the scintillator is in a suitable position, the swivel screws will then be adjusted in order to come into contact with the scintillator, and the pneumatic cylinders will then be retracted. Upon completing the installation of one paddle, the whole device will be rotated by 12° and then another paddle will be installed in the exact same manner. This process will be repeated until all 30 paddles have been successfully installed. In order to keep all of the scintillators firmly in place in the absence of the rings and plungers, wrapping material (which has yet to be determined) will be installed. Once the assembly is successfully completed, the GlueX Start Counter will undergo extensive testing and calibration.

3.9 Readout Electronics

3.9.1 Electronics [59]

The main parameters and properties of the electronics are given in Table 3.28.

Table 3.28: Electronics channel counts.

Item	Description	Quantity
GlueX ASIC GASS-2	Drift chamber preamp 8ch/chip	2034
Preamp Card FDC wires	3 ASICs GASS-2, 24 ch, discriminated output	96 (110)
Preamp Card FDC strips	3 ASICs GASS-2, 24 ch, analog output	432 (475)
Preamp Card CDC wires	3 ASICs GASS-2, 24 ch, analog output	149 (165)
FANIO (for CAEN 1290)	Clock, synch, trigger signals fan in-out	1
DISC Discriminator	Leading-edge JLab discriminator, 16 ch	109
fADC125 V2	Sampling Flash 125 MHz, 12-bit, 72 ch	194
fADC250 V2	Sampling Flash 250 MHz, 12-bit, 16 ch	324
F1TDC V2	Pipeline TDC, 57 ps, ECL, 32 ch	50
F1TDC V3	Pipeline TDC, 97 ps, LVDS, 48 ch	48
CAEN VX 1290	Pipeline TDC, 25 ps, 32 ch	6
VME64x Crate	8 (DISC) and 3 (Controls)	11
VXS Crate	51 DAQ and 2 Trig	53
VME Crate controller	Readout Controller (ROC)	64
TI	Trigger Interface	52 (56)
SD	Signal Distribution	52 (56)
CTP	Crate Trigger Processor	26
SSP	Sub-system Processor	8
GTP	Global Trigger Processor	1
TS	Trigger Supervisor	1 (2)
TD	Trigger Distribution	9
LV MPV8008	MPOD 8V, 8 ch, 5A/ch	24
LV MPV8030	MPOD 30V, 8 ch, 2.5 A/ch	1
LV ISEG EHS 201P-F-K	MPOD 100V, 16 ch, 10 mA/ch	31
LV Chassis	MPOD Chassis / Mini (TAGM)	7/1
HV A1550P	CAEN +5kV, 1mA, 24 ch	10
HV A1550N	CAEN −5kV, 1mA, 24 ch	4
HV A1535SN	CAEN −3.5kV, 3mA, 24 ch	19
HV Chassis	CAEN HV chassis	6
Cabling	NEC 2011, NFPA 70, UL CL2 or better	
Racks	Hammond C4F247736 24”×36”×44”U w/d/h	47
	Low racks in the tagger hall	8
Grounding: Segregated clean and utility grounds separately bonded to hall floor grounding grid		
EMI	FCC Part 15, CISPR 22, Class B	

[59] *SVN revision ID:* tdr_summary_electr.tex 13854 2014-06-12 04:42:15Z gen

3.10 Trigger

3.10.1 Trigger Summary [60]

The main parameters and properties of the TRIGGER are given in Tables 3.29 and 3.30.

Table 3.29: TRIGGER properties.

Item	Value
L1 trigger rate (for high-lumi runs)	<200 kHz
L1 algorithm	energy balance in calorimeters (main algorithm), hits count
Detectors used in trigger:	
energy sum	BCAL, FCAL
hit count	TAGM, TAGH, SC, TOF, PSC
Trigger latency	$\sim 3.2\mu$s fixed latency
L3 trigger rate	20 kHz
Algorithm	Full event reconstruction on L3 farms
Number of farm nodes	TBD

Table 3.30: TRIGGER channel counts.

L1 modules	Description	Quantity
Crate Trigger Processor CTP	Sums energies from fADC250-MHz in the crate, form hit pattern	26
Sub-System Processor SSP	Sums energies from BCAL/FCAL crates, passes hit patterns to GTP	8
Global Trigger Processor GTP	Runs trigger algorithms	1
Trigger Supervisor TS	Handles trigger types, distribute triggers and clock	1
Trigger Distribution TD	Distributes triggers and clock to readout crates	9
Trigger Interface TI	Receives triggers and clock from SD	52 (56)
Signal Distribution SD	Distributes triggers and clock inside the crate	52 (56)

[60] *SVN revision ID:* tdr_summary_trig.tex 13854 2014-06-12 04:42:15Z gen

3.11 DAQ and Online

3.11.1 DAQ and Online Summary [61]

The main parameters and properties of Online Computing including the DAQ are given in Tables 3.31, 3.32 and 3.33. A listing of crates and electronic modules used by the DAQ system are given in Table 3.28.

Table 3.31: Online/DAQ components.

Item	Value
Hall network switch input ports	1 Gbit/s TCP/IP Ethernet (copper)
Hall network switch uplink ports	10 Gbit/s TCP/IP Ethernet (fiber)
Counting House main switch ports	1 Gbit/s and 10 Gbit/s Ethernet (copper,fiber)
DAQ interconnect protocol in Counting House	TCP/IP over 40 Gbit/s Infiniband
DAQ base architecture	CODA3, 2-stage event building
Pre/post level 3 event monitoring	20 kHz
Raid to silo network connection	Dual 10 Gbit/sec Ethernet (fiber)
Operating system on Counting House computers	RHEL6 (eventually RHEL7)

Table 3.32: Online/DAQ channel counts.

Item	Description	Quantity
Cisco 24-port endpoint switches	ROC and control uplinks	12
Cisco switch	Main Ethernet switch	1
Mellenox Infiniband switch	Central Infiniband switch	1
32-port Digi terminal servers	Provides remote RS232 access	8
Netapps file server	Central file server	1
16-core Dell servers	First stage event builders	6
32-core Dell servers	Second stage event builder	1
RAID servers (150 hours storage)	Local event data storage	2 @ 75 TB
Multi-core Dell servers	Online computing	21

Table 3.33: DAQ rates.

Item	Low Luminosity	High Luminosity
L1 Trigger rate	20 kHz	200 kHz
Average physics event size	15 kB	15 kB
Data rate (front-end)	300 MB/s	3000 MB/s
Data rate (tape)	300 MB/s	300 MB/s

[61] *SVN revision ID:* tdr_summary_online.tex 13854 2014-06-12 04:42:15Z gen

3.12 Slow Controls

3.12.1 Slow Controls Summary [62]

The main parameters and properties of the Slow Controls are given in Tables 3.34 and 3.35.

Table 3.34: Slow Control properties.

Item	Value
SCADA architecture foundation	EPICS
Display management framework	CSS BOY
Alarm handler	CSS BEAST
EPICS Archiving	JLab MYA
PLC Allen-Bradley communication protocol	EtherNet/IP
Communication protocol with Wiener chassis	SNMP
Communication protocol with CAEN chassis	Proprietary CAEN protocol over Ethernet
Communication protocol with FCAL bases	Custom protocol over Ethernet/CAN bridge
Communication protocol with microscope boards	Custom protocol over Ethernet

Table 3.35: Slow Controls channel counts.

Item	Description	Quantity
16-core Dell Linux servers	EPICS softIOCs	2
8-core Dell Linux servers	EPICS softIOCs	1
MOXA single board Linux computer	EPICS softIOC	1
VME Linux controllers	EPICS IOC	3
Allen-Bradley ControlLogix PLC CPU	Solenoid magnet controls	1
Allen-Bradley ControlLogix EN2T communication modules	Solenoid magnet controls	4
Allen-Bradley CompactLogix PLC CPUs	Detector controls	5
Allen-Bradley Point I/O PLC communication modules	Solenoid and detector controls	7
National Instruments PXI chassis	Solenoid magnet DAQ	1
RTA Serial-to-EtherNet/IP bridge modules	Magnet and detector controls	8
RTA Modbus-to-EtherNet/IP bridge modules	Magnet and detector controls	1
Anagate CAN-to-Ethernet bridge modules	Controls of FCAL PMT bases	7

[62] *SVN revision ID:* tdr_summary_controls.tex 13854 2014-06-12 04:42:15Z gen

Appendix A

Calibration

A.1 BCAL Calibration

The absolute calibration of the BCAL will be accomplished using the energy deposition of particles. We can use the showers from photons from π^0 and η decays and also charged particle ionization losses. No complete study has been conducted to date to demonstrate the detailed procedure that is needed to complete this task. But some preliminary studies have been made to estimate the coverage and anticipated statistics that could be expected.

Cosmic-rays will be used initially to equalize the response between cells and prototypes have already provided testbeds for such procedures [78]. Selection cuts were employed to define clean muon events and their energy deposition can be used for calibration as they provide 2 MeV per readout cell energy deposition in the fibers. When the magnet is on, charged particles can be used for calibration although their energy loss and trajectories must be simulated. Initial simulations have been carried out using charged pions and protons [79]. The detailed geometry of the matrix was simulated using FLUKA and GEANT 3.21 was used to simulated five modules next to each other, in order to ensure that energy escaping laterally from a module is recovered properly in an adjacent one. A realistic map of the GlueX solenoidal field was implemented. Pions and protons were simulated having momentum of 1 GeV/c and at 20°. The pions (protons) deposited ∼7 (8) MeV in inner cells, which implies that the calibration of the inner layers of the calorimeter is not very sensitive to the pion to proton ratio.

To estimate the statistics available for calibrations in the BCAL, we used the GlueX event generator BGGEN to produce the equivalent of 10 s of data at a photon beam flux of 10^7/s and selected events containing π^0 and ηs [80]. Photons were tagged as hitting the FCAL or BCAL, when their polar angle was between 1–11° or 11–126°, respectively. In order to have a robust sample of showers for the calibration, we required that both photons from each decay have at least 0.5 GeV of energy. In ten hours of data at $10^7\gamma$/s, we expect approximately 17 million π^0 events and approximately 3 million η events with both photons hitting the BCAL (see Fig. A.1). Comparable number of events produce one photon in the BCAL and one photon in the FCAL. Although the data set with π^0s is larger, its angular distribution is such that the maximum angles sampled barely extend much past 40°. The range can be extended to 60-70° by lowering the photon energy selection to about 0.2 GeV. The angular coverage for ηs is wider and will be needed to provide showers at the upstream end of the bcal.

For the BCAL calibration, we will likely begin with the sample of π^0 events with one photon in each of the calorimeters and fix the FCAL response to that already determined. The

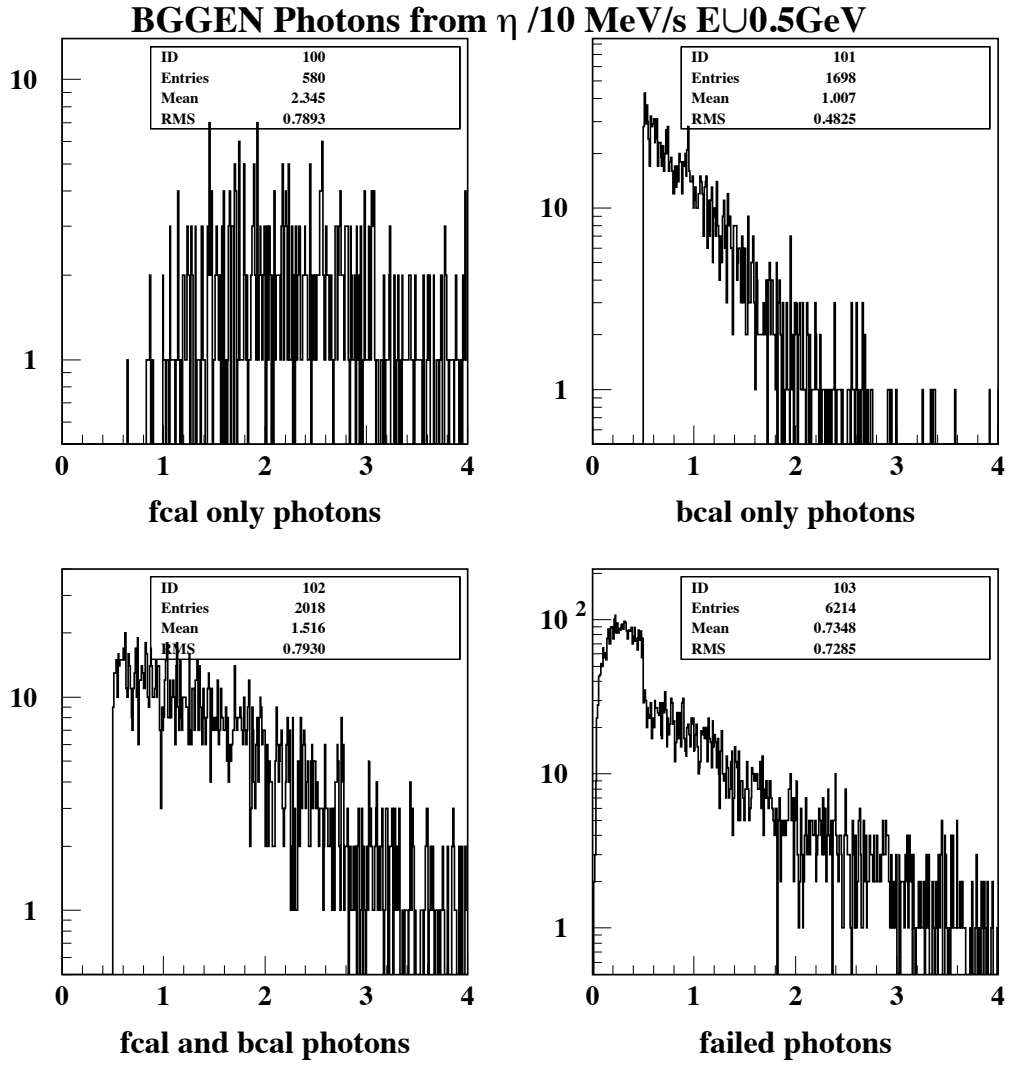

Figure A.1: The energy distribution of photons greater than 0.5 GeV from η decays. Top left) Energy distribution when both photons hit the FCAL. Top right) Energy distribution when both photons hit the BCAL. Bottom left) Energy distribution when one photon is detected in the FCAL and one photon is detected in the BCAL. Bottom right) Energy distribution of photons from η decays when at least one photon misses both calorimeters or the energy of one photon is below 0.5 GeV.

calibration constants for each cell in the BCAL will then be adjusted to minimize the width of the π^0 mass. There are 1536 adjustable channels in the BCAL; although for low-angle photons, only the inner layers contribute to the energy sums. The calibration constants can be confirmed or improved using the sample of π^0 events that decay into two photons that hit the BCAL. Once a reasonable starting point is obtained, this later sample may be the only one needed for smaller updates. Finally, the sample of ηs must be used to confirm the calibration over the full length of the BCAL, especially for any systematic effects near the upstream end.

Appendix B

Performance

B.1 Tracking

The tracking chambers are designed to reconstruct the momenta of the charged particles emerging from the target. The transverse momentum, $p_\perp$ and the dip–angle, λ, ($\lambda = \frac{\pi}{2} - \theta$) are measured from the curvature of the tracks in the solenoidal field and their initial direction. The total momentum and the longitudinal momentum are then obtained from these as $p_{total} = p_\perp \sec\lambda$ and $p_\parallel = p_\perp \tan\lambda$. The accuracy of the $p_\perp$ measuremen depends on the $r-\phi$ resolution of the tracking chambers, while the λ measurement relies on an accurate measurement of both z and the distance traveled. The tracking system in the GlueX detector must cover as close to a 4π solid angle as possible over a wide range of particle momenta and must have sufficient momentum resolution to be able to identify missing particles. To achieve these goals, the LASS detector [81] design was used as our starting point. This device used several different tracking elements each optimized for a particular region in the detector. All tracking devices are located inside the barrel calorimeter, which is in turn inside the 2.08 T solenoid. Surrounding the target is a cylindrical straw-tube drift chamber (CDC) which provides very good $r-\phi$ and good z resolution. In addition, this detector provides some dE/dx information to aid in the separation of π's, K's and p's up to momenta of about 0.45 GeV/c – a regime where dE/dx measurements work extremely well. In the forward region, round planar drift chambers (FDC) are arranged in four identical tracking packages. These packages allow tracking particles down to about one degree with respect to the beam line. A summary of the tracking chamber parameters are given in Table B.1.

System	*Radius*		*Length*		*Resolution*	
	$r_{\min}$ (cm)	$r_{\max}$ (cm)	z_{min} (cm)	$z_{\max}$ (cm)	$\sigma_{r-\phi}$ (μm)	σ_z (mm)
CDC	9.9	55.5	17	167	150	1.5
FDC	3.0†, 3.9‡	48.5	176	364	150	fixed

Table B.1: A summary of the tracking chamber parameters. The z values under *Length* indicate the smallest and largest z of the combined system. The z origin is at the upstream end of the magnet. The z resolution for the CDC comes from $\pm 6^\circ$ stereo layers. The z resolution of the planar chambers is assumed to be given by their position in space. †FDC packages 1 and 2, ‡FDC packages 3 and 4.

Pattern recognition is an important part of track reconstruction. This process requires finding local clusters of hits and associating them into small track segments that can be combined into larger tracks. In order for this procedure to work well, it is desirable to have sufficient hits in close proximity such that they will be easily associated. In the forward direction cathodes and anodes in each layer of the FDC are arranged such that together they provided a 3-dimensional point. Each package consists of six closely spaced planes. Such packages allow local identification of track segments with a reasonable measure of curvature. This has then been repeated four times to provide sufficient segments for high efficiency track-segment linking. In the CDC, the pattern recognition issue is dealt with by creating three sections containing several adjacent straight tubes. These are then interleaved with two sets of crossed stereo layers.

Bibliography

[1] G. Biallas and E. Chudakov, "Hall D Superconducting Solenoid," Tech. Rep. GlueX-doc-**2378**, Jefferson Lab, June, 2014. http://argus.phys.uregina.ca/cgi-bin/private/DocDB/ShowDocument?docid=2378. 21, 22, 23, 31

[2] "POISSON / SUPERFISH Program." http://laacg1.lanl.gov/laacg/services/download_sf.phtml. LANL. 21

[3] J. Ballard, G. H. Biallas, P. Brindza, T. Carstens, J. Creel, *et al.*, "Refurbishment and testing of the 1970's era LASS solenoid coils for Jlab's Hall D," *AIP Conf.Proc.* **1434** (2011) 861–868. http://scitation.aip.org/content/aip/proceeding/aipcp/10.1063/1.4707001. 21

[4] G. Biallas *et al.*, "Assembly of Solenoid Conductor Documents," Technical Note GlueX-doc-2510, JLab, 2014. http://argus.phys.uregina.ca/cgi-bin/private/DocDB/ShowDocument?docid=2510. 22

[5] J. S. Alcorn, H. Peterson, and S. S. Lorant, "Slac two-meter diameter, 25-kilogauss, superconducting solenoid, UAMH BINN," in *Applied Superconductivity Conference*, p. 273. Inst. of Electrical and Electronics Engineers, Inc., New York; Stanford Univ., CA, 1972. 22

[6] N. Laverdure, J. Creel, K. Dixon, V. Ganni, F. Martin, R. Norton, and S. Radovic, "The hall d solenoid helium refrigeration system at jlab," *AIP Conference Proceedings* **1573** no. 1, (2014) 329–336. http://scitation.aip.org/content/aip/proceeding/aipcp/10.1063/1.4860719. 31

[7] G. McNicoll, "A study of photon sensitivity in the Hall D detector," Tech. Rep. GlueX-doc-**36**, Carnegie Mellon University, 2000. http://argus.phys.uregina.ca/cgi-bin/private/DocDB/ShowDocument?docid=36. 39

[8] J. Kuhn and C. A. Meyer, "Acceptance Study for the GlueX detector system," Tech. Rep. GlueX-doc-**264**, 2004. http://argus.phys.uregina.ca/cgi-bin/private/DocDB/ShowDocument?docid=264. 39

[9] C. A. Meyer, "A study of timing resolutions on particle identification in the Hall Ddectector at jefferson lab," Tech. Rep. GlueX-doc-**14**, Carnegie Mellon University, 1999. http://argus.phys.uregina.ca/cgi-bin/private/DocDB/ShowDocument?docid=14. 39

[10] C. A. Meyer and P. Eugenio, "A Study of Compined K–π Separation using Time–of–Flight Counters and a Gas Čerenkov Detector," Tech. Rep. GlueX-doc-**15**, Carnegie Mellon University, 1998. http://argus.phys.uregina.ca/cgi-bin/private/DocDB/ShowDocument?docid=15. 39

[11] T. Sjostrand, L. Lonnblad, and S. Mrenna, "PYTHIA 6.2: Physics and manual," arXiv:hep-ph/0108264. 39

[12] R. Brun *et al.*, 1986. GEANT3, CERN-DD/EE/84-1. 39

[13] M. Adinolfi, F. Ambrosino, A. Antonelli, M. Antonelli, F. Anulli, *et al.*, "The KLOE electromagnetic calorimeter," *Nucl.Instrum.Meth.* **A461** (2001) 344. 41

[14] M. Adinolfi, F. Ambrosino, A. Antonelli, M. Antonelli, F. Anulli, *et al.*, "The KLOE electromagnetic calorimeter," *Nucl.Instrum.Meth.* **A482** (2002) 364–386. 41

[15] M. Adinolfi, F. Ambrosino, A. Antonelli, M. Antonelli, F. Anulli, *et al.*, "The KLOE electromagnetic calorimeter," *Nucl.Instrum.Meth.* **A494** (2002) 326–331. 41

[16] A. Antonelli, M. Antonelli, G. Barbiellini, M. Barone, S. Bertolucci, *et al.*, "Measurements of light yield, attenuation length and time response of long samples of 'blue' scintillating fibers," *Nucl.Instrum.Meth.* **A370** (1996) 367–371. 41

[17] R. Wigmans, *Calorimetry: Energy measurement in particle physics*, vol. 107 of *International Series of Monographs on Physics*. Oxford University Press, 2000. 41, 54

[18] E. Chudakov *et al.*, "Summary of Hall D Subsystems," Specification D00000-00-00-S006, Jefferson Lab, May, 2013. https://misportal.jlab.org/jlabDocs/document.seam?id=79548. 42

[19] J. Lagner, "Hall D GlueX Detector Barrel Calorimeter Sub-Assembly," Drawing D00000-01-07-1000, Jefferson Lab, Apr., 2009. https://misportal.jlab.org/jlabDocs/document.seam?id=65967. 42

[20] Brian Klein *et. al*, "B-CAL Progress and Construction Report," Tech. Rep. GlueX Technical Note **333**, 2004. http://argus.phys.uregina.ca/cgi-bin/private/DocDB/ShowDocument?docid=333. 44

[21] B. Klein and Z. Papandreou, "GlueX BCAL Construction Video Guide," Tech. Rep. GlueX-doc-**1144**, University of Regina, Oct., 2008. http://argus.phys.uregina.ca/cgi-bin/private/DocDB/ShowDocument?docid=1144. 44

[22] B. Klein, "BCAL Electroneumatic Press Photos," Tech. Rep. GlueX-doc-**1187**, University of Regina, Jan., 2009. http://argus.phys.uregina.ca/cgi-bin/private/DocDB/ShowDocument?docid=1187. 44

[23] B. Klein, "BCAL Electroneumatic Press Operation Videos," Tech. Rep. GlueX-doc-**1188**, University of Regina, Jan., 2009. http://argus.phys.uregina.ca/cgi-bin/private/DocDB/ShowDocument?docid=1188. 44

[24] Z. Papandreou and D. Kolybaba, "Barrel calorimeter module construction procedure manual and procedures," Tech. Rep. GlueX-doc-**1573**, University of Regina, Aug., 2010. http://argus.phys.uregina.ca/cgi-bin/private/DocDB/ShowDocument?docid=1573. 44

[25] E. Smith, "Acceptance Studies for the Production Light Guides of the BCAL," Tech. Rep. GlueX-doc-**1784**, Jefferson Lab, June, 2011. http://argus.phys.uregina.ca/cgi-bin/private/DocDB/ShowDocument?docid=1784. 44

[26] C. Hutton, "Hall D GlueX Barrel Detector Light Guide A," Drawing D00000-01-07-2057, Jefferson Lab, Mar., 2012. https://misportal.jlab.org/jlabDocs/document.seam?id=69828. 44

[27] C. Hutton, "Hall D GlueX Barrel Detector Light Guide B," Drawing D00000-01-07-2058, Jefferson Lab, Mar., 2012. https://misportal.jlab.org/jlabDocs/document.seam?id=69829. 44

[28] C. Hutton, "Hall D GlueX Barrel Detector Light Guide C," Drawing D00000-01-07-2059, Jefferson Lab, Mar., 2012. https://misportal.jlab.org/jlabDocs/document.seam?id=69830. 44

[29] C. Hutton, "Hall D GlueX Barrel Detector Light Guide D," Drawing D00000-01-07-2060, Jefferson Lab, Mar., 2012. https://misportal.jlab.org/jlabDocs/document.seam?id=69831. 44

[30] C. Hutton, "Hall D GlueX Barrel Detector Light Guide E," Drawing D00000-01-07-2061, Jefferson Lab, Mar., 2012. https://misportal.jlab.org/jlabDocs/document.seam?id=69832. 44

[31] C. Hutton, "Hall D GlueX Barrel Detector Light Guide F," Drawing D00000-01-07-2062, Jefferson Lab, Mar., 2012. https://misportal.jlab.org/jlabDocs/document.seam?id=69833. 44

[32] C. Hutton, "Hall D GlueX Barrel Detector Light Guide G," Drawing D00000-01-07-2063, Jefferson Lab, Mar., 2012. https://misportal.jlab.org/jlabDocs/document.seam?id=69834. 44

[33] C. Hutton, "Hall D GlueX Barrel Detector Light Guide H," Drawing D00000-01-07-2064, Jefferson Lab, Mar., 2012. https://misportal.jlab.org/jlabDocs/document.seam?id=69835. 44

[34] C. Hutton, "Hall D GlueX Barrel Detector Light Guide J," Drawing D00000-01-07-2065, Jefferson Lab, Mar., 2012. https://misportal.jlab.org/jlabDocs/document.seam?id=69836. 44

[35] C. Hutton, "Hall D GlueX Barrel Detector Light Guide K," Drawing D00000-01-07-2066, Jefferson Lab, Mar., 2012. https://misportal.jlab.org/jlabDocs/document.seam?id=69837. 44

[36] J. Fochtman, "BCAL Light Guide Installation and Rework," Procedure D00000-01-07-P003, Jefferson Lab, June, 2013. https://misportal.jlab.org/jlabDocs/document.seam?id=75344. 44

[37] E. Smith, "Test of wrapping on BCAL light guides," Tech. Rep. GlueX-doc-**1948**, Jefferson Lab, Mar., 2012. http://argus.phys.uregina.ca/cgi-bin/private/DocDB/ShowDocument?docid=1948. 44

[38] E. Smith, "Procedure for Gluing Light Guides onto Bcal modules," Traveler GEV12-HALLD-BCAL-GUIDES, Jefferson Lab, Feb., 2013. https://pansophy.jlab.org/pansophy/Travelers/TRAVELER_INDEX.cfm?project=GEV12&area=GEV12&system=HALLD. 44

[39] Y. Qiang, C. Zorn, F. Barbosa, and E. Smith, "Radiation Hardness Tests of SiPMs for the JLab Hall D Barrel Calorimeter," *Nucl.Instrum.Meth.* **A698** (2013) 234–241, arXiv:1207.3743 [physics.ins-det]. 45, 46

[40] Hamamatsu, "MPPC Multi-Pixel Photon Counter," data sheet, Jan, 2008. 46

[41] E. Smith, "Hall D BCAL Readout: Silicon Photomultiplier Array Specification," Specification D00000-01-07-S004 Rev-B, Jefferson Lab, June, 2012. https://misportal.jlab.org/jlabDocs/document.seam?id=70738. 46

[42] **GlueX Collaboration** Collaboration, F. Barbosa *et al.*, "Silicon photomultiplier characterization for the GlueX barrel calorimeter," *Nucl.Instrum.Meth.* **A695** (2012) 100–104. 46

[43] F. Barbosa *et al.*, "Test Results for the 80 First Article Samples of the Hamamatsu Array," Tech. Rep. GlueX-doc-**1777**, Jefferson Lab, June, 2011. http://argus.phys.uregina.ca/cgi-bin/private/DocDB/ShowDocument?docid=1777. 46

[44] Y. Qiang, C. Zorn, F. Barbosa, and E. Smith, "Neutron radiation hardness tests of SiPMs," *AIP Conf.Proc.* **1560** (2013) 703–705. 46

[45] C. Z. E.S. Smith, Y. Qiang, "Status of understanding of Radiation Damage to SiPMs," Tech. Rep. GlueX-doc-**2059**, Jefferson Lab, July, 2010. http://argus.phys.uregina.ca/cgi-bin/private/DocDB/ShowDocument?docid=2059. 46

[46] P. Lightfoot, G. Barker, K. Mavrokoridis, Y. A. Ramachers, and N. Spooner, "Characterisation of a silicon photomultiplier device for applications in liquid argon based neutrino physics and dark matter searches," *JINST* **3** (2008) P10001, arXiv:0807.3220 [physics.ins-det]. 46

[47] Z. Papandreou *et al.*, "Cosmic Ray Tests and Light Output from BCAL," Tech. Rep. GlueX-doc-**1864**, University of Regina and Jefferson Lab, Nov., 2011. http://argus.phys.uregina.ca/cgi-bin/private/DocDB/ShowDocument?docid=1864. 48

[48] J. McKisson, "BCAL Temperature Compensation Calculations," Tech. Rep. GlueX-doc-**2394**, Jefferson Lab, Feb., 2014. http://argus.phys.uregina.ca/cgi-bin/private/DocDB/ShowDocument?docid=2394. 48

[49] E. Anassontzis, P. Ioannou, C. Kourkoumelis, G. Vasileiadis, G. Voulgaris, *et al.*, "Relative gain monitoring of the GlueX calorimeters," *Nucl.Instrum.Meth.* **A738** (2014) 41–49. 48

[50] E. Smith, "Scintillation Fibers for the Barrel Calorimeter," Specification D00000-01-07-S001 Rev-A, Jefferson Lab, May, 2008. https://misportal.jlab.org/jlabDocs/document.seam?id=70607. 50

[51] B. Giebrecht *et. al*, "Performance of 'first-article' scintillating fibres for the GlueX Barrel Calorimeter," Tech. Rep. GlueX-doc-**1317**, University of Regina, Dec., 2009. http://argus.phys.uregina.ca/cgi-bin/private/DocDB/ShowDocument?docid=1317. 50

[52] Z. Papandreou, "BCAL Scintillating Fibre Performance: Half Way Milestone," Tech. Rep. GlueX-doc-**1647**, University of Regina, Dec., 2010. http://argus.phys.uregina.ca/cgi-bin/private/DocDB/ShowDocument?docid=1647. 50

[53] Z. Papandreou, "Fibre QA for Shipments 28 and 29," Tech. Rep. GlueX-doc-**1809**, University of Regina, Sept., 2011. http://argus.phys.uregina.ca/cgi-bin/private/DocDB/ShowDocument?docid=1809. 50

[54] Z. Papandreou, "Performance of Kuraray SCSF-78MJ scintillating fibres for the GlueX Barrel Calorimeter," Tech. Rep. GlueX-doc-**1956**, University of Regina, Apr., 2012. http://argus.phys.uregina.ca/cgi-bin/private/DocDB/ShowDocument?docid=1956. 50, 51, 53

[55] A. Baulin *et al.*, "Attenuation length and spectral response of Kuraray SCSF-78MJ scintillating fibres," *Nucl.Instrum.Meth.* **A715** no. 0, (2013) 48 – 55. http://www.sciencedirect.com/science/article/pii/S016890021300315X. 50, 53

[56] Z. Papandreou, B.D. Leverington and Lolos, G.J., "Spectral response of scintillating fibres," Tech. Rep. GlueX-doc-**1072**, University of Regina, June, 2008. http://argus.phys.uregina.ca/cgi-bin/private/DocDB/ShowDocument?docid=1072. 50

[57] Kuraray, "Fiber Spectra from Lot 72," tech. rep., October, 2009. Private communication. 51

[58] B. Leverington *et al.*, "Performance of the prototype module of the gluex electromagnetic barrel calorimeter," *Nucl.Instrum.Meth.* **A596** no. 3, (2008) 327 – 337. http://www.sciencedirect.com/science/article/pii/S0168900208013077. 53

[59] B.D. Leverington *et al.*, "Performance of the prototype module of the GlueX electromagnetic barrel calorimeter," Tech. Rep. GlueX-doc-**1071**, University of Regina, June, 2008. http://argus.phys.uregina.ca/cgi-bin/private/DocDB/ShowDocument?docid=1071. 53

[60] S. Katsaganis and Z. Papandreou, "Standalone Simulations for the Barrel Calorimeter: Double-Clad Fibres," Tech. Rep. GlueX-doc-**1871**, University of Regina, Dec., 2011. http://argus.phys.uregina.ca/cgi-bin/private/DocDB/ShowDocument?docid=1871. 54, 56, 57

[61] G. Koleva, "BCAL Prototype Beam Test at the M11 Channel at TRIUMF," Master's thesis, University of Regina, 2006. 54

[62] R. Jones, 2001. The HDGeant Monte Carlo Program. 56

[63] **Particle Data Group** Collaboration, J. Beringer *et al.*, "Review of Particle Physics (RPP)," *Phys.Rev.* **D86** (2012) 010001. 56

[64] Z. Papandreou, "BCAL Calorimetry Response," Tech. Rep. GlueX-doc-**840**, University of Regina, Jan., 2008. http://argus.phys.uregina.ca/cgi-bin/private/DocDB/ShowDocument?docid=840. 56, 57

[65] A. Dzierba, Z. Papandreou *et al.*, "BCAL Facts: What we know and how we know," Tech. Rep. GlueX-doc-**842**, University of Indiana and University of Regina, July, 2007. http://argus.phys.uregina.ca/cgi-bin/private/DocDB/ShowDocument?docid=842. 56

[66] B. Leverington, "BCAL Sampling Fraction ...," Tech. Rep. GlueX-doc-**827**, University of Regina, Jan., 2007. http://argus.phys.uregina.ca/cgi-bin/private/DocDB/ShowDocument?docid=827. 57

[67] M. Antonelli, G. Barbiellini, S. Bertolucci, C. Bini, C. Bloise *et al.*, "The electromagnetic calorimeter of the KLOE experiment at DANE," *Nucl.Instrum.Meth.* **A379** (1996) 511–514. 57

[68] I. S. A. Semenov, "Photon-Neutron Separation with BCAL," Tech. Rep. GlueX-doc-**1865**, Jefferson Lab, Nov., 2011. http://argus.phys.uregina.ca/cgi-bin/private/DocDB/ShowDocument?docid=1865. 58

[69] G. Lolos *et al.*, "Proposal for Beam Test of a GlueX Barrel Calorimeter Prototype in Hall B," Tech. Rep. GlueX-doc-**1900**, Jefferson Lab, Mar., 2012. http://argus.phys.uregina.ca/cgi-bin/private/DocDB/ShowDocument?docid=1900. 58

[70] J. Bennett, M. Kornicer, M. Shepherd, and M. Ito, "Precision timing measurement of phototube pulses using a flash analog-to-digital converter," *Nucl.Instrum.Meth.* **A622** (2010) 225–230, arXiv:1005.5349 [physics.ins-det]. 61

[71] K. Moriya, J. Leckey, M. Shepherd, K. Bauer, D. Bennett, *et al.*, "A measurement of the energy and timing resolution of the GlueX Forward Calorimeter using an electron beam," *Nucl.Instrum.Meth.* **A726** (2013) 60–66. 61

[72] B. Brabson, R. Crittenden, A. Dzierba, T. Foxford, J. Gunter, *et al.*, "A Study of two prototype lead glass electromagnetic calorimeters," *Nucl.Instrum.Meth.* **A332** (1993) 419–443. 64

[73] A. Brunner, R. Crittenden, A. Dzierba, J. Gunter, R. Gardner, *et al.*, "A Cockcroft-Walton base for the FEU84-3 photomultiplier tube," *Nucl.Instrum.Meth.* **A414** (1998) 466–476. 65

[74] Y. Van Haarlem, C. Meyer, F. Barbosa, B. Dey, D. Lawrence, V. Razmyslovich, E. Smith, G. Visser, *et al.*, "The GlueX Central Drift Chamber: Design and Performance," *Nucl.Instrum.Meth.* **A622** (2010) 142–156, arXiv:1004.3796 [nucl-ex]. 71, 83

[75] S. Roth and R. Schumacher, "A computer-controlled tension monitoring system for drift chamber wires," *Nucl.Instrum.Meth.* **A369** (1996) 215–221. 79

[76] R. Veenhof, *The GARFIELD Program, Simulation of Gaseous Detectors*. CERN, 1984. http://garfield.web.cern.ch/garfield/. 85

[77] H. C. Fenker, J. Thomas, M. Brooks, D. Lee, and G. Mills, "Precision interpolating pad chambers," *Nucl.Instrum.Meth.* **A367** (1995) 285–289. 94

[78] A. Semenov and I. Semenova, "Cosmic Ray Tests and Light Output from BCAL," Tech. Rep. GlueX-doc-**1582**, University of Regina, Sept., 2010. http://argus.phys.uregina.ca/cgi-bin/private/DocDB/ShowDocument?docid=1582. 119

[79] I. S. A. Semenov, "Hadronic Calibration of BCAL," Tech. Rep. GlueX-doc-**1344**, Jefferson Lab, Sept., 2009. http://argus.phys.uregina.ca/cgi-bin/private/DocDB/ShowDocument?docid=1344. 119

[80] E. Smith, "Statistics for p0 and eta production," Tech. Rep. GlueX-doc-**1702**, Jefferson Lab, Feb., 2011. http://argus.phys.uregina.ca/cgi-bin/private/DocDB/ShowDocument?docid=1702. 119

[81] D. Aston, N. Awaji, L. Bird, D. Blockus, R. K. Carnegie, J. D'Amore, W. M. Dunwoodie, S. Durkin, R. Endorf, P. G. Estabrooks, T. H. Fieguth, K. Fujii, M. G. D. Gilchriese, M. F. Gravina, H. Hanerfeld, H. Hayashii, R. J. Hemingway, A. K. Honma, D. Hutchinson, S. Iwata, W. B. Johnson, R. Kajikawa, A. Kilert, P. F. Kunz, D. W. G. S. Leith, L. J. Levinson, L. Madansky, M. Marshall, T. Matsui, R. McKee, R. McKillan, D. G. McShurley, B. T. Meadows, W. T. Meyer, A. Miyamoto, M. Nussbaum, A. Nuttall, G. K. Oakham, G. Oxoby, H. Ozaki, C. O. Pak, A. Pevsner, B. N. Ratcliff, R. H. Richter, J. A. Scheid, D. Schultz, S. Shapiro, T. Shimomura, P. K. Sinervo, A. Sugiyama, S. Suzuki, G. J. Tarnopolsky, T. Tauchi, K. Ukai, J. Vavra, A. Waite, W. Walsh, S. H. Williams, and C. Woody, "The LASS spectrometer," Tech. Rep. SLAC-298, SLAC, Stanford, CA, 1986. Copies available from the SLAC publications office, at http://www.slac.stanford.edu/pubs/. 122